2009

FILM CONVERSION AND BREAKDOWN PROCESSES ON CARBON STEEL IN THE PRESENCE OF HALIDES

Katayoun Yazdanfar

FILM CONVERSION AND BREAKDOWN PROCESSES ON CARBON STEEL IN THE PRESENCE OF HALIDES

(Spine title: Film Conversion and Breakdown Processes on Carbon Steel)

(Thesis format: Monograph}

by

Katayoun Yazdanfar

Graduate Program in Chemistry

A thesis submitted in partial fulfillment
of the requirements for the degree of
Master of Science

School of Graduate and Postdoctoral Studies
The University of Western Ontario
London, Ontario, Canada
November 2009

Abstract

The objective of this research is to determine the features which cause film breakdown leading to pitting on carbon steel in solutions containing halide anions (Cl^-, Br^-, I^-). It is commonly accepted that the influence of Cl^- on passive film properties is the key feature in breakdown, and the possibility that transformations in the oxide are responsible has not been considered. Since electrochemical techniques are extremely sensitive and easy to apply , they have been used to follow the kinetics of reactions occurring on a carbon steel surface at pH = 10.6. This particular pH was chosen since these studies are part of a larger project to determine the behaviour of carbon steel under CANDU reactor operating conditions.

The electrochemical techniques, Electrochemical Impedance Spectroscopy (EIS), Cyclic Voltammetry and Amperometry, and surface analytical methods such as Scanning Electron Microscopy (SEM), Energy Dispersive X-ray (EDX), X-ray Photoelectron Spectroscopy (XPS), and in-situ/ex-situ Raman spectroscopy have been used to investigate the changes in film properties leading to breakdown in borate-buffered solutions containing either Cl^-, Br^- or I^-. While variations in breakdown potential are observed in the presence of the different halide anions, its value does not vary consistently with either halide type or concentration, and breakdown never occurs below a critical potential of 0.0 V vs SCE. These results suggest that the key features leading to breakdown are subtle changes in oxide structure/composition at higher potentials. Current measurements under potentiostatic conditions indicate that the Fe_3O_4/γ-Fe_2O_3

passive film grown at lower potentials thickens slightly when the potential is increased above a critical value. This indicates an increase in defectiveness of the film occurs in this potential range. A possible interpretation is that the field-assisted conversion of the $Fe^{II/III}$ oxide (Fe_3O_4 /γ-Fe_2O_3) to γ-FeOOH, which is thermodynamically possible in this potential range, leads to a considerable volume change which creates stress in the oxide film leading to localized fracture. In borate solutions containing no halide, the film is rapidly repaired by further Fe_3O_4/γ-Fe_2O_3/γ-FeOOH growth, leading to the observed thickening. That thickening and an increase in Fe^{III} content occurs is confirmed by XPS measurements. However, in the presence of halide ions, halide transport to the metal/oxide interface prevents repassivation leading to initiation of pitting.

Keywords: Film Breakdown, Breakdown Potential, Carbon Steel, Pit Initiation, Halide Solutions, Mildly Basic

Acknowledgements

First and foremost, I would like to thank my supervisors, Dr. David W. Shoesmith and Dr. Jungsook C. Wren, without whose support and help the completion of this thesis would not have been possible. Their dedications to my research and the guidance and patience which they so graciously extended to me throughout my graduate studies have been great blessings. I am, therefore, deeply indebted to them for their willingness to take me on and keep me as a member of their research groups.

I would also like to express my sincere gratitude to Dr. X. Zhang, Dr. J. Noël and Dr. P. Keech for the countless hours they spent guiding me through my research. They were always willing to answer my questions and ready to share their knowledge with me.

I am taking this opportunity to acknowledge Surface Science Western for its wonderful services and for the use of its instruments.

I would also like to thank the past and present members of the Shoesmith and Wren groups for their help, support, and friendship throughout my graduate studies.

Finally, I give my sincerest and most heartfelt thanks to my parents and my family for all their love and support.

I would not have been able to get this far without all of you.

Table of Contents

List of Figures

List of Tables

List of Abbreviation, Symbols and Nomenclature

^{o}	Degree
%	Percent
wt	Weight
ν	Scattered light frequency
$\nu_{\circ}$	Excitation frequency
θ	Phase angle
ω	Angular velocity
Ω	Ohm
BCC	Body centred cubic
Br^{-}	Bromide ion
°C	Degree Celcius
C	Carbon / Coulombs / Capacitance
C_{OX}	Capacitance of the oxide film
$Ca(OH)_2$	Calcium hydroxide
CANDU	CAnada Deuterium Uranium
CE	Counter electrode
Cl^{-}	Choloride ion
CPE	Constant phase element
CS	Carbon steel
CV	Cyclic voltammetry

E	Potential
E_B	Binding energy
E_K	Kinetic energy
E^0	Amplitute of a sinusoidal potential
E_{App}	Applied potential
E_{corr}	Corrosion potential
E_{eq}	Equilibrium potential
EIS	Electrochemcial impedance spectroscopy
EDX	Energy dispersive x-ray
eV	Electron volt
F	Faraday constant / Farad / Flourine
FCC	Face centred cubic
Fe	Iron
Fe^{2+}	Aqueous iron in the plus two oxidation state
Fe^{3+}	Aqueous iron in the plus three oxidation state
Fe^{II}	Iron coordinated in an oxide in the plus two oxidation state
Fe^{III}	Iron coordinated in an oxide in the plus three oxidation state
Fe_3O_4	Magnetite
α- Fe_2O_3	Hematite
γ- Fe_2O_3	Maghemite
$Fe(OH)_2$	Iron dihydroxide
$Fe(OH)_3$	Iron trihydroxide
γ- FeOOH	Lepidocrocite

h	Planck constant
HTS	Heat transport system
hν	Photon energy
Hz	Hertz
I	Current
I^0	Amplitude of a sinusoidal current
j	imaginary unit
KCl	Potassium chloride
KOH	Potassium hydroxide
LiBr	Lithium bromide
LiCl	Lithium chloride
mol	Mole
MPa	Mega pascal
mV	Millivolt
Mn	Manganese
$Na_2B_4O_7$	Sodium borate
NaCl	Sodium choloride (salt)
NaOH	Sodium hydroxide
NHE	Normal hydrogen electrode
P	Phosphorous
pH	Cologarithm of the activity of dissolved hydrogen ions
PLWR	Pressurized light water reactor
PHWR	Pressurized heavy water reactor

PWR	Pressurized light water reactor
R	Resistance
R_{OX}	Resistance of the oxide film
RE	Reference electrode
R_S	Solution resistance
RRDE	Rotating ring disc electrode
S	Sulfur
Si	Silicon
SCE	Saturated calomel electrode
SEM	Scanning electron microscopy
SHE	Standard hydrogen electrode
t	Time
UO_2	Uranium dioxide
V	Volt
WE	Working electrode
XPS	x-ray photoelectron spectroscopy
Z	Impedance
Z_{imag}	Imaginary impedance
Z_{real}	Real impedance

Chapter 1

1 INTRODUCTION

1.1 Carbon Steel and its Application in Nuclear Systems

Carbon steel, also known as plain steel or mild steel, is a metallic iron-based alloy, with small amounts of impurities such as Si, Mn, P and S. Table 1-1 lists a typical carbon steel composition. Commonly, the presence of minor elements is ignored in terms of the expectations for the performance of carbon steels. In addition, as its name suggests, carbon is the important secondary component of carbon steel. Carbon molecules fit into interstitial sites within the body-centered cubic structure of iron. This makes the material harder and inhibits dislocation movement. In this way carbon molecules increase the strength of iron. Depending on its carbon content, steel can be classified into three major categories: low-carbon steel (> 0.25 wt% C), medium-carbon steel (between 0.25 and 0.6 wt% C), and high-carbon steel (between 0.6 and 1.4 wt% C)[1]. For better understanding of these three categories the phase diagram of iron-iron carbide needs to be reviewed. The Figure 1.1 shows a portion of the temperature and carbon ranges for certain types of heat treatments. When heated, pure iron experiences two changes in crystal structure before it melts. The stable form at room temperature, called ferrite, or α iron, has a BCC crystal structure with 0.02 wt% C composition. Ferrite undergoes a polymorphic transformation to FCC austenite, or γ iron, at 912°C with a composition of 0.8 wt% C. At 1394°C FCC austenite reverts back to a BCC phase

known as a γ ferrite, which finally melts at 1538°C [1-2]. The Figure 1.1 shows the composition of carbon up to 6.70 wt% C, which corresponds to the formation of iron carbide, or cementite (Fe_3C). When slowly cooled through eutectoid temperature, the microstructure of iron-carbon alloys consists of two phases: α and Fe_3C. Those form simultaneously during the transformation and are referred to as pearlite. Mechanically, pearlite has properties intermediate between the soft, ductile ferrite and hard, brittle cementite because carbon atoms diffuse away from the 0.02 wt% ferrite regions and to the 6.7 wt% cementite layers, as the perarlite extends [2].

Table 1-1 A Typical Carbon Steel composition expressed as wt%

Fe	C	Si	Mn	P	S
Balance	0.23	0.22	1.05	0.012	0.014

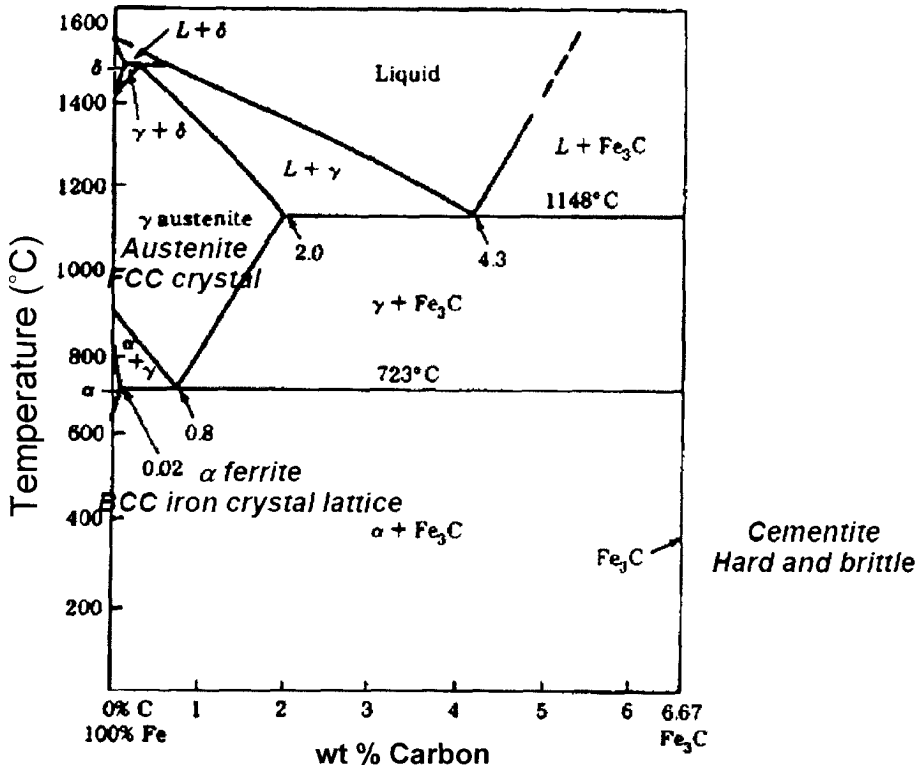

Figure 1-1 : The iron-iron carbide phase diagram [2].

1.1.1 Low-Carbon Steels

Of the different kinds of carbon steels, low-carbon steel is produced in the greatest quantities. Low-carbon steels contain less than about 0.25 wt% C, and are unresponsive to heat treatments designed to form martensite, the product of rapidly quenching austenite, which is seen in other steels. The crystal structure of martensite is Body-centered tetragonal and it has a needle-shaped grains [1]. Therefore, strengthening is done by means of cold work. Microstructures consist of ferrite (the stable iron-iron

carbide phase at room temperature) and pearlite (the product of the transformation of austenite through slow cooling) constituents. As a result, low carbon steels are comparatively soft and weak; however, they possess high ductility and toughness [1] Furthermore, they are machinable, weldable, and the least expensive to produce, since purity is a less rigorous requirement than in other carbon steels [2].

1.1.2 Medium-Carbon Steels

Carbon concentrations in the medium-carbon steels vary from 0.25 to 0.6 wt%. In order to improve the mechanical properties of the medium-carbon steels, they may be heat treated by austenitizing, quenching, and then tempering [1-2], and their microstructures are usually tempered martensite, composed of the stable ferrite and cementite phases ($\alpha + Fe_3C$) [1-2]. The only effective way to heat treat the plain medium carbon steels is to allow heat treatment in a very thin section and at very rapid quenching rates. The ability of these alloys to be heat treated can be improved by adding chromium, nickel, and molybdenum. These heat-treated alloys are stronger than the low-carbon steels, but their ductility is lower.

1.1.3 High-Carbon Steels

Carbon constitutes from 0.6 to 1.4 wt% of the high-carbon steels. They are the hardest, strongest, and least ductile of the carbon steels. They are usually used in a

hardened and tempered condition, are wear resistant, and can hold a sharp cutting edge [1-2].

Despite their relatively limited corrosion resistance, carbon steels are used extensively in industry: in marine applications, nuclear and fossil fuel power plants, transportation, metal processing equipment, pipelines or other liquid transportation components, as well as in other applications such as toys and tools. Therefore, a better understanding of carbon steel corrosion in different environments might help predict their behaviour, which could improve the materials durability. The particular carbon steel utilized in this research has many industrial applications, such as within the nuclear power generation industry and the fabrication of nuclear waste containers.

1.2 Nuclear Power Generation

A prominent nuclear power plant design is the Canadian CANDU® (CANada Deuterium Uranium) reactor, which is a Pressurized Heavy Water Reactor (PHWR) [3]. Figure 1-2(a) shows a schematic of the key components of a CANDU® reactor: the fuel, the moderator, and the heat transport system (HTS). CANDU® reactors make use of natural, un-enriched uranium dioxide for fuel, and heavy water for the moderator and coolant [4]. The high neutron moderating efficiency of D_2O allows the un-enriched UO_2 to be used as a fuel. The Pressurized Light Water Reactor (PLWR) the most common reactor type in the USA and Europe, uses enriched uranium and light water as a moderator [4]. In either reactor system, the Heat Transport System (HTS) carries the coolant, in closed loops, between the reactor core and the steam generators. In the

CANDU® the HTS (highlighted in yellow in Figure1-2 (a)) inside the reactor core is composed of a horizontal array of fuel channels made of a zirconium alloy. On leaving the core, each channel is connected to a feeder pipe made of carbon steel of the type used in this research [4]. HTS in PWR has a pressure vessel which contains light water and there is no separation of coolant from moderator. Which in CANDU® due to pressure tube design the coolant is separated from the moderator (which is housed in the Calandria tank, as shown in Figure 1-2 (a) by the fuel channels. For safety purposes, a shielding tank containing light water surrounds the Calandria tank to minimize the radiation dose rates outside the reactor core [3-4].

As one of the possible degradation processes in reactor systems, the failure of carbon steel feeder pipes is an important operational and safety issue for the Canadian nuclear power industry [4]. Figure 1-2 (b) outlines the safety issues associated with feeder pipe degradation. Corrosion of carbon steel is expected to release corrosion products into the coolant which will circulate through the reactor core where they can be neutron activated and become radioactive. If the radioactive corrosion products are transported out of the core and deposited on the feeder pipe, the radiation level outside the reactor core can be significantly increased, potentially enhancing radiation exposure of maintenance operators during reactor shutdowns, avoidance of these exposures makes maintenance very costly. Stress corrosion and/or flow-accelerated corrosion of carbon steel could eventually lead to feeder pipe rupture [4]. For these reasons, it is crucial to understand how aqueous environments will influence carbon steel degradation in nuclear reactor environments, and, in turn, how carbon steel degradation, leading to release of corrosion products into the aqueous solutions, will influence the aqueous environment.

a)

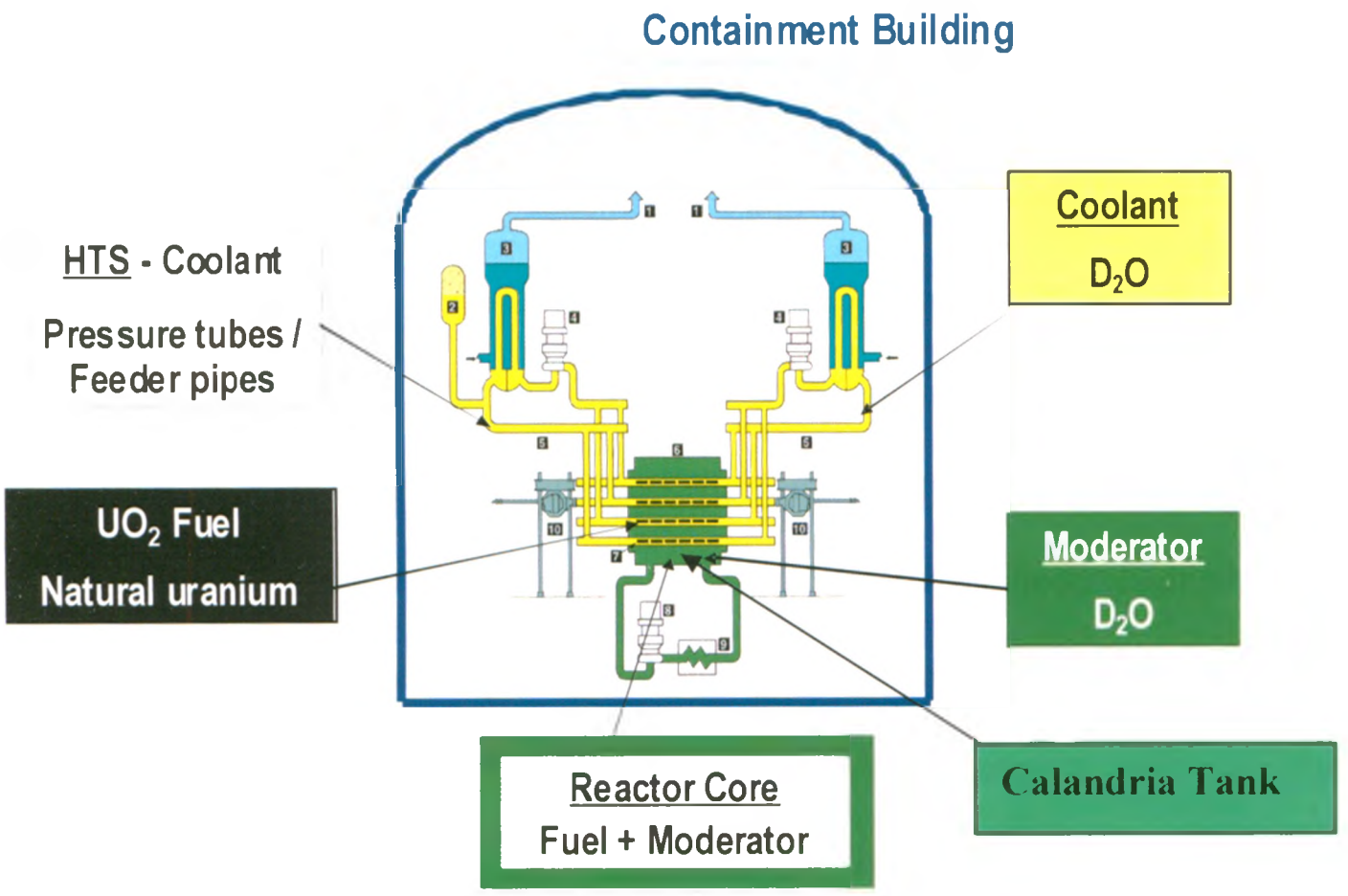

b)

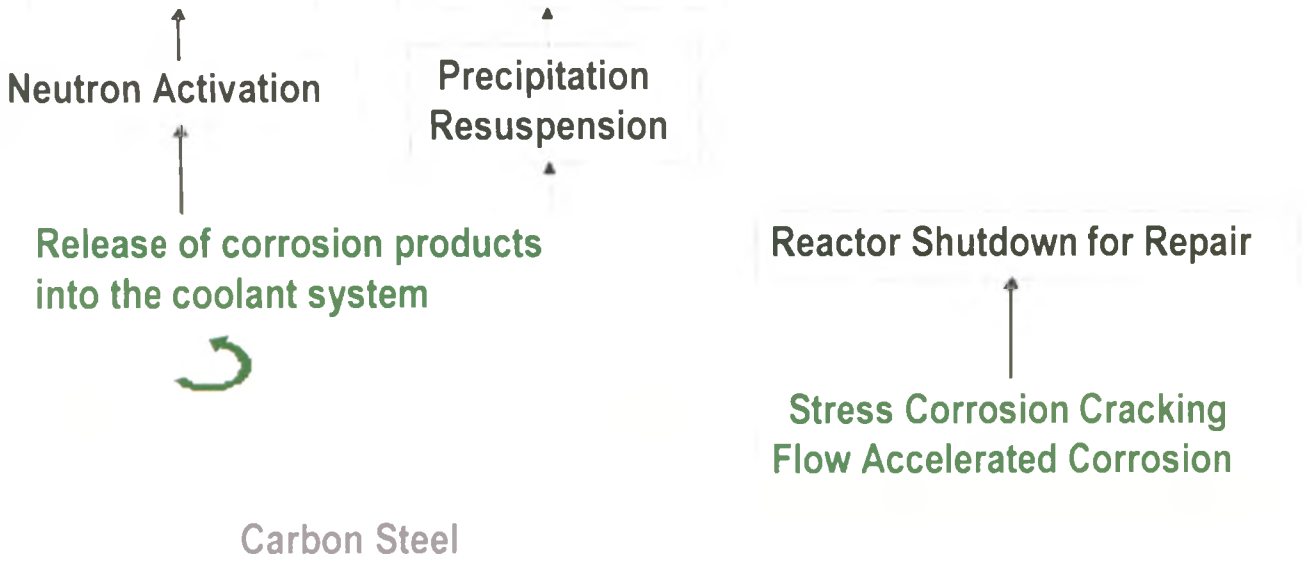

Figure 1-2 :(a) A Schematic of the Nuclear components of a CANDU® reactor; (b) Potential impacts of carbon steel pipe corrosion.[3]

1.3 Nuclear Waste Containers

Figure 1-3 shows a schematic of a proposed Canadian container design [6] for permanent nuclear waste disposal. One important feature of this design is the use of a carbon steel liner to structurally re-enforce the thin outer shell of copper. Copper is chosen to provide corrosion durability [6-7] in the groundwater environment anticipated in granitic repository environments (Canada, Sweden, Finland). Under these conditions a container would be subjected to hydrostatic and clay swelling pressures that will compress the ductile copper shell onto the rigid inner steel liner [8]. Since most of this external load will be transferred to the steel liner [8], the liner must withstand the combined loading stress of 15 MPa at 100 °C [8-11]. In Northern regions, it is also possible that the container will experience an additional hydrostatic load exerted by a period of glaciation above the repository. Therefore, the liner must be designed to withstand a total load of 45 MPa at 50°C. If the exterior copper shell were to fail, groundwater leakage into the container would lead to corrosion of the carbon steel. Research on the consequences of steel corrosion on subsequent container behaviour and the release of radionuclides from the fuel is underway [12-14].

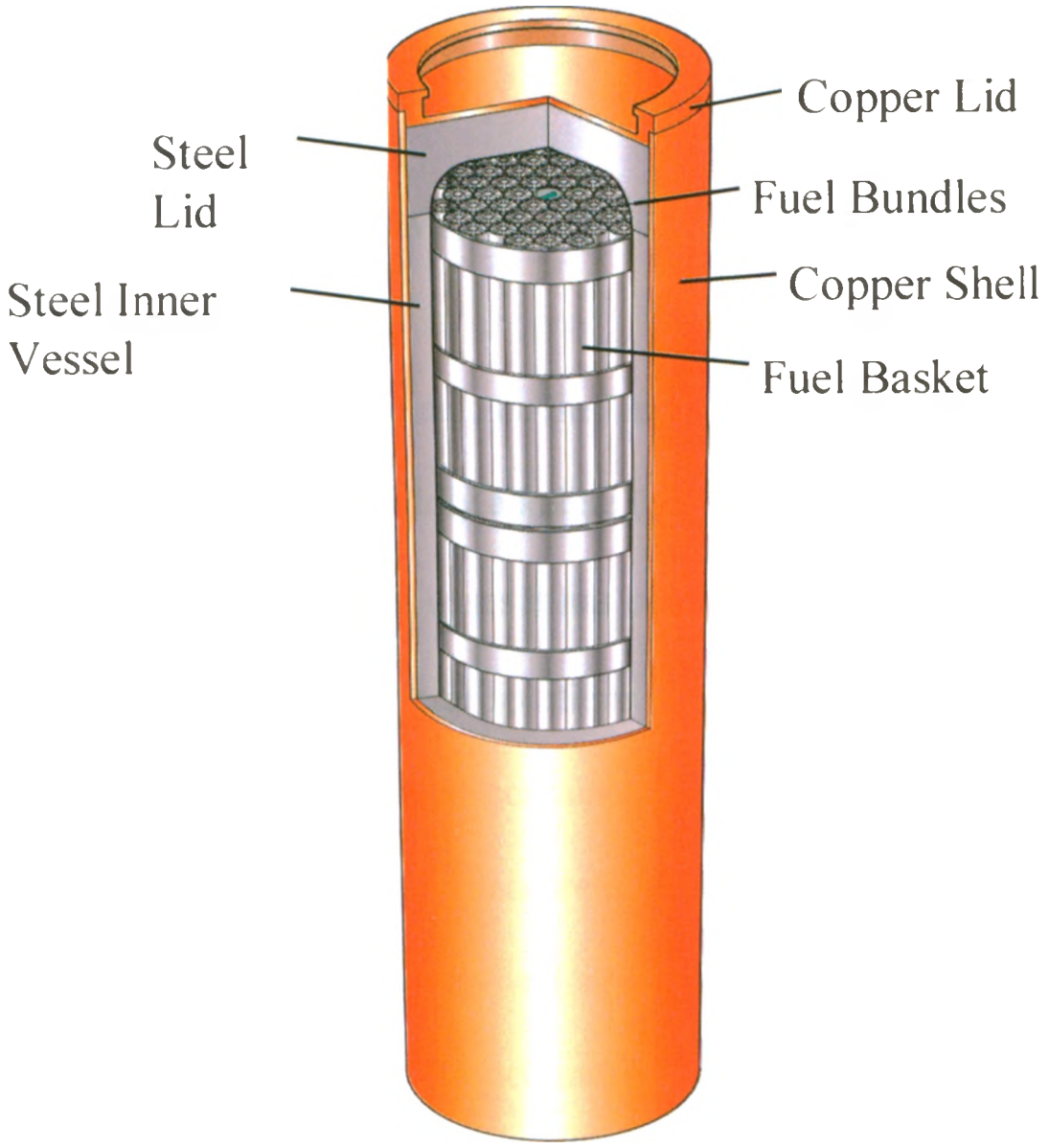

Figure 1-3 : Schematic diagram of the proposed nuclear waste container design showing the steel inner vessel, and steel inner baskets holding the used fuel. The container is about 1.2 m in diameter and 3.9 m long. [15]

Chapter 2

2 LITERATURE REVIEW

Extensive electrochemical studies have been carried out on the anodic and cathodic behaviour of iron in mildly alkaline (pH = 8.4) [16-21], and highly alkaline (pH $\geq$ 13) solutions [22-25]. In most cases it has been observed that the passive films formed on iron or steel surfaces in neutral solutions are ferric (Fe^{3+}) and ferrous (Fe^{2+}) oxide layers with hydrous compounds containing absorbed water [16-22]. For many applications, general corrosion measurements are suitable for the prediction of performance and lifetimes of iron or steel structures (e.g. cars, bridges, etc). However, in many cases, localized corrosion is much more relevant to a material's performance, since it can result in catastrophic failure of the material. High pressure systems are one such case, and these include gas cylinders, pipelines, nuclear reactors, etc. Unfortunately, only a small number of articles address the possibility of localized corrosion of iron in near alkaline solutions; to that end, this study has been conducted to examine this issue. First, it is instructive to review and define the pitting or localized corrosion process, and highlight some of the issues presented by research in this area.

A metal surface exposed to a corrosive environment may sustain attack at a number of isolated sites. If the combined area of these sites is considerably smaller than the total exposed surface area, the metal is said to experience localized corrosion. In this case, the rate of dissolution at these sites is much greater than that associated with

uniform corrosion, and structural failure may occur after a much shorter period than expected [26]. A number of different modes of localized corrosion have been identified. These depend upon the type of metal undergoing corrosion and the environment it is exposed to. One of the most destructive forms is pitting corrosion, which is characterized by the presence of small pits on the exposed metal surface. The geometries of the pits are determined by factors such as metal composition and surface orientation [27], and temperature [28]

Measuring the electrochemical conditions within such cavities poses many difficulties. Therefore, many different mathematical models have been developed to resolve them. Broadly speaking, these can be divided into three types depending on the stage of pitting the model describes: (1) the initial stage which entails such phenomena as passive film formation, film rupture under mechanical stresses, the influence of aggressive anions on the film breakdown, etc.; (2) early pit growth, involving processes that lead to the development of a self-perpetuating corrosion cell; (3) the propagation of the cavity involving mechanisms of ion transport in electrolytic solutions. It is not always clear where the separation between stages 2 and 3 lies.[29]

Localized corrosion tends to be rather unpredictable with respect to the time of initiation and the location of attack. However, certain specific chemical and electrochemical conditions need to be fulfilled prior to the initiation of localized corrosion on a metal surface. Generally, a thin adherent oxide film covers the metal surface, which limits corrosion uniform to a slow rate, largely determined by the thickness and solubility of the film. Many theories try to explain the formation and structure of this film and how corrosion occurs through it [20-31]. According to

Smialowska [30], the models for pit nucleation can be arranged into three main groups. In the first group of models it is suggested that, prior to pit nucleation, penetration of Cl^- through the film occurs without destroying the passive film [29-31]. Dissolution of the metal/pit initiation takes place when Cl^- reaches the metal surface. Another group of models proposes that "mechanical" breakdown of the passive film occurs before local dissolution of the metal initiates a pit [29-31]. The final group of models suggests that initiation involves local thinning of the passive film until the bare metal is revealed at the location of the ensuring pit [29-31]. While acknowledging these models Marcus et al., [31] have proposed a key role for film structure and the redistribution of potential in the pit initiation process. These will be described in detail in section 2.1.

A brief summary of the structure and properties of passive layers (especially of iron oxide films) is provided to establish a better basis for the discussion and understanding of corrosion mechanisms. The phenomenon of passive layer formation has been explained by Toney et al., [32], in great detail. The electrochemical event as a function of potential, are illustrated in Figure 2-1. This figure shows the idealized current potential curve for a passivating metal. As the potential is increased from a more negative to a more positive value, the metal exhibits an active region where it dissolves at a rate dependent on potential. However, at a critical potential, a passive film forms, which protects the metal from further dissolution resulting in a drastically lower current. This phenomenon has been extensively investigated since the 1700s, when it was first studied by Faraday [34] and Schonbein [35]. To date the exact atomic structure of iron passive films remain unresolved. However, electrochemical experiments and a number

of analytical methods including electron diffraction [36-38] have led to the suggestion that the film consists of an inner layer of Fe_3O_4 and an outer layer of γ-Fe_2O_3.

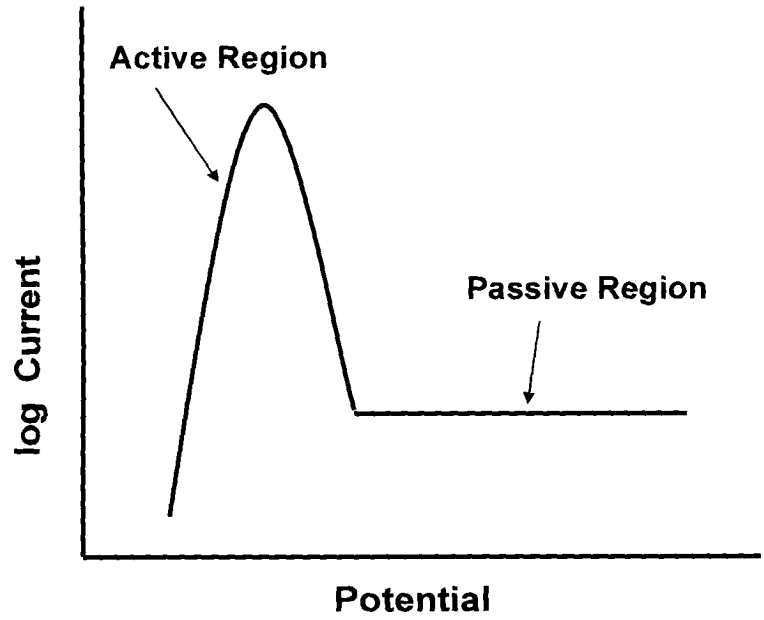

Figure 2-1 :A typical anodic polarization curve for a metal electrode undergoing passivation at a distinct anodic potential.

2.1 Model of Pit Initiation

Penetration Models: Many authors, [39-45] among them Evans [40], Rozenfeld et al.[41], Nishimura and Kudo [42], have proposed that a passive film is penetrated by chloride anions. Two classes of penetration model have been proposed: one suggesting that penetration of aggressive anions (particularly chloride) occurs through imperfections in the passive film, and the other suggesting that the penetration is

accompanied by some interaction of anions with the oxide lattice [30]. The penetration model proposed by Evans et al [40] in 1927 is of the first type. The small diameter of Cl^- enables it to permeate through a protective oxide film and breakdown the film when the aggressive anion reaches the bare metal. According to this model, adsorption of aggressive anion on the oxide film is the first step leading to passivity breakdown. For the second model Rozenfeld and Marshakov [41] suggested that the exchange of oxygen with chloride ion occurs at sites at the oxide-solution interface where the metal-oxygen bond is weakest. According to this theory, aggressive anions displace oxygen from the oxide surface and subsequently penetrate the passive film, and accumulate at the metal/oxide interface to cause a pit. In 1981, Nishimura and Kudo [42] advanced a model based on the two-layer concept of a passive film comprising an inner barrier layer and an outer deposited layer. It was proposed that pitting occurs in two steps. In step one, the incubation time period, chloride ions penetrate through fine pores in the deposited layer, which acts as an ion-selective membrane, to reach the barrier layer. In step two, called pit nucleation (initiation), the barrier layer fractures due to attack by Cl^-. This model does not explicitly specify whether this is a chemical or physical breakdown.

The penetration mechanisms require transfer of the aggressive anions through the passive layer to the metal-oxide interface, where they initiate metal dissolution. However, according to Strehblow [46], systematic study of this theory is still missing because relevant experiments are difficult to conduct. The limited area of pits and low quantities of aggressive anions are two reasons for this difficulty. Furthermore, it is unclear why the breakdown event occurs locally in passive films which have highly disordered structures. Since many sophisticated surface analytical methods such as XPS

have failed to detect the chloride ions in the barrier layer of the oxide film, the model involving Cl^- penetration through the passive film does not have sufficient supporting experimental evidence. However, using Auger electron Spectroscopy and Secondary Ion Mass Spectroscopy, Goetz and coworkers [47] claim to have demonstrated that Cl^- was not incorporated into the passive oxide film. Such results hamper the credibility of penetration mechanisms.

Passive Film Thinning Model: In 1967, Hoar and Jacob [48] proposed the film "thinning" model based on the formation of transient complexes for the pitting of austenitic stainless steel. Several years later, this model was also suggested by Heusler and Fischer [49] for iron. Their hypothesis was that specific adsorption of chloride leads to enhanced oxide dissolution at these absorption sites with subsequent thinning of the oxide film until the film is finally breached and active dissolution starts.

Strehblow [46] examined the thinning model using the rotating ring-disc electrode (RRDE) technique. The measurable increase in the release of Fe^{3+} ions from a prepassivated Fe electrode upon addition of Cl^- to the solution was used as a measure of locally enhanced dissolution of the oxide film. Such a release leads to an initial local thinning of the passive layer and finally to its complete breakdown and the formation of a pit. Khalil et al. [50] also proposed the nucleation of pits by a local thinning of the oxide film until the bare surface is exposed. However, Khalil et al [50] assumed that dissolution of the passive film occurs via the formation of soluble complexes. They believed the thinning of the oxide film starts by adsorption of aggressive anions on the oxide surface forming soluble complexes. Khalil et al. attributed the different

aggressiveness of halides to the different stability constants of the complex with the metal cations. [50].

Seo et al [51] proposed a slightly different model for the reduction of film thickness at sites where chloride ions agglomerate. They suggest that above a certain critical potential, potential-dependent oxide dissolution occurs, and pits form more rapidly than at locations covered by thinner films than by thicker films. By contrast, Bardwell and MacDougall [52] argued that a thinner film does not pit more rapidly than a thicker film. Clearly, they suggest pitting does not occur with a shorter induction time even though the film is thinner, but instead must await the growth of oxide to a critical state. Many authors, such as Hoar and Jacobs [48], Dalek and Foley [53], and others [54-56], support thinning of the oxide film as the cause of passive film destruction. All these researchers believe that localized dissolution is initiated by adsorption of aggressive anions and formation of soluble complexes with the cations at the oxide/solution interface. At a constant anodic potential, the electric field is increased across this interface at the thinned location on the film causing enhanced film dissolution until the bare metal surface is exposed. [54-56]

Smialowska [30] has pointed out that the thinning film model also has significant limitations. In fact, for many alloys and metals, pits nucleate at the metal/oxide interface, leaving an un-dissolved passive film above the pit. Goetz et al.[47], also mentioned that experiments performed below the pitting potential prove that the presence of Cl^- does not cause thinning of the passive film in borate solution.

Mechanical Breakdown Model: In 1947, Hoar [57-58] proposed that, when in contact with an aggressive electrolyte, an oxide film on metal can become mechanically stressed and damaged by pores and flaws generated from changes in interfacial forces. If metal cations are released inside the pores or flaws through oxidation processes, insoluble hydroxides or oxides can be produced through their interaction with water. Such hydrolysis processes are expected to lead to acidification, and this mechanism is autocatalytic because the cation dissolution rate is increased by the increased acidity. Hoar proposed two reasons for the increase of aggressiveness with an increasing Cl^- concentration: increased conductivity of the solution and decreased migration of OH^- ions into, and H^+ ions out of, pores.

Zaya [59] also proposed that a passive film continuously breaks and repairs, eventually leading to pitting when chloride ions reach and adsorb on the metal surface through the flaws. Mechanical breakdown of the film probably occurs with different energies at different spots on the film, and therefore, not all breakdowns are expected to lead to stable pit formation. Similarly, Marcus [31] maintains that when the electrode potential is suddenly changed stresses are caused within the film. At cracks within the passive layer, the current density will be that expected at the relatively positive potential with no protecting oxide present. However, only temporary Fe^{2+} formation of a few seconds' duration will occur as the passive layer self heals and, hence, to obtain a measurable quantity of Fe^{2+} from the unprotected metal surface, many such defects of nanometer dimensions within the passive layer would be necessary. In the absence of any aggressive anions, the temporary release of Fe^{2+} is not easy to measure. However, in the

presence of aggressive anions, their direct access to the metal surface will prevent repassivation and a pit can form.

2.2 Passivation of Iron and Pit Initiation in the Presence of Halide Ions

So far, however, no agreement has been reached on the atomic structure of this passive film, although, electron diffraction and electrochemical experiments [36-37,60-61] have led to the suggestion that the film consists of an inner layer of Fe_3O_4 and an outer layer of γ-Fe_2O_3: see further discussion in chapter 6. Such passive films, however, are often susceptible to pitting corrosion, which often occurs in the presence of aggressive anionic species, such as chloride. The reason for the aggressiveness of chloride and other halide anions has been pondered for some time. For example, chloride is a relatively small anion with high diffusivity and the anion of a strong acid, and many metal cations exhibit considerable solubility in chloride solutions. It is also frequently present as a contaminant.

Only a small number of papers discuss the pitting of iron in alkaline solutions. Oranowska et al [62], studied the behaviour of iron in a saturated $Ca(OH)_2$ solution at pH 12.5 with and without Cl^-. They noticed that in the presence of Cl^-, breakdown of passivity occurred by the spontaneous onset of uneven general corrosion, once the potential attained a critical value. Also, the film thickness in the presence of Cl^- was greater relative to that when it was not present. Tousek [63] also observed pitting of iron in 0.1 M KOH + 0.4 M KCl when the potential was shifted to a value situated above a critical potential. The effect of film thickness on the susceptibility of iron to pitting was

studied by McBee et al [64], who found that the thicker the passive film, the longer the time needed for its breakdown in NaCl solution. Passive film formation on iron and film breakdown in sodium hydroxide solution (pH = 12) containing chloride ion (0.05 M and 0.005 M) was studied by Zakroczymski et al [22]. They reported that the shape of the polarization curves was not influenced by the presence of chloride ions. Additionally, they found that pitting took place when the specimen was first passivated at a constant potential of 0.55 V (vs NHE) for 60 s, 120 s, 300 s in 0.05 M NaOH. However, pitting did not occur when chloride ions were added after 600 s and the potential maintained for 160 h. They claimed that, the time required for pit initiation was shorter when samples were electrochemically passivated for 5 min than for 10 min. A longer passivation often resulted in no pitting, indicating changes in the protective properties of the passive film occurred over time. Also, it was confirmed that pitting is a probabilistic event that may or may not happen. Furthermore, Zakroczymski et al. noticed that pitting did not occur at potentials lower than about 0.25 V (vs NHE). [22]

DeCastro and Wilde [65] studied the anodic dissolution behaviour of iron in halide solutions at both stationary and rotating electrodes in 1 M LiBr and LiCl at pH 8. Active dissolution kinetics was reported for stationary electrodes, whereas with rotating electrodes an active/passive transition was observed. They claimed that the pitting potential was independent of halide ion concentration and electrode velocity, indicating that hydrodynamic factors are not important in the pit initiation process. However, pit propagation was markedly influenced by rotation. Bardwell et al [66] analyzed the initiation of pitting on iron in acetate and borate solutions containing 1 M halide ions at pH = 8.4 and pH = 7.4, and reported that, for potentials below the pitting potential, the

current transients recorded at constant potential exhibited the same behaviour in the absence or presence of halide. This shows the kinetics of film growth in the two solutions is similar. Only after pitting had initiated did the current in halide-containing solution begin to show a positive deviation from that in halide-free solution. This led to the assumption that pitting initiated at the point of the deviation.

In their work Ahn and Macdonald [67] examined the role of chloride ion in passivity breakdown on iron at pH = 8.5 at a concentration of 0.1 M NaCl. They found that the Cl^- ion acts only at the barrier layer/solution interface and neither penetrates nor incorporates into the film. Furthermore, they reported that if penetration and incorporation of chloride ions occurred, changes in the structure and composition (and, thus, also in the electronic and optical properties) of the film would be likely to occur. Such changes would be caused by the substantial difference in size between Cl^- (Pauling radii of 0.181 nm) and O^{2-} (Pauling radii of 0.140 nm). This suggests that passivity breakdown on iron is not directly related to the oxygen vacancy and/or the cation interstitial, whichever is the dominant. According to Ahn et al., the condensation of metal vacancies at the metal/film interface is responsible for the passivity breakdown.[67]

Bardwell and MacDougall [68] studied the involvement of surface oxide films on iron in halide-induced pitting in borate buffer at pH = 8.4 with a halide concentration of 0.0945 M. They found a linear correlation between the logarithm of the halide ion concentration and the critical thickness of pitting, and the slopes are similar in two cases (Cl^- and Br^-). As the halide concentration increased, the solution becomes more aggressive and less anodic charge must pass before pitting begins. By using SIMS analyses [68] in halide and halide-free solutions they proved that the passive film on Fe

grows at the same rate in both solutions. Clearly, neither Br^- nor Cl^- is being incorporated into the film in any significant degree during the induction period.

Bardwell et al., [66] studied the behaviour of iron in neutral pH buffered solution and reached the conclusion that pit initiation is, to a great extent, determined by the nature of the passive film. Having performed the experiment in halide-free buffer and halide-containing buffer, they found that the kinetics of film growth in the two solutions were very similar. Not until after pitting had initiated did the current in halide-containing solution begin to display a positive deviation from that in halide-free solution. Therefore, it is safe to surmise that pitting initiates at the point of deviation between the two curves.

Sieber et al., [16] investigated the passivity of iron in borate and phosphate buffer at pH = 8.4 in halide-free solutions. They found that the passive films formed on iron in neutral solution are ferric and ferrous oxide layers with hydrous compounds including adsorbed water. This agrees with the result of Zakroczymski and his coworkers [22]. Sieber et al. suggested that pitting of iron can occur in the presence of Cl^- when the passive film is not yet sufficiently consolidated, i.e., when it probably contains a substantial amount of incorporated water. Also, Revie et al. [69] found that the passivation of iron in chloride containing solutions leads to the incorporation of a greater amount of water in the film than is the case in Cl^--free borate solutions. Lochel and Strehblow [70] studied the nucleation of corrosion pits on passive iron and other metals using rotating split-ring-disc-electrodes. They proved that for non-stationary conditions passive film breakdown is favoured. If aggressive anions are present in the electrolyte at a sufficient concentration, they have direct access to the bare metal surface to prevent repassivation, allowing the formation of a corrosion pit.

To date, there are many theories that try to explain pit initiation and the film breakdown through passive films. No model can thoroughly explain the cause of passive film breakdown and pit initiation in the presence of anions (e.g. Cl^-). It has been proven by many researchers that pit initiation is, to a great extent, determined by the nature of the passive film. When aggressive anions are present at sufficient concentrations they may have direct access to the bare metal interfere to interface with the re-passivation process leading to pit propagation. Such an event leads to a corrosion pit, but this does not define the role of the anions during the initiation process. This work attempts to define the anion role in the initiation stage.

2.3 Goals of the Research

The goals of the research are to investigate the passive film breakdown on oxide-covered carbon steel in solutions containing aggressive anions (e.g. Cl^-, Br^-, I^-) and also to establish the role of the film properties on pit initiation. The experimental approach taken was to apply different electrochemical potentials to reproduce different redox environments, since electrochemical techniques are extremely sensitive and easy to control, and very useful to follow the reaction kinetics of redox active surfaces. Various electrochemical techniques, including cyclic voltammetry (CV) and potentiostatic film growth (PS) measurements and electrochemical impedance spectroscopy (EIS) were used to study the oxide film formation and film breakdown process. These electrochemical techniques were complemented by various surface analyses techniques such as Ex situ and in situ Raman spectroscopy, scanning electron microscopy (SEM), energy dispersive x-ray and x-ray photoelectron spectroscopy (XPS) to characterized oxide film properties.

Chapter 3

3 LITERATURE REVIEW FOR EXPERIMENTAL TECHNIQUES

3.1 Cyclic Voltammetry (CV)

Cyclic voltammetry is a potentiodynamic technique that allows the general electrochemical reactivity of a system to be rapidly examined. In this technique, the potential of the working electrode, WE (compared to the reference electrode, RE) is scanned between two limits as a function of time, and the current that flows between the WE and counter electrode (CE), is recorded (see Figure 3-1). In our experiments the forward scan is positive-going (i.e. from a more negative potential terminus to a more positive one), during which oxidation of the electrode surface may occur as the potential of the WE becomes more positive than the equilibrium potential for a specific electrochemical reaction. During the reverse (negative-going) scan, reduction of the oxidation products becomes thermodynamically possible once the potential is more negative than the equilibrium potential for a specific electrochemical reaction. For both the positive and negative scans, the occurrence of electrochemical reactions can be both thermodynamically and kinetically controlled.

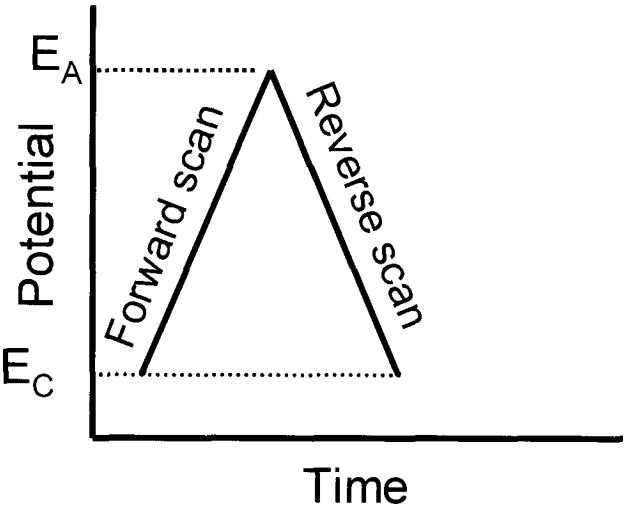

Figure 3-1 :Schematic of the potential-time profile used in cyclic voltammetry: E_C and E_A are the cathodic and anodic limiting potentials, respectively.

The magnitudes of charges accumulated in the anodic and cathodic scans will only be equal if the oxidation reactions that take place during the anodic scan are electrochemically reversed on the cathodic scan (i.e., if the oxidation products on the electrode surface are fully reduced). There are two possible reasons for the oxidation charge being greater than the reduction charge: 1) The oxidation product is kinetically irreducible; and 2) The oxidation products are lost from the electrode.

In this work, reversibility would require that the oxidation products of iron not be (1) soluble Fe^{2+}, (2) oxides which are difficult to reduce such as Fe_3O_4, or (3) oxides which undergo incomplete reduction on the timescale of the CV experiment. Within this context, currents seen in a CV can illustrate the separate oxidation processes occurring; i.e. can be useful in identifying the potentials at which various oxides/hydroxides grow.

3.2 Potentiostatic Film Growth

In potentiostatic film growth experiments, a constant external potential is applied to the WE and maintained for a certain length of time, during which the resulting current is measured. Changes in current with time provide insight into the changes occurring on the WE surface.

Since it is generally known [36-37,60-61] that oxidation occurs on iron through the formation of either magnetite (Fe_3O_4), maghemite γ-(Fe_2O_3) or lepidocrocite γ-FeOOH, and other oxyhydroxides and oxides, at anodic potentials, we can, in principle, use potentiostatic oxidation to study film growth, breakdown and dissolution at specific potentials. The applied potential will affect the composition of the film grown, so an appropriate potential can be chosen, based on the results of cyclic voltammetric experiments, and the anodic current measured as a function of time. The current is a measure of the overall reactivity, and the change in current with time yields information on the film growth mechanism (Figure 3-2 a-d).

These plots show the expected behaviour of the current as a function of time for specific electrode processes. Plot (a) shows the expected current when no protective layer of oxide film is formed on the surface of the electrode, and metal dissolution takes place at the constant current expected at this potential. Plot (b) shows the current-time relationship expected when a passive film forms and efficiently protects the metal from anodic dissolution. In this mechanism the current decreases exponentially. Plot (c) shows the current behaviour when either a slightly soluble or an incomplete (porous) passive oxide film grows on the surface of the electrode. At short times the current decays with time as the film grows on the electrode. At longer times, the current reaches

a steady-state due to dissolution at a constant rate. Such a long term steady-state current will be observed if the chemical dissolution rate of the oxide film at the oxide/solution interface is balanced by its electrochemical (anodic) formation at the metal/oxide interface. It will also be observed if the film is porous and dissolution can occur through the film. Finally, plot (d) illustrates the current-time behaviour when pitting occurs. Initially the film grows, as illustrated in (b), with the current decreasing exponentially with time until film breakdown occurs. At this point the current increases irregularly to a higher value and continues to increase as the pit(s) grow(s). Integration of the current with respect to time yields the charge passed which can be used to calculate the total amount of oxidation which occurred, and possibly the extent of oxide formation, and (if the oxide density is known) the film thickness.

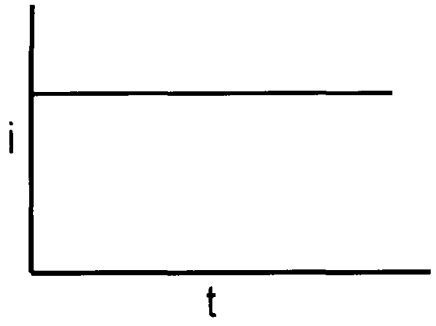

a) Metal dissolution

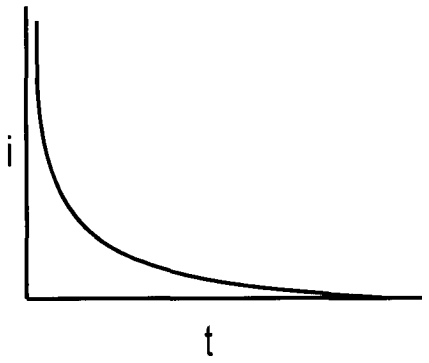

b) Growth of a passive film

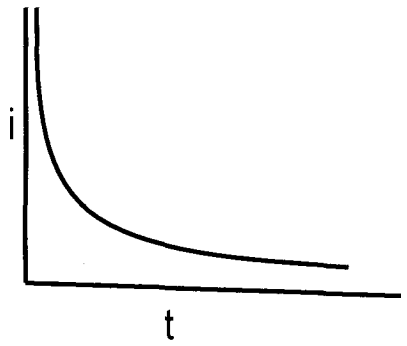

c) Growth of a porous film or a film with a measurable dissolution rate

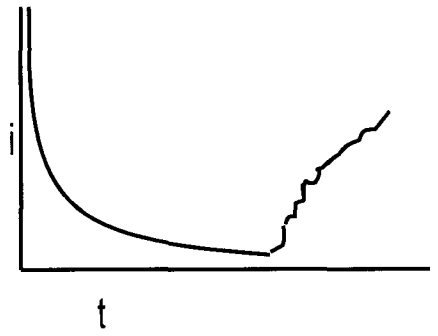

d) Growth of a film followed by film breakdown and pitting

Figure 3-2 :Current behaviour expected as a function of time for different reactions occurring on a reactive metal surface

3.3 Electrochemical Impedance Spectroscopy (EIS)

EIS can be a useful method for characterizing the properties of electrochemical and corrosion interfaces. It is particularly useful in the characterization of oxide-covered metal surfaces. This technique, as illustrated in Figure 3-3, involves the application of a small sinusoidal potential (E_{ac}) perturbation ($\leq \pm$ 10 mV) superimposed on a dc potential (either an applied or corrosion potential).

$$\mathbf{E_{ac} = E_0 \sin(\omega t)} \qquad \textbf{3-1}$$

to the electrode/solution interface, and the measurement of the resulting sinusoidal current I_{ac} which occurs at the same frequency, but, depending on the characteristics of the interface, may be shifted in phase θ

$$\mathbf{I_{ac} = I_0 \sin(\omega t + \theta)} \qquad \textbf{3-2}$$

In these equations, E_{ac} is the ac potential at time t, E_0 the ac potential amplitude, ω the angular frequency in radian/s, θ is the phase shift, and I_0 the ac current amplitude.

In general, an electrochemical interface can be represented by an electrical equivalent circuit composed of resistors, capacitors, and other electrical elements, such as a Warburg impedance. For a metal/metal oxide/aqueous solution system, the system

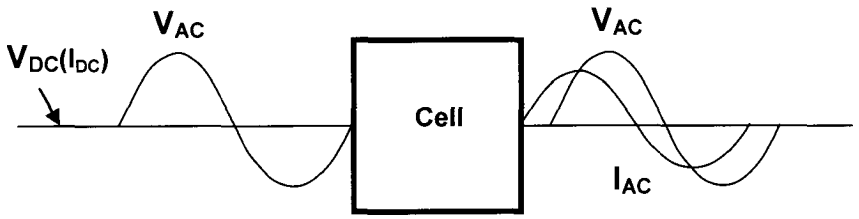

Figure 3-3 :The relationship between the input alternating voltage and the resulting output alternating current in an EIS experiment.

resistance (i.e. in-phase response) is a combination of the resistances of the metal/oxide and oxide/solution interfaces, the oxide film resistance, and the solution resistance. Capacitances may result from the build up of stored charges at the oxide/solution and/or metal/oxide interfaces and the polarization of dipoles in the oxide film. Of these various equivalent circuit elements, only specific components are often detected, depending on their relative magnitudes and characteristic frequencies. For example, large individual resistances are dominant when several resistances are in series, while small resistances are dominant when resistances are in parallel [72].

Figure 3-4 shows the simplest single time constant equivalent circuit, the Randles circuit, that can be used to characterize an electrified interface [72]. In general terms, for "active" (dissolution of metal) interfaces, the expected circuit components are the solution resistance, the double layer capacitance and the charge transfer resistance for dissolution. For a uniformly passive surface (when a thin oxide film forms and prevents

further dissolution), the circuit components represent the solution resistance (R_s), the capacitance of the oxide film (C_{ox}), and the resistance of the oxide film, (R_{ox}).

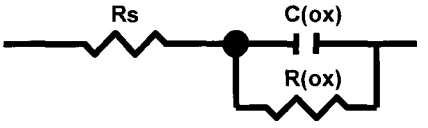

Figure 3-4 :A simple electrical equivalent circuit (one time constant) which can be used to simulate the properties of an oxide-covered electrode.

The impedance (Z) of this interface is a function of the frequency (ω) of the sinusoidal potential input and is often expressed using a complex function:

$$Z(\omega) = Z_{\mathrm{Re}}(\omega) - jZ_{\mathrm{Im}}(\omega) \qquad \textbf{3-3}$$

where j = $(-1)^{1/2}$, and Z_{Re} and Z_{Im} are the in-phase and out of phase impedances, respectively. Thus the resistance (R) corresponds to the real (in-phase) component of the impedance, and the capacitance (C) to the imaginary (out of phase) component. Therefore, the individual impedances in equation 3-3 can be expressed as:

$$Z_{\mathrm{Re}}(\omega) = R \qquad \text{and} \qquad Z_{\mathrm{Im}}(\omega) = \frac{1}{\omega C} \qquad \textbf{3-4}$$

The total impedance, $|Z(\omega)|$, is then given by

$$|Z(\omega)|^2 = Z_{\mathrm{Re}}(\omega)^2 + Z_{\mathrm{Im}}(\omega)^2 = \frac{R^2 + \omega^2 C^2}{\omega^2 R^2 C^2} \qquad \textbf{3-5}$$

Usually, impedance data are plotted in one of two ways: either as a Nyquist plot or as a pair of Bode plots. In a Nyquist plot, Figure 3-5, the real component of impedance is plotted against the imaginary component, for the Randles circuit shown above in Figure 3-4. The R_{ox}-C_{ox} circuit representation yields a semicircular plot when the selected frequency range is suitable. The extrapolation of such a plot to the real axis as $\omega \rightarrow 0$ yields the total resistance of the interface; and the larger the semi-circle, the higher the interfacial resistance. The existence of more than one semi-circle in the impedance spectrum indicates the presence of more than one time constant (or R-C component) requiring a more complicated equivalent circuit than that shown in Figure 3.4. Bode plots are generally presented as a pair: a plot of log of the absolute impedance $|Z|$, vs. the log of frequency, and a plot of the phase angle (θ) vs. the log of frequency, as shown in Figure 3-6

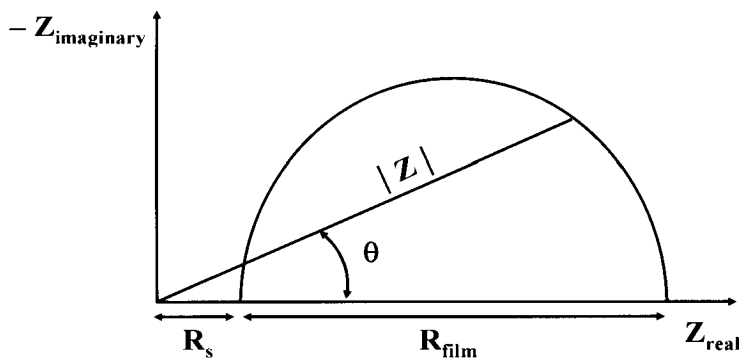

Figure 3-5 : The impedance spectrum plotted in the Nyquist format, for the circuit shown in Figure 3.4.

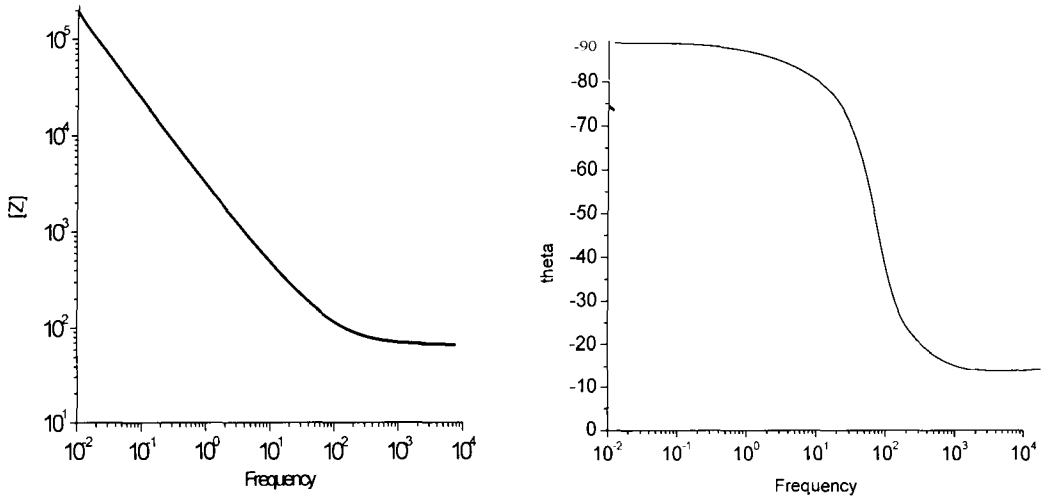

Figure 3-6 : The impedance spectrum, plotted in the Bode format, for the circuit shown in Figure 3.4.

The Nyquist and Bode plots yield information on how the system is behaving. For example, for the circuit shown in Figure 3-4, at very high frequencies there is no time for charge to build up on a capacitor and the solution resistance can be determined readily. At very low frequencies the capacitor charges and discharges rapidly compared to the frequency used and is, hence, undetectable. Therefore, the resulting impedance measurement is due to the total resistance of the system, for example, $R_S + R_{ox}$ for the circuit shown in Figure 3.4. In between the low and high frequency extremes, both resistance and capacitance will contribute to the impedance, and the out-of-phase behaviour is observed.

Commonly, more than one equivalent circuit can fit a set of impedance data. However, the simplest possible circuit that can reasonably fit the data is generally used.

To extract meaningful information from such an equivalent circuit fit, the individual circuit elements must be interpretable in terms of the electrochemical properties of the electrode interface.

3.4 Surface Analyses

3.4.1 X-Ray Photoelectron Spectroscopy (XPS)

X-ray photoelectron spectroscopy (XPS), also known as electron spectroscopy for chemical analysis (ESCA), is a surface sensitive technique which can yield atomic and molecular information about the outer 3 to 10 nm of the surface of materials, as well as providing a quantitative analysis of the surface composition [74-78]. XPS is based on the photoelectric effect, [77]. The sample is ionized using low energy X-rays (also referred to as soft X-rays), which have energy sufficient to remove core and valence electrons. Photoelectrons are ejected from core and valence levels of the atoms in the surface after direct energy transfer to the atoms, Figure 3-7, as a relaxation mechanism for the ionized species formed as a result of the absorption of the x-ray energy [78].
The measured kinetic energy, E_K, of these photoelectrons depends on the energy of the X-ray, $h\nu$, and the electron binding energy, E_B. The maximum kinetic energy, E_K, of the ejected electrons is given by:

$$\mathbf{E_K = h\nu - E_B} \qquad \textbf{3-6}$$

where h is the Planck constant (6.62×10^{-34} J·s), and ν is the frequency (Hz) of the

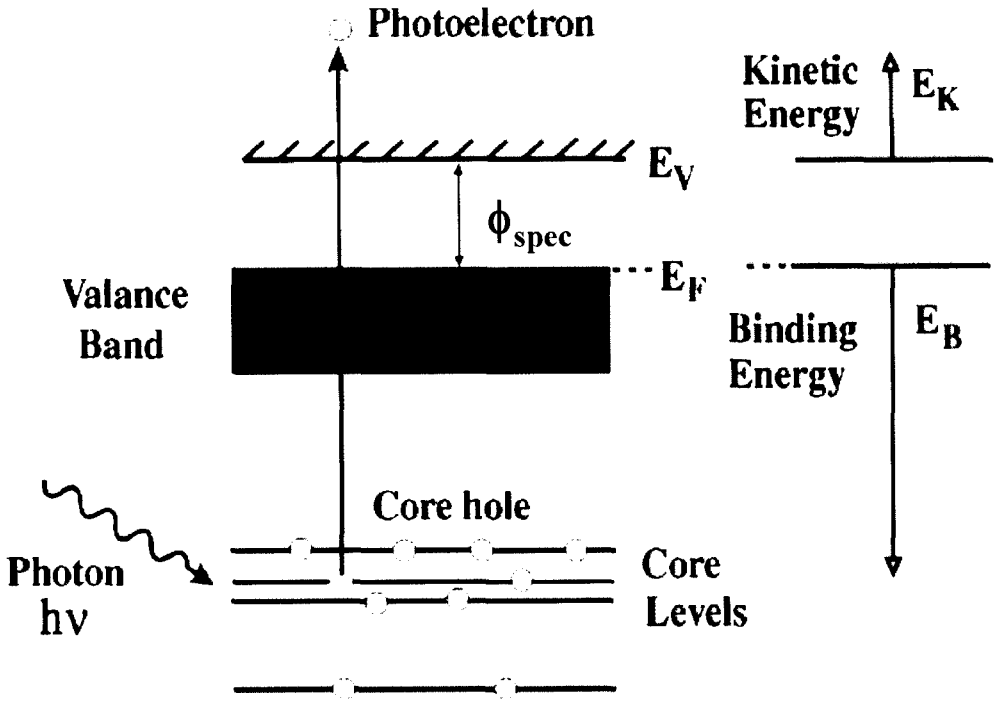

Figure 3-7 :Schematic representation of the excitation of a core level electron, and subsequent photoelectron generation in XPS. The kinetic energy of the photoelectron (E_K) is the difference between the X-ray energy (hν) and the binding energy of the electron (E_B) plus the work function of the spectrometer, $\phi_{spectrometer}$ [78]

radiation. The binding energy, E_B, is partly determined by the chemical environment of the atom, but mostly by the ionization energy of the electron energy level. This combination makes XPS useful in identifying the nature and oxidation state of atoms in surface films, in addition to identifying individual atomic species.

Since the binding energies of electrons in bulk materials are usually measured in relation to the Fermi-level, rather than the vacuum level, a correction to equation 3- 6 is needed to

account for the work function of the sample and the electron energy analyzer. Thus, the experimentally measured energies of the photoelectrons are given by:

$$\mathbf{E_K = h\nu - E_B - (\phi_{spectrometer})} \qquad \textbf{3-7}$$

The precise energy relationship can be determined for a photoelectron emitted from a conducting sample in electrical contact with the spectrometer, as illustrated in Figure 3-8. It can be seen that the work function of the sample is one of the energy steps to be overcome in moving an electron from a core level in the sample to the vacuum level (away from all electrostatic influences of the atom).

Since the spectrometer recaptures ejected photoelectrons, the sample work function term is cancelled because both the sample and spectrometer Fermi levels are the same (i.e. they are in electrical contact). While X-ray penetration depth can be quite large [75], electrons escaping from a sample have a low inelastic mean-free path (λ_m). Thus, XPS can be regarded as a surface sensitive technique, with most photoelectrons escaping from a depth of between 0.5 and 3.0 nm [75], although the maximum depth is generally quoted to be 10 nm.

An XPS spectrum plots the measured photoelectron intensity as a function of kinetic energy. The resultant spectrum is then often replotted as a function of binding energy using equation 3-7 and known values for $\phi_{spectrometer}$ and the frequency (ν) of the x-ray radiation. For every element, there is a characteristic binding energy associated with each atomic orbital, producing a characteristic set of peaks in the photoelectron spectrum.

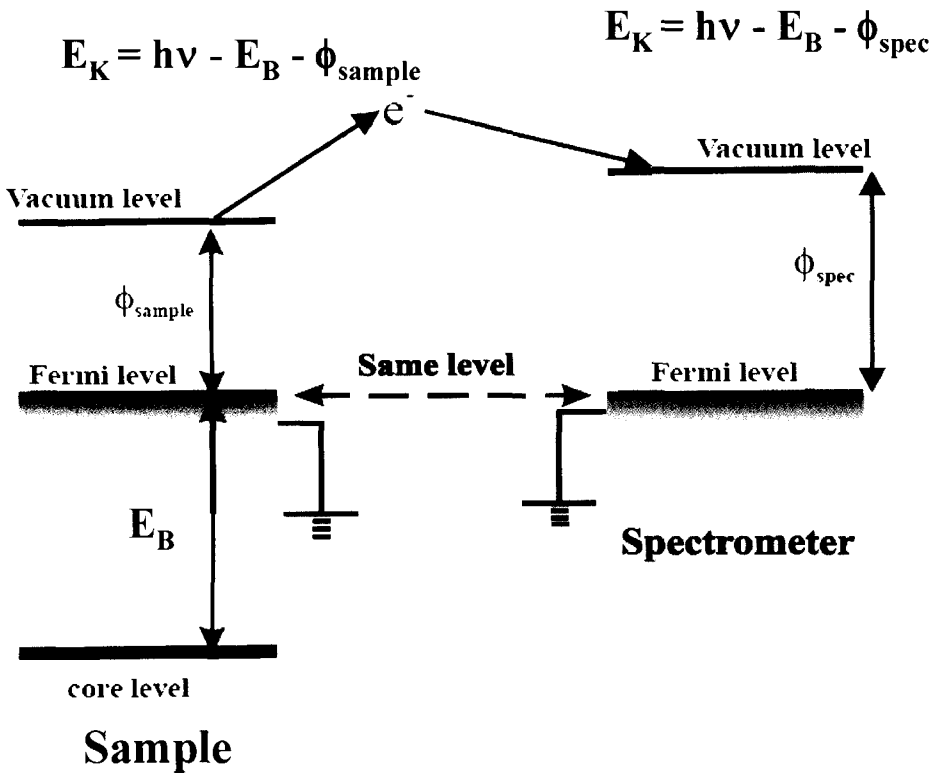

Figure 3-8 : Schematic process for the removal of an electron from a sample in an XPS spectrometer.

Thus, XPS is a very useful tool for elemental analysis of the outermost surface layers.

Another valuable feature of XPS is its ability to distinguish between oxidation states and/or the chemical environment of an element. The exact binding energy of a given electron depends not only upon the level from which photoemission occurs, but also upon the oxidation state of the atom and the local environment (i.e. neighbouring

ligands). These slight differences of energy levels appear as small shifts in the peak positions in the binding energy scale, and are termed chemical shifts. Distinct chemical states, which are close in energy, can be deconvoluted by obtaining high-resolution spectra of individual energy regions and using peak fitting programs to give the percent composition of each state.

3.4.2 Scanning Electron Microscopy/ Energy Dispersive X-ray Spectroscopy (SEM/EDX)

Scanning electron microscopy (SEM) is used mainly to study surface topography at higher magnifications and with better depth of field than can be achieved using optical microscopy. SEM results can be easily combined with techniques that provide data on the chemical composition of materials, such as energy dispersive X-ray spectroscopy (EDX)[75-79]. SEM has many advantages over optical microscopy, especially the ability to achieve higher magnification and to obtain depth resolution. The resolution by SEM can approach a few nm and the magnification can be easily adjusted from about 10 to 300,000 X, vs. 500 X for optical microscopy [79].

With conventional SEM, a source of electrons is focused to a narrow beam in high vacuum.(10^{-6} Torr), which then scans the sample surface. The electrons are generated by thermionic emission from a metal filament, and accelerated to 0.5 to 30 keV using magnetic fields. A system of electrical and magnetic field optics is used to focus the beam to a spot < 10 nm in diameter on the sample surface. As the electrons interact

with the surface, several processes can occur that result in the emission of electrons or photons from the surface. The general system configuration is shown in Figure 3-9.

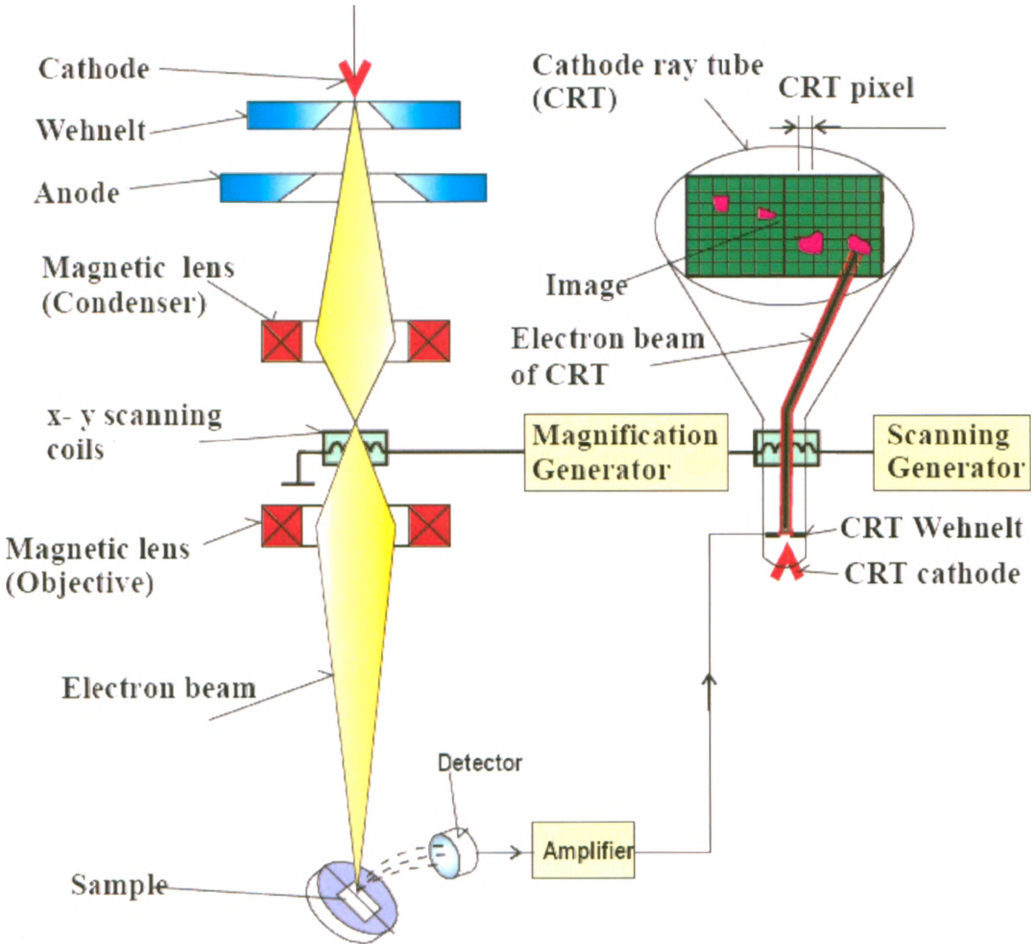

Figure 3-9 : Schematic diagram of a Scanning Electron Microscope.

There are three kinds of images produced by SEM: secondary electron images, backscattered electron images, and elemental X-ray images [79-80]; although combinations of hardware and software can make combinatorial images containing

multiple components of each of these. Secondary and backscattered electrons are produced by different interactions, so they are typically separated according to their respective energies. Secondary electrons are produced through inelastic collisions, as some energy is transferred to the surface, so electrons are emitted with less energy than the electron beam. The majority of the emitted secondary electrons are produced within the first few nm of the surface [80], since secondary electrons produced much deeper in the material are subject to additional inelastic collisions. The intensity of these secondary electrons is to a great extent determined by the surface topography of the sample and they are able to leave the surface if their energy is greater than the work function of 2 to 6 eV.

Primary electrons that have been scattered with no loss of kinetic energy (i.e., elastically) by the nucleus of an atom are backscattered electrons. In this case, the higher the atomic number of a material, the greater the likelihood of backscattering [79]. Consequently, with a beam passing from a low-Z (atomic number) to a high-Z region, the signal due to backscattering, and thus also the image brightness, will increase, allowing a qualitative differentiation between atomic species; a difference that is enhanced as the difference in atomic number is increased. Chemical compounds such as oxides would backscatter according to the weighted average of the combined elements' content; hence differentiation between metal and metal-oxide is generally possible using backscattered electrons.

Another important electron interaction in the SEM occurs when the primary electron comes into collision with, and dislodges, a core electron from an atom in the solid. The excited atom will relax to its ground ionized state and reduce its energy through the ejection of either a characteristic X-ray photon or an Auger electron. For

SEM, the X-ray emission signal can be arranged by wavelength with a wavelength spectrometer or, more commonly, by energy with an energy dispersive X-ray (EDX) detector, and these distributions are characteristic of the atomic energy levels of the elements that released them. Software on the SEM/EDX can be utilized to create elemental images showing the spatial distribution of specific elements in the field of view. Since primary electrons can penetrate to considerable depth into a solid and the X-ray photon can easily escape, X-ray emission will occur from a large volume of the sample.

3.4.3 Raman Spectroscopy

Raman spectroscopy is an analytical technique that makes use of light scattering, the properties of which are described below. Light scattering is a light-particle interaction that occurs according to equation 3-8:

$$\mathbf{I}_{\text{scattering}} \approx \mathbf{h}\,\nu^4 \qquad \textbf{3-8}$$

where I is the intensity, h is the Planck constant and ν is the light frequency. This frequency dependence is responsible for the blue colour of the sky. When the full spectrum emitted by the sun interacts with gases in the atmosphere, the blue light scatters significantly more intensely than visible light of lower frequencies. As a result, more blue light is directed downward from the sky, rather than along its original path through

the atmosphere. This change in direction of the photon is what defines a scattering event, and the scattered photons emerge from the interaction traveling in all directions.

Various types of scattering can be distinguished [81]; however, this discussion will be limited to Rayleigh, Stokes and Anti-Stokes scattering. The scattering of sunlight by the atmosphere, as described above, is the first type, Rayleigh scattering. Rayleigh scattering is an elastic scattering event, in which an incident photon interacts with a molecule, and emerges at the same frequency Figure 3-10 (a). In addition to this process, Stokes and Anti-Stokes scattering are inelastic scattering events in which the incident photon gains or loses energy upon the interaction. Stokes scattering occurs when the photon loses energy to the molecule, leaving the molecule in typically an excited vibrational state Figure 3-10 (b). For this process, the energy gained by the molecule can be calculated as:

$$\triangle E_{vibration} = E_0 - E = h\nu' \qquad \textbf{3-9}$$

where E_0 is the incident photon energy, E is the emitted photon energy and ν' is the frequency of the vibrational event. Similarly, Anti-Stokes scattering occurs when the photon takes energy from the molecule that is already in an excited vibrational state, and leaves the molecule in a lower vibrational state Figure 3-10 (c). This is accompanied by emission of a photon with energy $E = h(\nu + \nu')$, a higher frequency light. In this case

$$\triangle E_{vibration} = E_0 - E = -h\nu' \qquad \textbf{3-10}$$

Detection of the Raman processes is accompanied by observing the scattering of UV or visible light at either higher or lower frequencies than the incident light. Since most species are in their vibrational ground states at room temperature, Stokes scattering is more widely used in Raman analysis. For Raman, it is the shift in frequency i.e., ν' Equation 3-9 and 3-10 that provides information on the vibration energy states of the molecule, and hence the types of species present on the surface of the specimen under examination. A large number of molecules are Raman active and exhibit characteristic Raman shifts which can be used as fingerprints to aid in their identification. This feature, and the fact that water is Raman inactive, make Raman spectroscopy a useful surface analytical technique for corrosion studies.

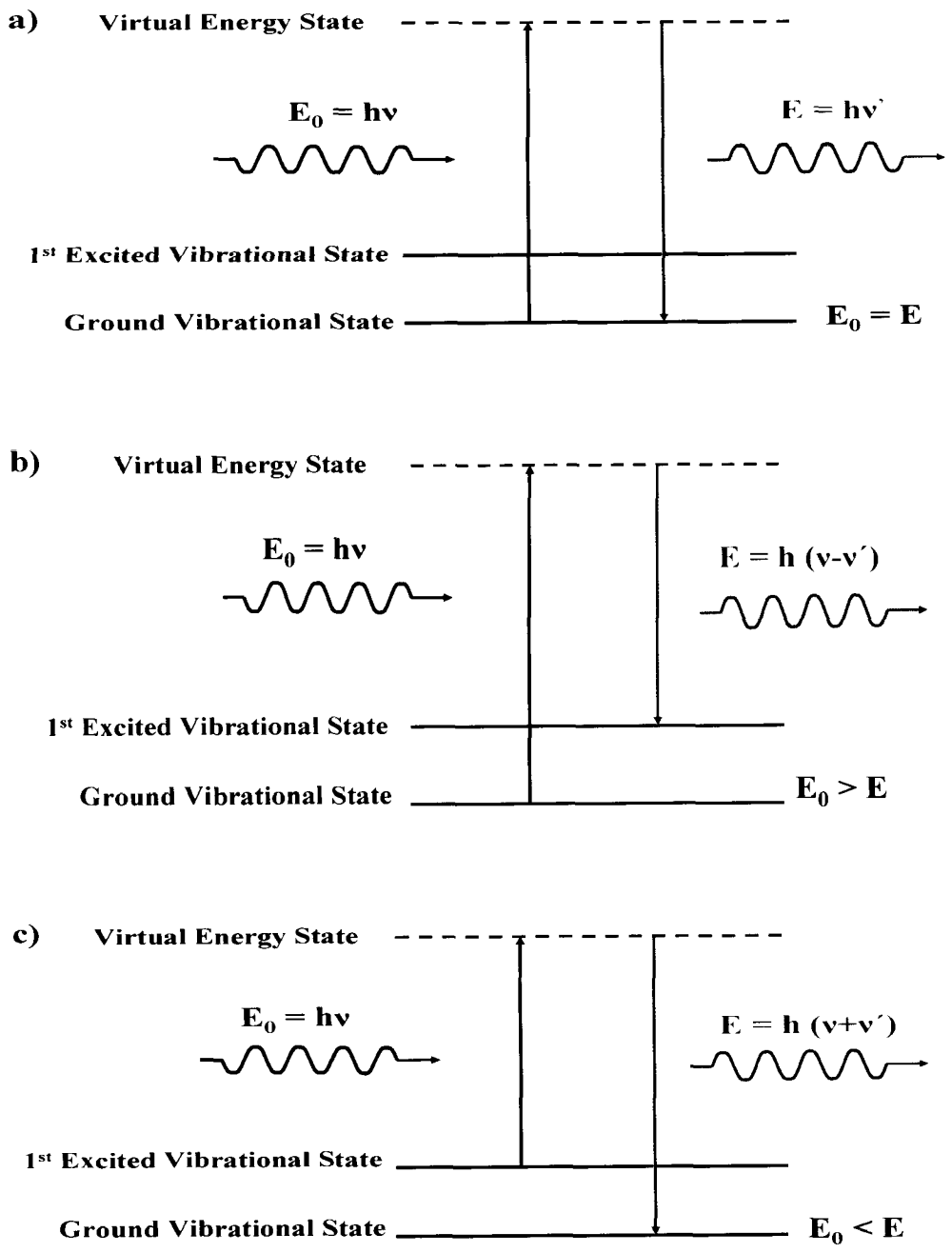

Figure 3-10 : Illustration showing (a) Raleigh scattering, (b) Stokes (Raman) scattering, and (c) Anti-stokes scattering.

Chapter 4

4 EXPERIMENTAL TECHNIQUES

4.1 Experimental Conditions

4.1.1 Electrochemical Cell

A standard three-electrode electrochemical cell was used in this study (Figure 4-1). The electrode components were a carbon steel working electrode (WE), whose potential was controlled against a saturated calomel reference electrode, (RE) (SCE, 0.241 V vs. SHE), and a platinum wire mesh counter electrode (CE), through which current flows at the same rate as through the working electrode (overall CE area = 18 cm2). The CE was made by spot welding a 1mm diameter platinum wire to a 4 cm x 4 cm platinum sheet (99.95% purity). Platinum mesh was chosen for the CE because of its high activity, negligible by-product production and large surface area compared to the WE. As shown in Figure 4-1 the RE, and CE were placed in separate compartments, isolated from the main cell containing the WE via porous frits. Through the open tip of the Luggin capillary, the RE senses the solution potential near the WE, minimizing any IR drop associated with the passage of current in the electrolyte. Additionally, a gas dispersion tube was fitted into the cell to allow purging with Ar gas, and a gas bubbler was used to ensure the cell remains air tight.

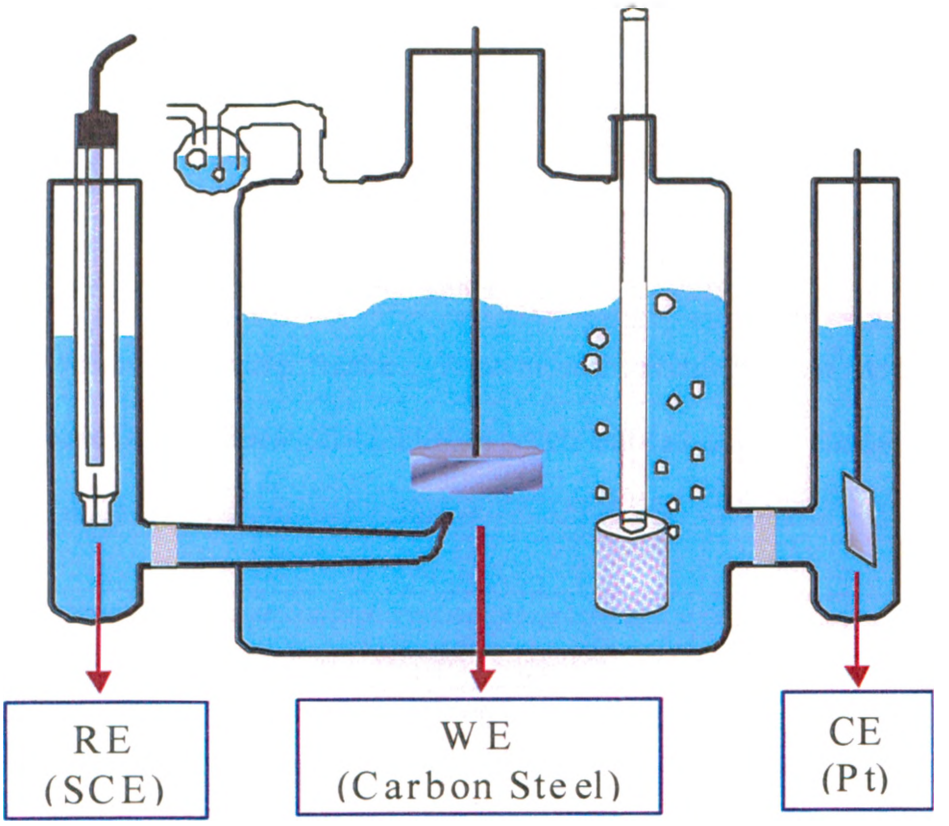

Figure 4-1 : The three-electrode electrochemical cell used for all experiments

4.1.2 Electrode Preparation

The WE was fabricated from cylindrical discs cut from an A516Gr70 carbon steel rod, with a composition (in wt%) of C 0.28, Mn 1.3, P 0.035, S 0.035, Si 0.45, with the balance being Fe. The carbon steel disc was placed in a polytetrafluoroethylene (PTFE) tube using epoxy resin, threaded onto a steel rod in the PTFE holder, and sealed with Teflon tape to prevent exposure of the back of the electrode to the electrolyte.

Through this preparation, the exposed area of the carbon steel electrode was limited to the flat front face having a surface area of 0.385 cm^2. The carbon steel electrodes were wet polished using 800, and 1000 grit silicon carbide papers and finally with a 1 μm polycrystalline diamond suspension. They were then washed with Millipore water (18.2 MΩ.cm resistivity), and ultrasonically cleaned in an acetone/methanol mixture for five minutes to remove polishing residue. Prior to each electrochemical experiment, the working electrode was rinsed with Millipore water, and cathodically cleaned at – 1.1 V for 5 min to remove any air-formed oxides.

4.1.3 Electrolyte

Experiments were conducted at room temperature in a 0.01 M sodium borate solution with the pH adjusted to 10.6. The electrolyte solution was made up with reagent-grade $Na_2B_4O_7 \cdot 10H_2O$ (Caledon Laboratories Ltd., 99.0% assay) and de-ionized water (Milli-Q Millipore), and the pH adjusted with small amounts of 2 M sodium hydroxide (NaOH, Caledon Laboratories Ltd., 97.0% assay). The pH of the electrolyte solution was measured using an Accumet® Basic AB15 pH meter with a standard size glass electrode prior to performing each experiment. When needed (Sodium) iodide, bromide, and chloride solutions in the concentration range 10^{-4} to 10^{-3} M were also prepared with reagent-grade chemicals (Caledon Laboratories Ltd, all 99.0% assay).

4.2 Electrochemical Methods

Two types of experiments were conducted; cyclic voltammetry and potentiostatic oxidation. All experiments began with a freshly polished carbon steel WE, placed in the pH-adjusted 0.01 M borate solution containing the desired concentration of a specific halide. The solutions were prepurged with Ar for at least one hour to remove dissolved oxygen from the solution. The WE was then cathodically cleaned at -1.1 V (versus SCE) for 300 s to remove air-formed oxide films. Electrochemical measurements were made using an 8-channel Solarton model 1480 potentiostat. Corrware^{TM} and Corrview^{TM} software (supplied by Scribner and Associates) were used to control experiments and to analyze data.

4.2.1 Cyclic Voltammetry

Cyclic voltammetry was conducted by scanning from the cathodic cleaning potential of -1.1 V to 0.4 V (vs. SCE) and back at a scan rate of 5 $mV.s^{-1}$ (
Figure 4-2). Cyclic voltammetry was used to determine passive film breakdown potentials on the carbon steel surface, and to provide a basis for the choice of potential in potentiostatic experiments. The concentration of the halides was 10^{-3} M in all voltammetric experiments.

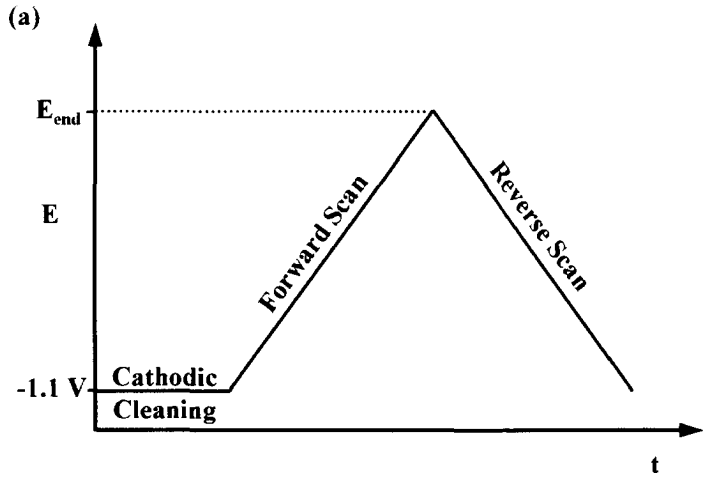

Figure 4-2 :Schematic of the potential-time profile used in cyclic voltammetry experiments

4.2.2 Potentiostatic Experiments

Potentiostatic experiments were conducted to determine the influence of oxide formation at lower potentials on subsequent oxide growth and conversion processes at higher potentials:

- In the first set of experiments, the carbon steel electrode was pre-oxidized by scanning the potential from E = -0.5 V to E = -0.3 V at a scan rate of 0.05 $mV.s^{-1}$,
- In the second set of the experiments, the surface was pre-oxidized by applying a constant potential at – 0.6 V for one day.

After one of these pre-oxidation steps, the potential was increased in a step-wise manner by 20 mV increments up to + 0.4 V. The potential was held for 40 min after each increment, during which period the current was measured for the first 20 min and an EIS

measurement performed over the second 20 min period. The procedure is illustrated in Figure 4-3. The presence of halide during the preoxidation stage could have influenced film growth, thereby making the film more susceptible to breakdown at higher potentials. To investigate whether this was the case, film growth was also conducted in the absence of halide which was subsequently added after the potential was raised to a desired value.

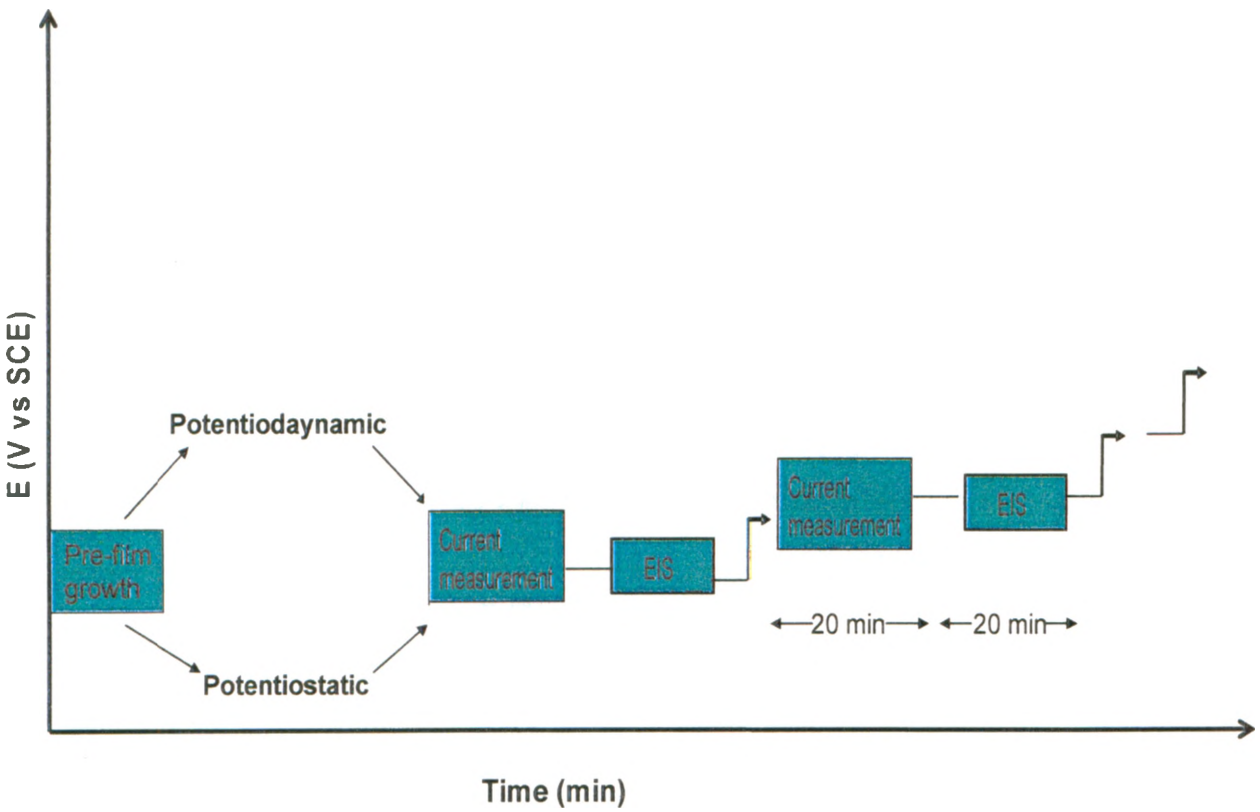

Figure 4-3 :Schematic of the potential-time profile used in potentiostatic/EIS experiments

4.2.3 Surface Analyses of Films Following Potential Step Experiments

Following film growth, a variety of methods were used to characterize the electrode surfaces. In some potentiostatic experiments the electrode was removed when the potential reached a desired value so that the electrode surface morphology and composition could be characterized. To prepare samples for surface analysis, electrodes were removed from the cell, washed with deionized water, dried with Ar gas, and then transferred into a glass vial inside a glove box to avoid complication due to air exposure.

4.2.4 Electrochemical Impedance Spectroscopy (EIS) Measurements

All EIS measurements were made using a Solartron 1252 frequency response analyzer coupled to a Solartron 1480 multistat. EIS was performed by applying a ± 10 mV (root mean square) AC sinusoidal potential waveform at the applied DC potential and recording the spectrum over the frequency range 10^4 to 10^{-2} Hz. Zplot™ / Zview™ software was used to acquire and analyze the data (supplied by Scribner and Associates). A small number of measurements were conducted from low frequency to high frequency to confirm that steady-state was maintained throughout the measurement.

4.3 Surface Analyses

4.3.1 Raman Spectroscopy

Ex-situ Raman spectroscopy was performed using one of two instruments. The first instrument was a Renishaw model 2000 Raman Spectrometer with a CCD detector running GRAMS/386 Version 3.03 Level II software, (Galactic Industrial Corporation) with a 633 nm line from a Melles Griot 35 mW HeNe laser. The laser was focused on the specimen using an Olympus microscope with a 50 x objective lens. The second instrument was a Confocal Raman microscope (Alpha SNOW, WITec) equipped with a YAG linearly polarized laser (Verdi 5, Coherent Inc., Santa Barbara, CA) with a 532 nm wavelength which was used to focus the laser beam onto the specimen and to collect Raman signals. Both instruments were used to analyze the deposits on electrochemically-treated carbon steel electrodes. *In-situ* Raman spectroscopy was performed using the Renishaw model 2000 on specimens anodically oxidized in borate buffer solution containing Br^- to investigate the oxide film present before and after film breakdown leading to pitting.

4.3.2 Scanning Electron Microscopy/Energy Dispersive X-ray (SEM/EDX)

Scanning Electron Microscopy (SEM) in combination with Energy Dispersive X-ray analysis was performed using a Leo 440 to examine the porosity, morphology and composition of corrosion product deposits. Samples were examined without applying a

coating. A copper strip was attached to the edge of the electrode to eliminate charging effects.

4.3.3 X-ray Photoelectron Spectroscopy (XPS)

XPS analyses were carried out with a Kratos Axis Nova spectrometer, using Al K_α- monochromatic radiation, operating at 150 W with a vacuum of 1×10^{-8} Pa. A micro-channel plate and phosphor detection system are incorporated into the system to provide parallel imaging capability with high spatial resolution and high sensitivity. The instrument probes the surface of the sample to a depth of 5-7 nanometers, and has detection limits ranging from 0.1 to 0.5 atomic percent depending on the element. The Kratos charge neutralizer system was used on specimens as necessary. Survey scans were carried out on an analysis area of 300 x 700 microns and a pass energy of 160 eV. High resolution analyses were carried out on an analysis area of 300 x 700 microns with a pass energy of 20 eV. The Fe 2p (at 720.75 eV ±19.1 eV), O1s (at 533.95 eV ± 9.1 eV), and C 1s (at 284 eV ± 0.5 eV) region of the spectrum were recorded. The spectra were charge-corrected, when required, by reference to the main line for the carbon 1s spectrum (adventitious carbon) set to 284.8 eV. Spectra were analysed using CasaXPS software (version 2.2.107).

Chapter 5

5 RESULTS AND DISCUSSION

5.1 Cyclic Voltammetry (CV)

Figure 5-1 shows the effect of halide anions on CVs recorded on carbon steel during (a) the first and (b) the second scan cycle. The current behaviour observed during the forward scan of the first cycle in halide solutions is essentially identical to that obtained in halide-free solution, up to a potential of ~ 0.1 V. Above this value, the anodic currents in halide solutions deviate significantly from those in borate solutions. This dramatic increase in current indicates the onset of pitting of the steel following a breach in the passive surface-oxide film. The potential at which the anodic current starts deviating from that in halide-free solution is, hereafter, referred to as the film-breakdown potential, E_B, consistent with literature terminology [73]. The film breakdown potential varied from one experiment to another even under the same condition, but was observed to be always above 0.0 V (vs. SCE).

The subsequent scan cycles observed in halide solutions were generally the same as those observed in halide-free solutions, except for the Cl^- case. For a solution containing Cl^-, film breakdown was still observed on the second scan, but no longer observed, on the third or higher scan cycle.

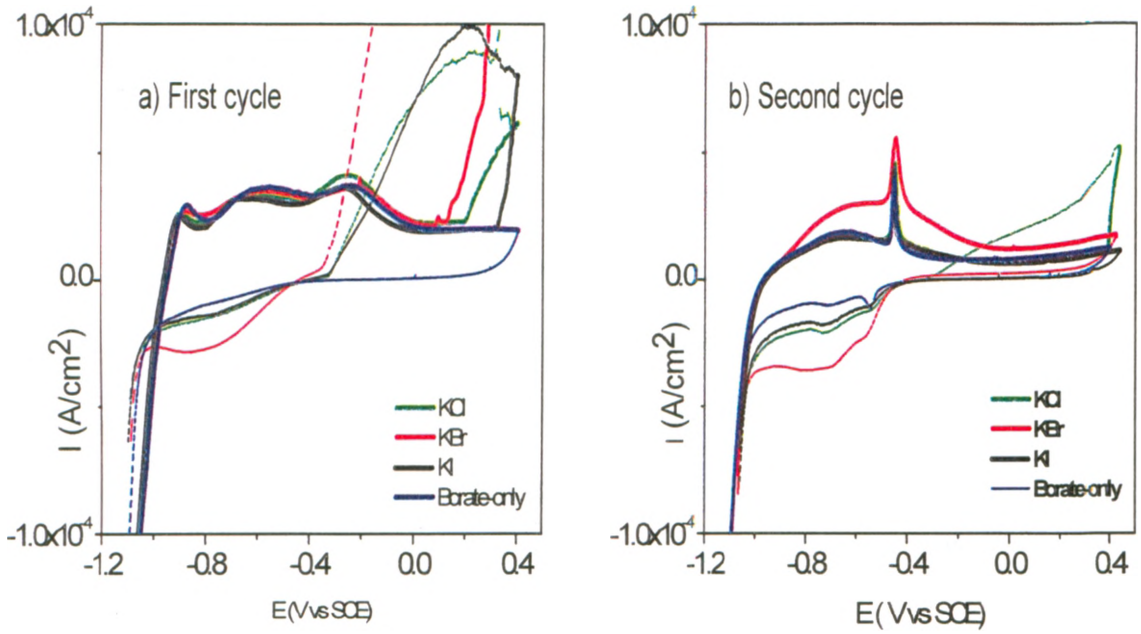

Figure 5-1 :Cyclic voltammograms recorded on carbon steel in 0.01 M borate buffer solutions containing 10^{-3} M halides: (a) the first cycle and (b) the second cycle. The CV obtained in a borate solution free of halide is also shown for comparison. Each scan was performed from -1.1 V to an anodic limit of 0.4 V and back to -1.1 V at 5 mV. s^{-1}. The solid lines show the forward scans, and the dashed lines the reverse scans.

The magnitude of the pitting current (the anodic current following film breakdown) also varied from one experiment to another, and showed no systematic dependence on the type of halide. This is expected, since the pitting corrosion rate depends on highly localized conditions within pits, not on bulk solution composition.

On the reverse scan, as the potential decreases, the current remains anodic, and, in cases when pitting initiated, increased considerably before decreasing and eventually

switching to a cathodic value. Such anodic hysteresis loops are commonly observed in voltammetric scans when pitting occurs. The potential at which the current becomes zero, referred to as the zero-current potential, $E_{i=0}$ in this study was similar for all three halide solutions as well as for halide-free solutions.. The zero-current potential, $E_{i=0}$, was equal to -0.4 ± 0.05 V and did not change with the scan cycle number. Note that $E_{i=0}$ differs from the re-passivation potential commonly used in pitting corrosion literature, where it is defined as the potential at which the current on the reverse scan becomes equal to the current on the forward scan. The re-passivation potential is very sensitive to the scan rate and the initial condition of the film. The magnitude of the cathodic current observed below $E_{i=0}$ was higher in halide solutions than in halide-free solutions. The relative increase in the cathodic current did not show any systematic dependence on type of halide.

When the halide concentration was below 10^{-3} M, no film breakdown was observed during CV scans at the rate of 5 mV/s used in this study. This is consistent with the study by Valcarce and coworkers [86] which showed that when the chloride concentration is lower than $[OH^-]$, i.e., $[Cl^-] / [OH^-] < 0.125$, chloride has no significant effect on the CV behaviour of carbon steel.

Previous studies [84] on oxide film formation and conversion on carbon steel have identified three oxidation potential regions for carbon steel at pH 10.6:

- Region I (E (V vs SCE) < – 0.6 V): The oxidation state of the oxide formed is limited to that of conductive magnetite (Fe_3O_4) or, a magnetite-like, phase.

- Region 2 (- 0.5 V < E (V vs SCE) < - 0.2 V): The oxide varies in composition with thickness, from a magnetite-like phase close to the metal/oxide interface to a more maghemite-like (γ-Fe_2O_3) phase close to the oxide/solution interface.

Region 3 (E (V vs SCE) > 0.0 V): Further oxidation of the inner magnetite to lepidocrocite (γ-FeOOH) becomes thermodynamically possible. This conversion leads to a significant volume change in the oxide which can expose the underlying layer to further oxidation.

5.2 Current Behaviour Under a Series of Potentiostatic Conditions

The primary purpose of performing the CV scans was to obtain a preliminary determination of the range of the film breakdown potential for carbon steel exposed to halide solutions. However, this technique has significant limitations since surface oxide (and/or halide) formation and conversion are known to be affected by scan rate, and the film formed at a faster scan rate is more likely to contain a high level of microscopic defects [87]. To avoid this problem experiments were performed under a series of potentiostatic conditions, where the potential was increased stepwise in 20 mV increments and applied for 40 min, sufficient time for the system to reach steady state and to allow EIS measurements.

Prior to the potentiostatic experiment, prefilm were grown either potentiostatically at -0.6 V or potentiodynamically at -0.5 V to -0.3 V.

During anodic film growth, there are two possible mechanisms by which halides can induce pitting corrosion on carbon steel:

1) Halides could be incorporated in to the metal-oxide matrix during film formation, resulting in a defective film susceptible to film breakdown and pit propagation, at a sufficiently high potential.

2) Halides are not involved in the oxide-film formation, but take advantage of film restructuring, or changes in the oxide phase or composition, to induce breakdown of the passive oxide layer and expose the base metal.

To differentiate between these possibilities, three sets of experiments were performed as described in section 4.2.2, and illustrated in Figure 4-3. In the first set, halide was added at the beginning of the experiment; and in the second set, halide was added after the potential had reached a value > 0.0 V, i.e., a value in the potential region of film breakdown observed in the CV experiment. In the third set to investigate the influence of the thickness and composition of the film initially present , an oxide was pre-grown at – 0.6 V for one day; at this potential a magnetite film would be expected.

5.2.1 Presence of Halide from the Beginning of the Experiment

Figure 5-2 and Figure 5-3 show the current observed as a function of potential (Figures a, c, and e) and as a function of time (Figures b, d, and f) in a solution containing 10^{-3} M of halide from the beginning of the experiment.

Figure **5-2** illustrates the cases which resulted in pitting whereas Figure 5-3 shows the cases which resulted in no pitting. In these figures the gaps in the current-time plots correspond to the intervals during which electrochemical impedance spectroscopy measurements were made.

Two main differences were observed in the current behaviour between the pitting and non-pitting cases. One difference is the potential, $E_{i=0}$, at which the current switched to cathodic on the reverse potentiodynamic scan from 0.4 V to – 0.5 V. This feature can be seen in Figure 5-2 (a, c, and e) and Figure 5-3 (a, c, and e) as the continuous lines overlying the current-potential plots. When pitting occurred, $E_{i=0}$ was observed to be -0.40 ± 0.05 V, irrespective of the type and concentration of halide, which is the same value observed in the CV experiment Figure 5-1. When no pitting occurred, $E_{i=0}$ = 0.2 ± 0.05 V, again irrespective of the type and concentration of halide, and in the potential range where film breakdown was observed on the forward scan in experiments containing halides.

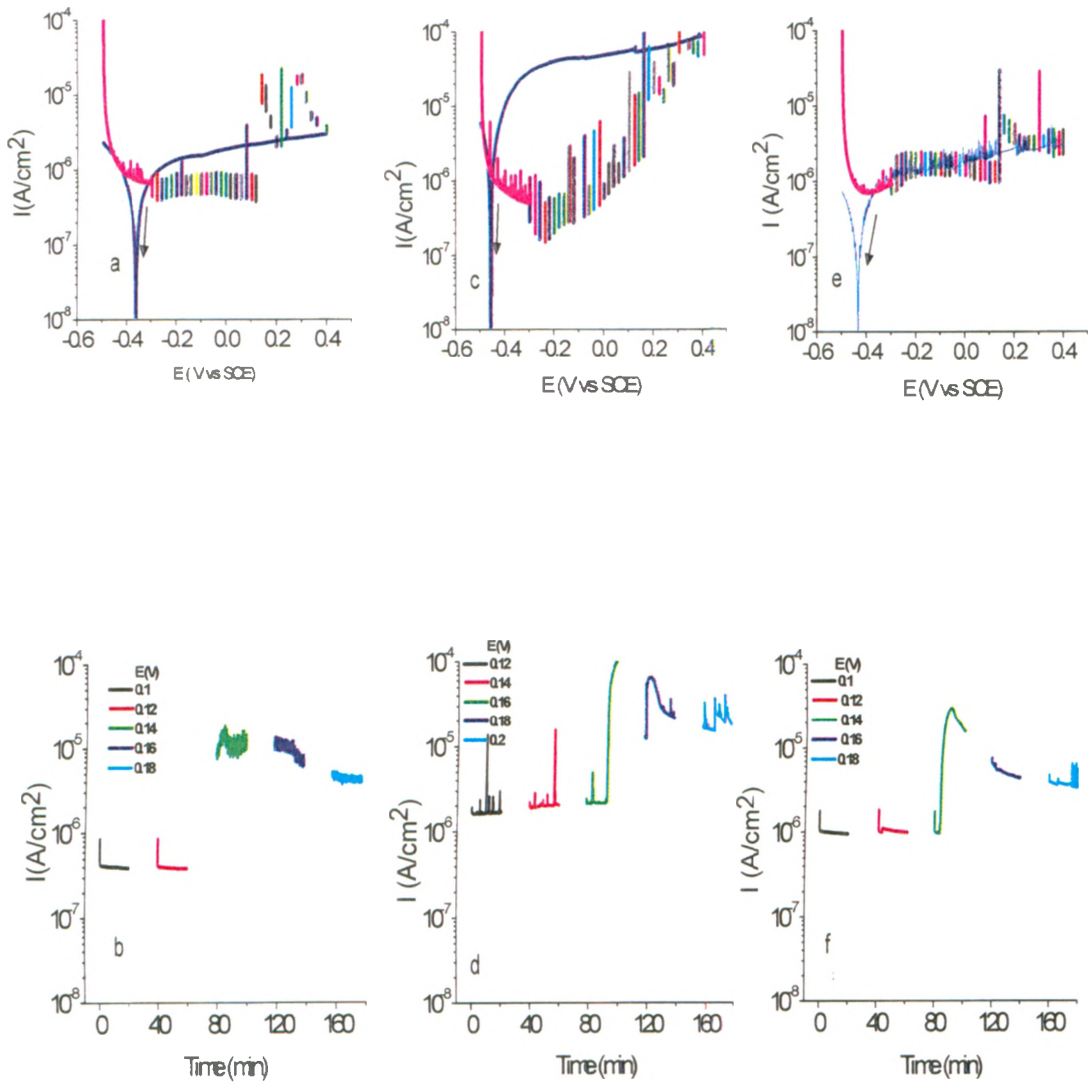

Figure 5-2 : Currents measured during potentiostatic film growth using the potential profile described in Figure 4-3. Halides were present from the onset of the experiments at a concentration of 10^{-3} M in borate solution at pH = 10.6; a, b) KCl; c, d) KBr; and e, f) KI. In these experiments pitting eventually occurred.

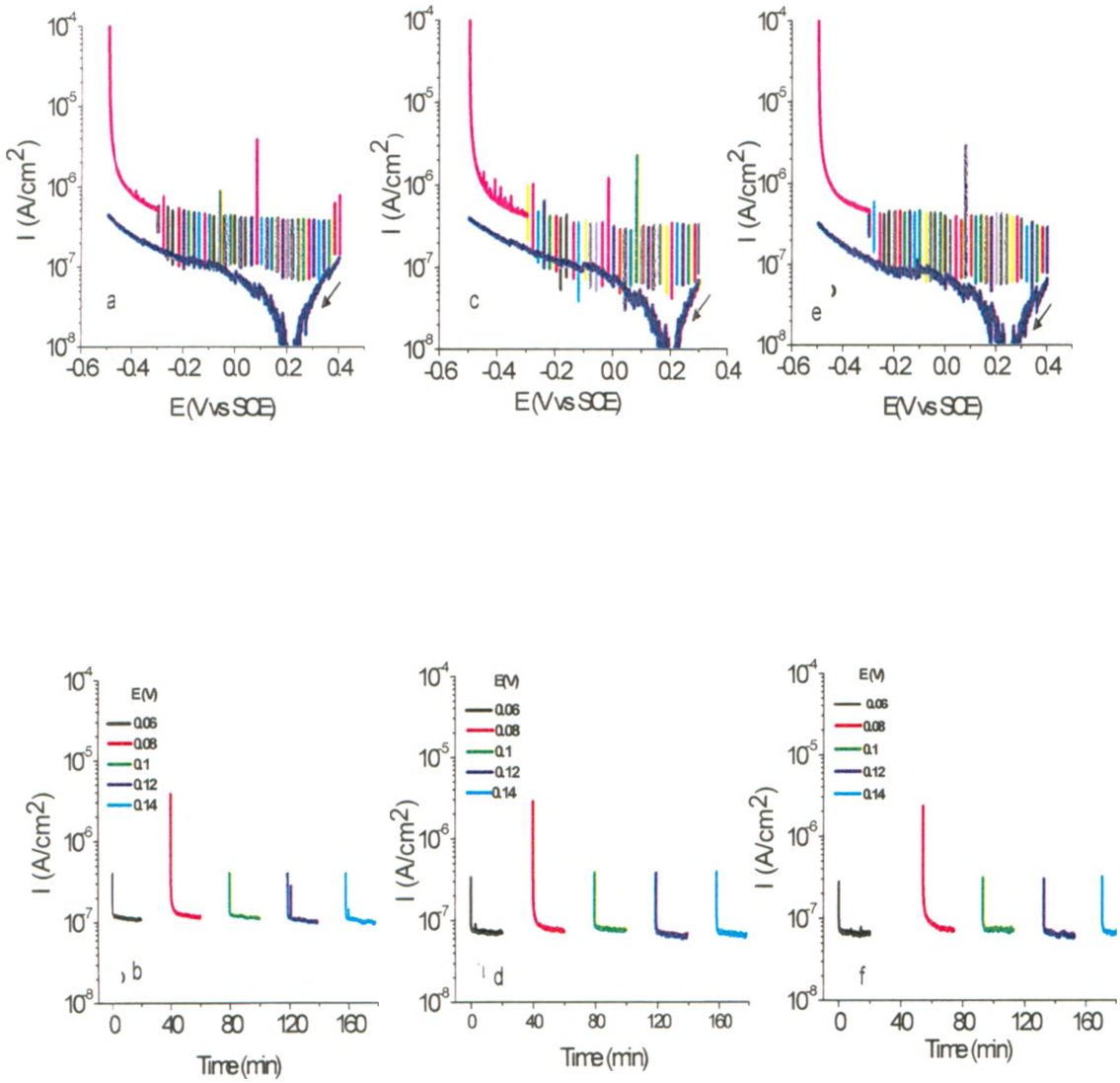

Figure 5-3 :Currents measured during potentiostatic film growth using the potential profile described in Figure 4-3. The experimental conditions were the same as those used in the experiments shown in Figure 5-2, but did not result in pitting corrosion; a, b) KBr; c, d) borate-only case; and e, f) KI

The observation that $E_{i=0}$ = - 0.40 ± 0.05 V shows that, under active pitting conditions, the passive film, formed at the sharp peak in the voltammogram, Figure 5-1(b), is destabilized locally on the electrode surface. The more positive potential value observed when pitting does not occur indicates passivity is maintained.

After each potential increase (in 20 mV increments), the current initially jumped to a slightly higher value before rapidly decreasing to the initial value. However, when pitting occurred, the current jumped to a higher level and remained there, or decreased at a much slower rate. The potential at which the current begins to increase indicating the onset of pitting is referred to as E_B, the breakdown potential, consistent with the terminology used in CV experiments (Section 4.2.1). As in the CV experiment, the measured E_B values varied from one experiment to another, and did not appear to have any systematic dependence on the type of halide, Figure 5-4. Of note, film breakdown always occurred at potentials > 0.0 V in the CV experiments, an observation consistent with the histogram of film breakdown potentials observed in potentiostatic experiments, as shown in Figure 5-4. The lowest breakdown potential recorded was 0.08 V, irrespective of the rate and the manner of potential increase. The breakdown potential was observed to always be in potential Region 3 defined in section 5.1[84]. In Region 3 (E > 0.0 V) oxidation of magnetite to lepidocrocite (γ-FeOOH) could lead to a significant volume change in the oxide phase and exposure of the underlying layer to further oxidation.

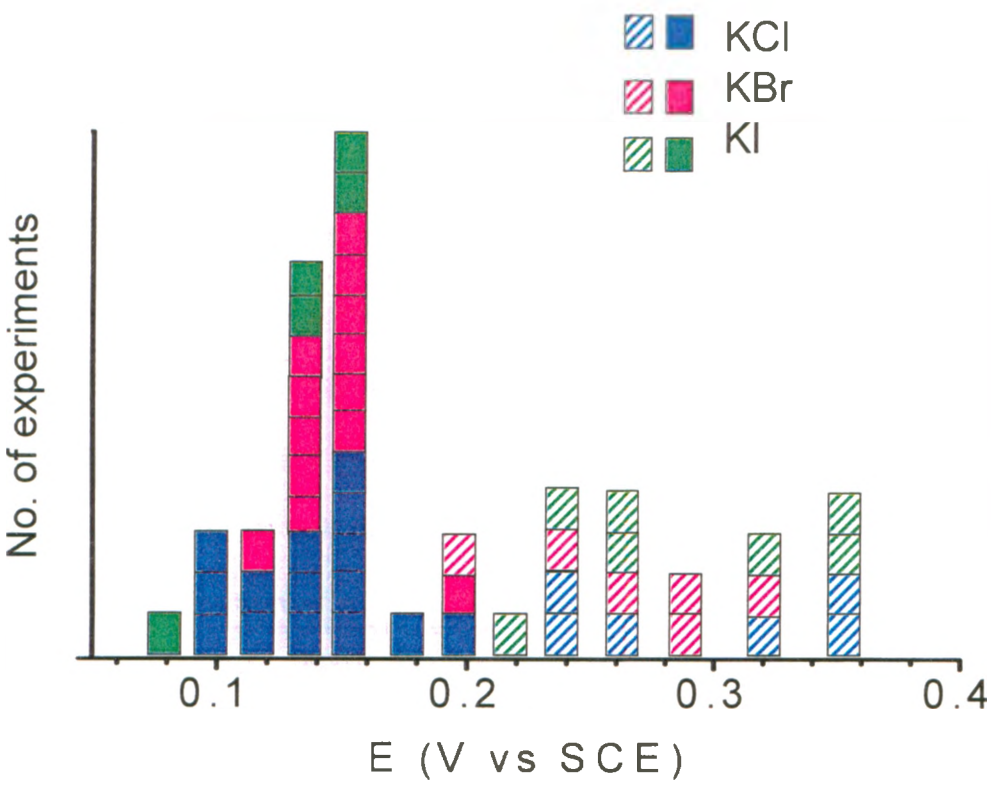

Figure 5-4 :Histogram of breakdown potentials, E_B, in different halide solutions. The solid blocks are those observed for thin films and the shaded blocks are those for thick films.

In both the CV and the potentiostatic experiments, the current level following film breakdown varied considerably from one experiment to another, even under the same experimental conditions. This suggests that once film breakdown occurred and pitting initiated, the rate of propagation of pits depended strongly on the local pH within individual pits and the mode of propagation of the pit. Interestingly, during experiments that resulted in no pitting, a higher surge of current was often observed upon increasing the potential to a value above 0.08 V, the minimum threshold above which pitting

occurred, see Figure 5-2 (a, c, and e). However, the current quickly decreased to the initial value, as was observed at other potentials. This surge may suggest changes in the film occurred at potential of 0.08 V. However, any breach in the film was quickly repaired in the absence of halides, preventing the propagation of pitting. When no pitting occurred, the current behaviour observed for step-wise increases in potential above 0.08 V in halide solutions was very similar to those observed for halide-free solutions, indicating that halides are not required to induce the film transition. This phenomenon is explored further by cycling back and forth around this potential (E = 0.08 V). Each time a jump in current was observed at E = 0.08 V. But when the potential was raised by 20 mV to E = 0.1 V and then back to E = 0.06 V, the transit behaviour was no longer observed.

5.2.2 Addition of Halide at Later Stages of Oxide Growth and Conversion

To determine whether the presence of halide influences oxide film growth/conversion leading to eventual film breakdown, oxide-films were grown in halide-free solutions using the same potential profile used in the first set of the experiments (Figure 4-3), section 4.2.2. When the potential reached a desired value, 10^{-3} M halide was added, and the potential was maintained at this value over a long period (5 to 20 h). This long period was used to ensure a similar exposure time to the halide solution in the two sets of experiments in the absence and presence of halide from the beginning of each experiment.

The addition of halide at potentials below 0.1 V *vs.* SCE did not lead to pitting, even for a subsequent exposure period of 20 h. However, the addition of halide at E >

0.14 V, a potential ~ 40 mV higher than the minimum breakdown potential, often lead to pitting Figure 5-5 shows a typical log | i| – t plot, in which 10^{-3} M Br^- was added to the solution at a potential of 0.14 V, after which, the potential was increased to 0.16 V and maintained at this value for 5 h. In this particular experiment, two current excursions were observed, the first at ~ 1 h and the second at ~ 3 h after the Br^- addition. In the first event, the initial film breakdown did not result in pitting, and the current was quickly restored to the initial value. For the second event, the current increase resulted in pitting, as indicated by the continuing high current (Figure 5-5).

These results indicate that the growth of a defective film in a halide-containing solution is not a prerequisite for film breakdown and the onset of pitting. This supports the second mechanism for halide- induced pitting discussed in Section 5.2.1. The key requirement is that the potential be in Region 3, where oxidation of magnetite in the inner region of the film to lepidocrocite (γ-FeOOH) results in a significant volume change in the film. The ensuing stresses then lead to breakdown of the passive oxide layer and exposure of the underlying active oxide or base metal. Once this happens, halides take advantage of the film fractures, preventing their repair, thereby allowing pits to propagate.

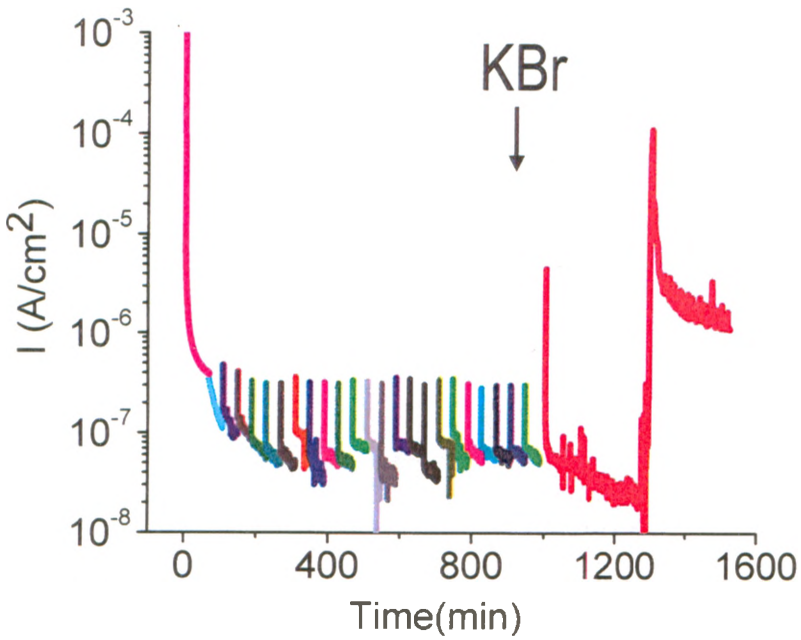

Figure 5-5 : Current-time behaviour observed during potentiostatic film growth using the potential profile in Figure 4-3; 10^{-3} M KBr was added to the borate solution when E reached 0.14 V. Following the Br- addition, the potential was increased to 0.16 V and maintained at this value for 5h.

5.2.3 Effect of Film Growth Time on Breakdown Potential

The effect of film growth time on pit initiation was explored by varying the extent of film growth in potential Region 1 (E < - 0.6 V), where oxide growth to yield a conducting magnetite phase occurs, as will be discussed in more detail in section 5.3. The results described in sections 5.2.1 and 5.2.2 were obtained after initial film growth under potentiodynamic conditions by scanning the potential from – 0.5 V to – 0.3 V in

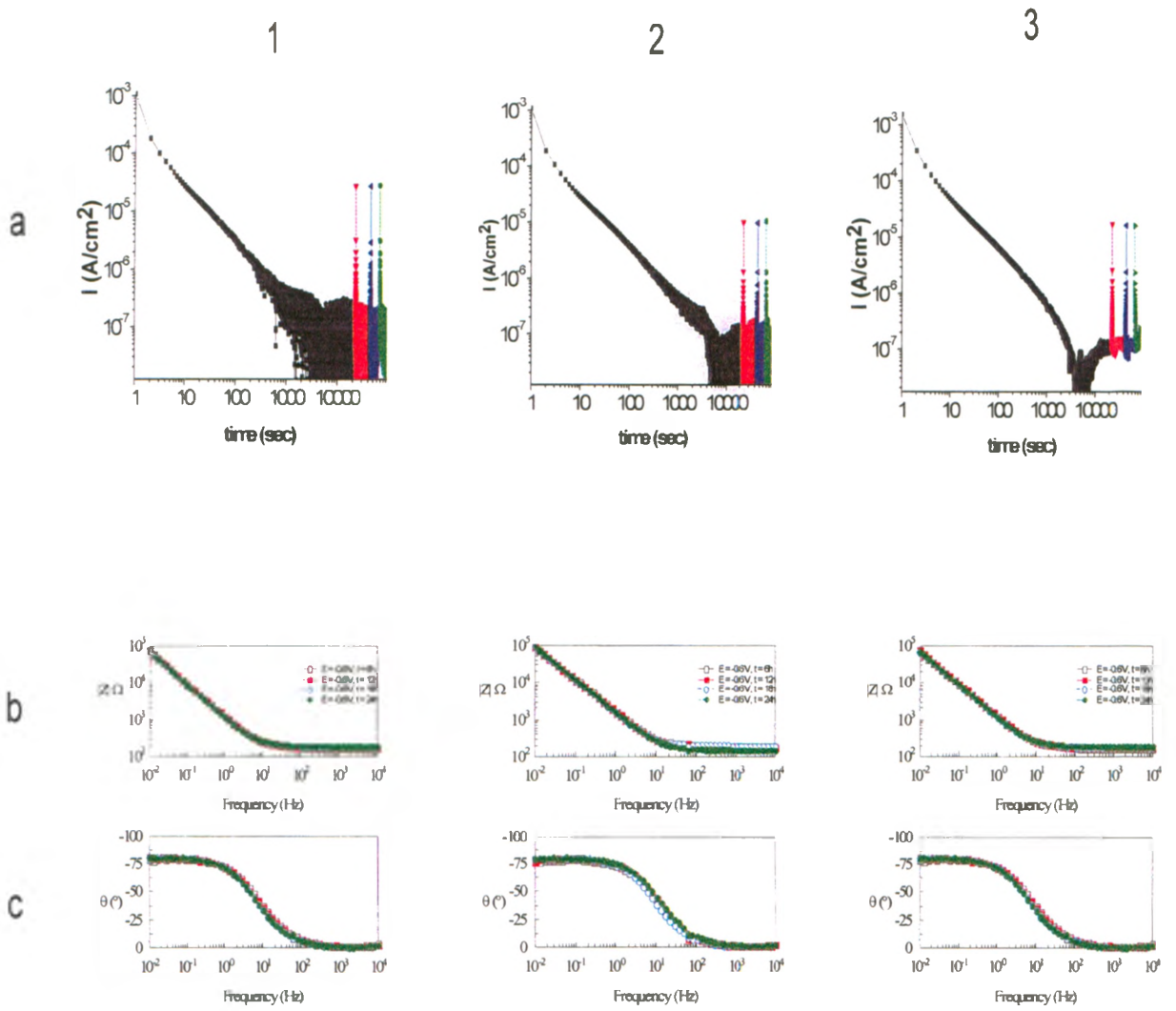

Figure 5-8 :a) Currents measured during potentiostatic film growth using the potential profile illustrated in Figure 4-3, after pre-growth at E = -0.6 V for one day in the 10^{-3} M borate solution at pH = 10.6. a1) Borate-only case, a2) KCl, and a3) KBr. (b) EIS response plotted as the log |Z| vs log Frequency at E = – 0.6 V: b1) borate-only case, b2) KCl and b3) KBr. (c) EIS response plotted as the phase angle (θ) vs log Frequency at E = - 0.6 V: c1) borate-only case, c2) KCl, and c3)KBr

Previous studies (84) attributed the observed current behaviour after the first 10 s to the solid-state growth of a magnetite-like (Fe_3O_4) phase. Magnetite is electronically conducting (with a band gap of 0.2 eV, [88]), and, thus, can support water reduction at this potential, which accounts for the steady-state cathodic current at longer times. The EIS, taken at every 6 h after steady state had been reached, showed no change with time, and were the same for all three solutions.

The impedance response can be represented by a single time constant equivalent circuit, and since magnetite is conducting this response will be primarily across the Fe_3O_4/solution interface. The similar current and EIS behaviour observed in both halide-free and halide-containing solutions is consistent with the interpretation that halide is not involved in the oxide formation at this potential. This observation is also consistent with the fact that $Fe(OH)_2$ is thermodynamically more stable than FeX_2 at this potential and pH 10.6 [88]

5.3.2 Film Growth During Step-wise Potential Increases

Following film growth at – 0.6 V for 1 day, the potential was increased in 20 mV increments (section 3.2.2.). At each potential, the current was measured taken for 20 min, followed by an EIS measurement which took another 20 min. The current as a function of time and the EIS observed at each potential are shown in Figure 5-9 for -0.58 V < E < -0.46 V, Figure 5-10 for -0.46 V < E < 0.0 V, and Figure 5-11 for 0.0 V < E < 0.4 V.

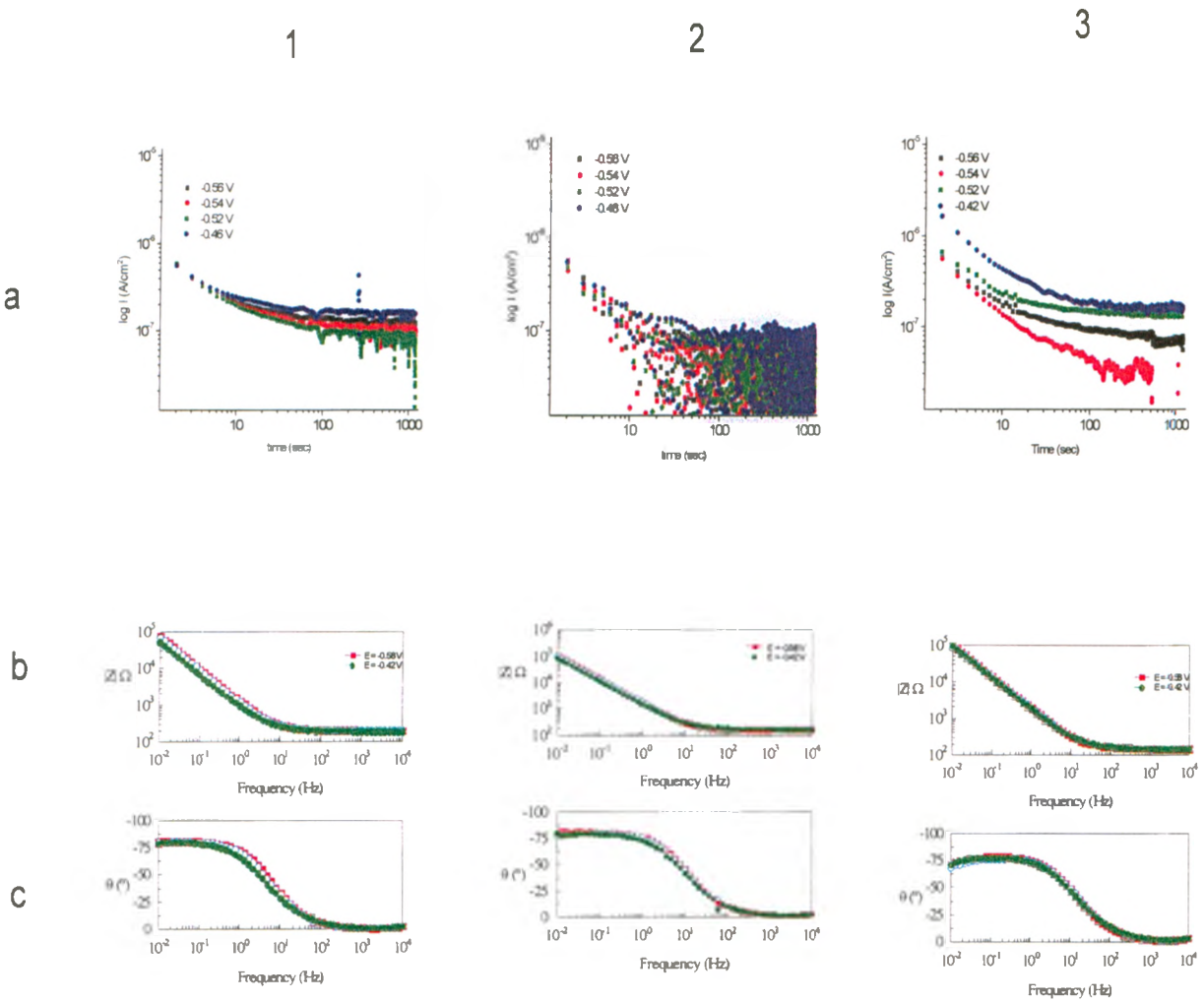

Figure 5-9 :a) Current measured during potentiostatic film growth, using the potential profile illustrated in Figure 4-3, after pre-growth of an oxide at E = -0.6 V for one day in the 10^{-3} M borate solution at pH = 10.6. a1) Borate-only case; a2) KCl; and a3) KBr. (b) EIS response plotted as the log |Z| vs log Frequency at - 0.58 V< E < – 0.46 V; b1) borate-only case; b2) KCl; and b3) KBr. (c) EIS response plotted as the phase angle (θ) vs log Frequency at - 0.58 V< E < – 0.46 V; c1) borate-only case; c2) KCl; and c3)KBr

The potential range, -0.58 V < E < -0.46 V (Figure 5-9) is the transition region between Regions 1 and 2, described in Section 5.1 [84]. In this potential region, continuous growth of magnetite (Fe_3O_4) and slow dissolution of Fe^{2+} and Fe^{3+} are expected. The current behaviour observed in this potential range was the same for halide-free and halide-containing solutions; the current increased with an increase in potential, and then decreased with time for ~ 10 s before reaching a steady-state value. The steady-state current increased slightly with an increase in potential in all cases. The EIS taken in this potential range also show no significant changes, as expected for the growth of a near-conducting magnetite-like oxide.

In Region 2 (- 0.5 V < E < 0 V), no significant increase in current occurred on increasing the potential, Figure 5-10. The current remained nearly constant with time, and the steady-state current was nearly independent of potential, exhibiting only a very small increase with increasing in potential. Despite the constant current behaviour, noticeable changes in the EIS occurred: the absolute impedance at the lowest frequency increased by an order or magnitude, and the maximum phase angle shifted to a higher frequency while decreasing at lower frequencies as the potential was increased from – 0.5 V to 0 V.

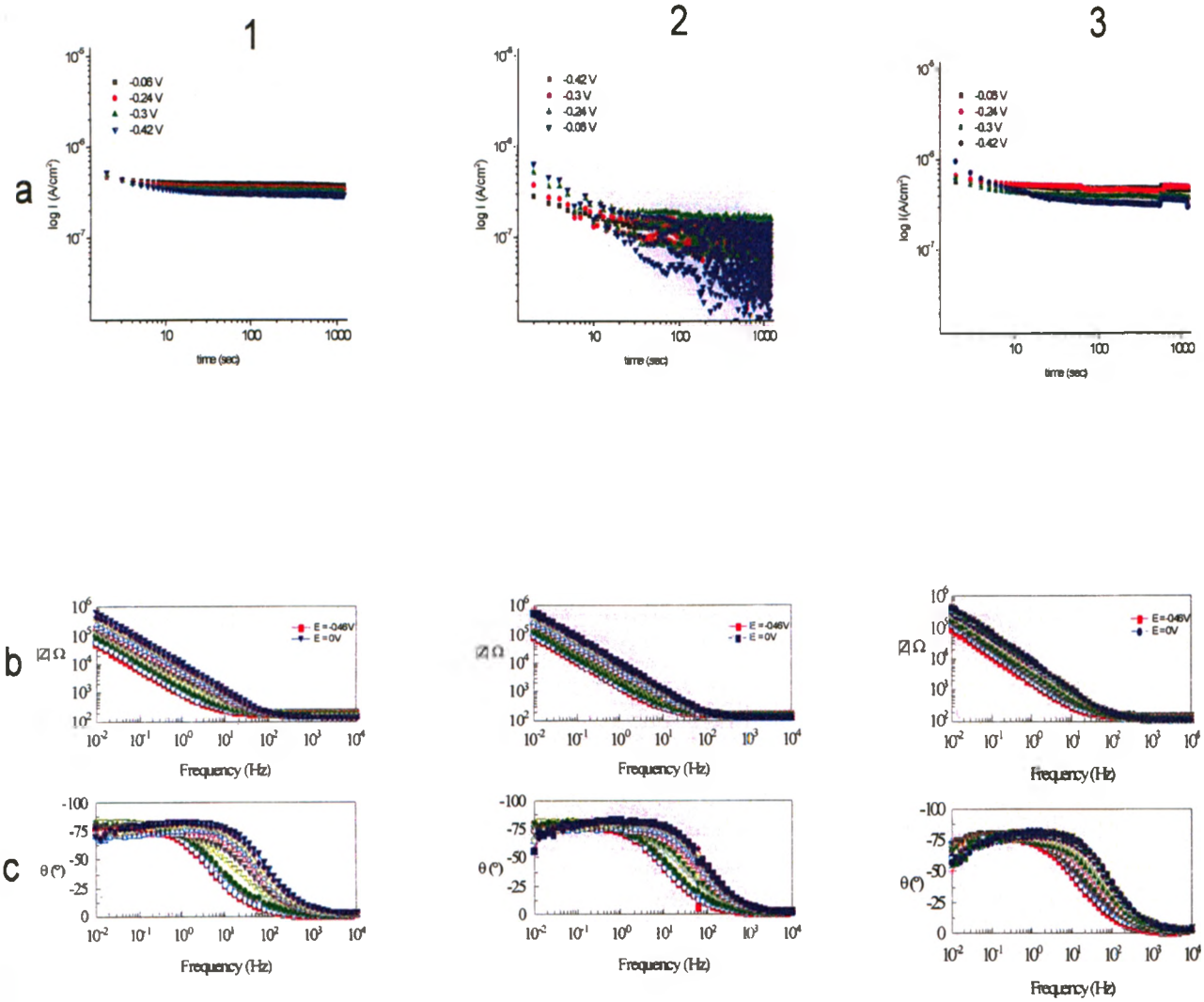

Figure 5-10 :a) Current measured during potentiostatic film growth, using the potential profile illustrated in Figure 4-3, after pre-growth of an oxide at E = -0.6 V for one day in the 10^{-3} M borate solution at pH = 10.6. a1) Borate-only case; a2) KCl; and a3) KBr. (b) EIS response plotted as the log |Z| vs log Frequency at - 0.46 V< E < 0 V; b1) borate-only case; b2) KCl; and b3) KBr. (c) EIS response plotted as the phase angle (θ) vs log Frequency at - 0.5 V< E < 0 V; c1) borate-only case; c2) KCl; and c3) KBr

These observations are consistent with the solid-state conversion of Fe_3O_4 to a more maghemite-like (γ-Fe_2O_3) phase at the oxide-solution interface in Region 2, [84] as will be discussed further in section 6. Both magnetite and maghemite have an inverse spinnel structure with oxide anions in a cubic close packed array and (iron) cations occupying octahedral (O_h) and tetrahedral (T_h) sites. The conversion from Fe_3O_4 to γ-Fe_2O_3 is not only thermodynamically feasible in this potential range [93], but also expected to be kinetically facile.

Whether the film in Region 2 consists of two distinct layers or an oxide layer with continuous distribution of Fe^{II}/Fe^{III} is still debated [104,105]. Nevertheless, the formation of more Fe^{III} species in the oxide phase would increase the resistance of the film. The extent of conversion from Fe_3O_4 to γ-Fe_2O_3 appears to be potential dependent, consistent with the previously proposed oxide formation mechanism [84]. The steady-state current is likely determined by the dissolution of Fe^{2+} and Fe^{3+} species from the surface, which will proceed only slowly at pH 10.6. Essentially, the same EIS and current behaviour were observed for all three solutions.

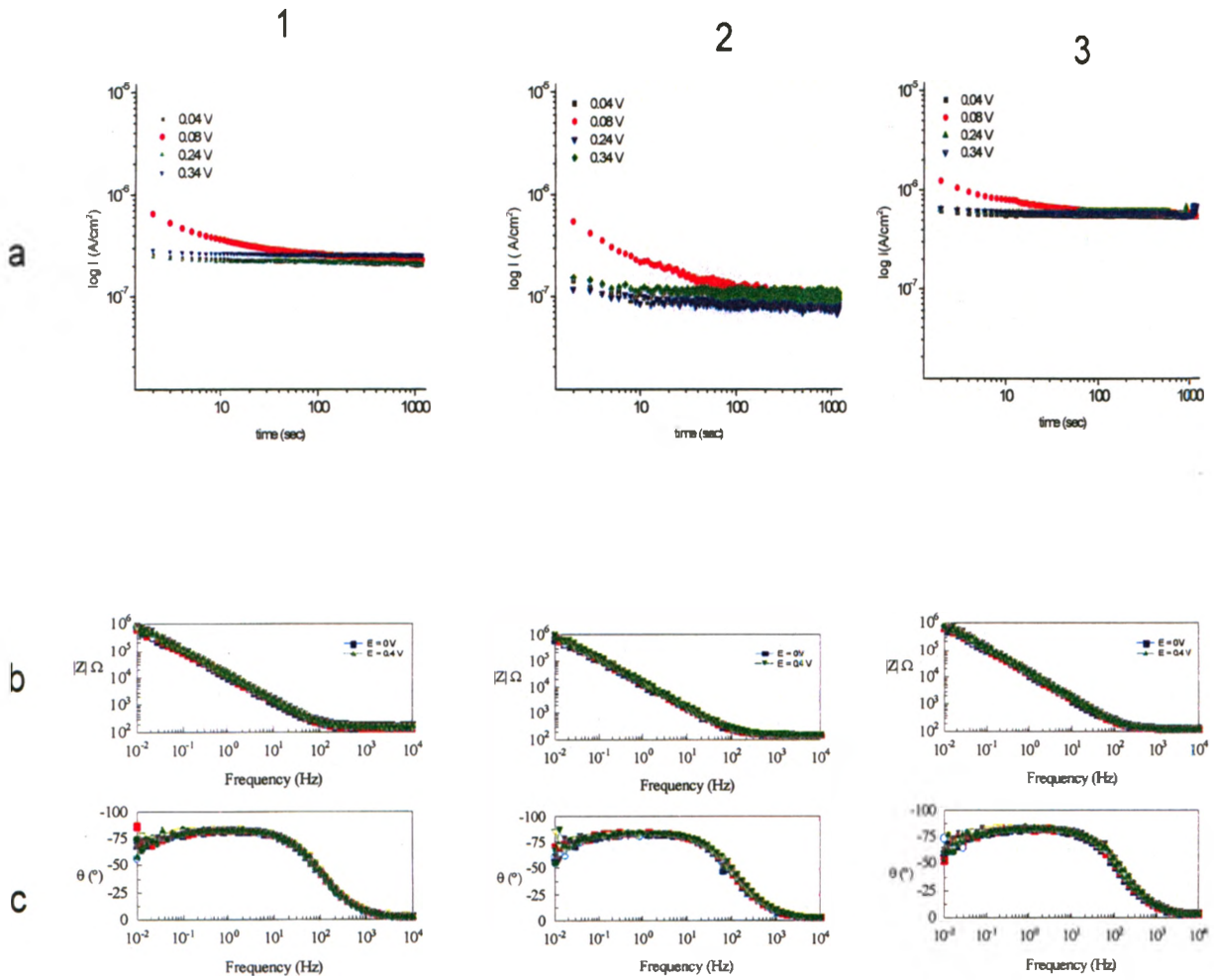

Figure 5-11 :a) Current measured during potentiostatic film growth, using the potential profile illustrated in Figure 4-3, after pre-growth of an oxide at E = -0.6 V for one day in the 10^{-3} M borate solution at pH = 10.6. a1) Borate-only case; a2) KCl; and a3) KBr. (b) EIS response plotted as the log |Z| vs log Frequency at E > 0 V; b1) borate-only case; b2) KCl; and b3) KBr. (c) EIS response plotted as the phase angle (θ) vs log Frequency at E > 0 V; c1) borate-only case; c2) KCl; and c3) KBr

In Region 3, (E > 0.0 V) (Figure 5-11), the current behaviour was similar to that observed in Region 2. The steady-state current is again independent of potential in all three cases, except at E = 0.08 V. This is the potential at which a current surge was consistently observed in the experiments presented in sections 5.2 and 5.2.1. The conversion of Fe_3O_4 to γ-FeOOH is thermodynamically possible for E > - 0.2 V (vs SCE) at pH 10.6. However, the potential drop across the low conductivity outer γ-Fe_2O_3 layer would prevent conversion until a substantial overpotential was present. The conversion of Fe_3O_4 to γ-FeOOH would also require diffusion of water species to the inner magnetite layer. Formation of the γ-FeOOH phase between the magnetite and maghemite layers is likely to create stress since, although the γ-FeOOH phase has a cubic close packed anion structure, the distance between anions is smaller, 0.28 nm [99], than for Fe_3O_4 or γ-Fe_2O_3, 0.3 nm [99]. Such changes could then lead to film fracture

The increase in current when the potential was raised to 0.08 V can be attributed to the onset of a new anodic process, consistent with the conversion of Fe_3O_4 to γ-FeOOH. The potential-independent steady-state current can be attributed to the dissolution rate of Fe^{III} from the outer oxide layer, a potential-independent chemical reaction which would be a function of the solubility of iron species.

When the current does not increase on increasing the potential it can be concluded that fractures caused by the volume change on converting Fe_3O_4 to γ-FeOOH quickly repair by growth of the Fe_3O_4/ Fe_2O_3 layer in the absence of aggressive halide anions. Sometimes, even in the presence of halides, repassivation occurs and pit initiation is not observed, as can be seen from Figure 5-7.

However, in the presence of halides, at a sufficient concentration, repassivation can be inhibited leading to pit initiation. The reason for pit initiation is discussed in section 6, but the key reaction steps preventing passivation are not fully understood. Recently, the presence of a surface film of $FeCl_2.4H_2O$ has been shown to be present at the base of artificial pits [89]. The formation of such a layer, and its subsequent hydrolysis leadings to the formation of $Fe(OH)_2$ could lead to the acidification required to stabilize a pit;

$$\mathbf{FeCl_2 + 2\ H_2O \rightarrow Fe\ (OH)_2 + 2\ H^+ + 2\ Cl^-} \qquad \textbf{5-1}$$

Similarly, any Fe^{3+} produced within the pit environment would lead to acidification,

$$\mathbf{Fe^{3+} + x\ H_2O \rightarrow Fe\ (OH)_x^{(3-x)+} + x\ H^+} \qquad \textbf{5-2}$$

Acidification would increase Fe^{2+} solubility but decrease that of Fe^{3+} since the minimum solubility for Fe^{3+} occurs at a pH < 10.6. However, any $Fe(OH)_3$ deposited within the pit must be unable to cause repassivation.

Although, the exact role of halide is not known it must stimulate metal dissolution and acidification of the breakdown site at the expense of repassivation by oxide growth.

5.4 Surface Analyses

5.4.1 Scanning Electron Microscopy/ Energy Dispersive X-ray Spectroscopy (SEM/EDX)

At the end of the potentiostatic experiment, the surfaces of the carbon steel samples subjected to pitting were examined by SEM and EDX for morphology and elemental analysis, and by Raman spectroscopy and XPS to determine the chemical composition and oxidation states of surface oxides. Figures 5-12, 5-13, and 5-14 show SEM images and EDX maps of the surface around pitted areas formed in the presence of the halides Cl^-, Br^-, and I^-, respectively. Three SEM images are shown for each halide case; (a) the pitted and surrounding areas after the experiment; (b) the same area, but after removing the oxide deposits around the pits; (c) the pitted area (deposits removed) at a higher magnification. These images show that diffusion of soluble corrosion products out of the acidified pit leads to their precipitation around the pit on encountering the slightly alkaline bulk solution. No accurate measure of the number of pits was obtained as this was highly variable from experiment to experiment and no specific dependence of the number or form of pits on the type of halide was observed. Pits also had variable depths but these were not measured.

The same areas were mapped for the elements Fe and O using EDX, Figure 5-12 (d and e), respectively. Generally, the EDX mapping shows a higher ratio of O to Fe (less dense with Fe but denser with O) in and near the pitted areas, compared to the intact (unpitted) surrounding area. This confirms that Fe dissolved within the pit is deposited

around the outside of the pit. In other measurements (not shown) halide was also sometimes detected by EDX at the locations of these deposits.

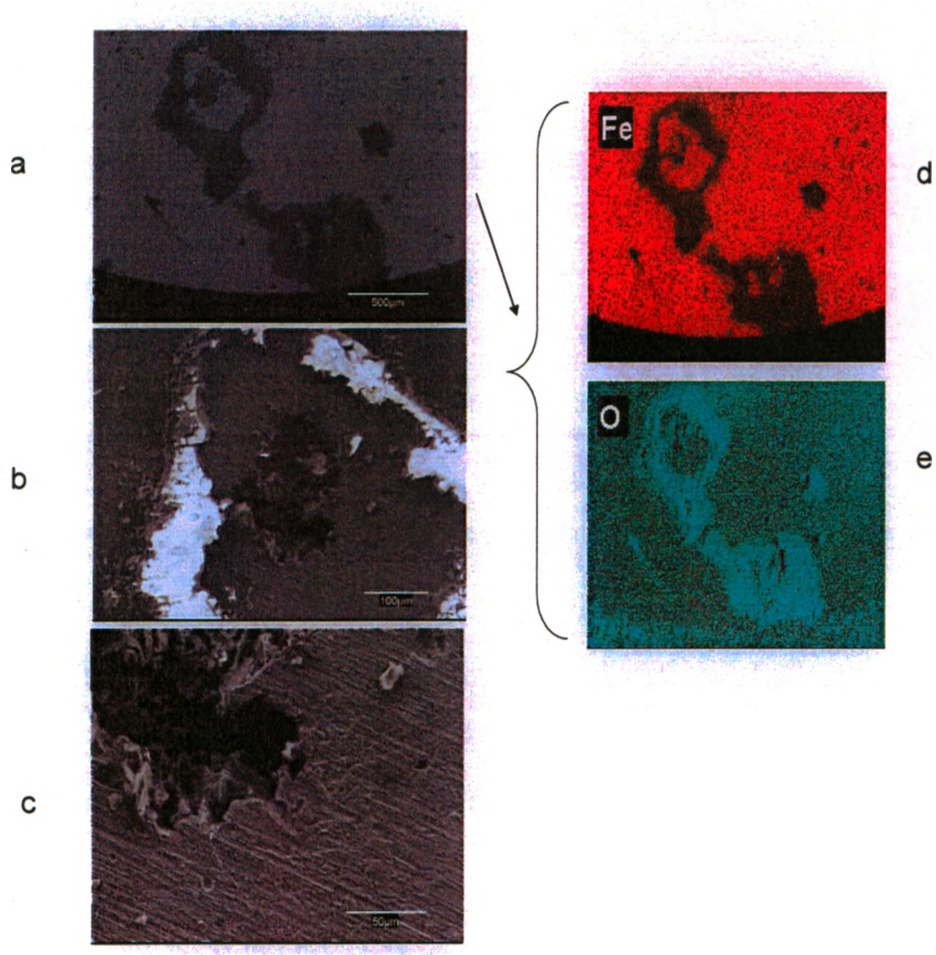

Figure 5-12 :SEM images (a, b,c), and EDX maps (d,e) of the pitted area. The electrode had undergone potentiostatic film growth in Cl^- solution via the procedure illustrated in Figure 4-3: b) the pitted area after removing the corrosion products. c) the magnification of the pitted area

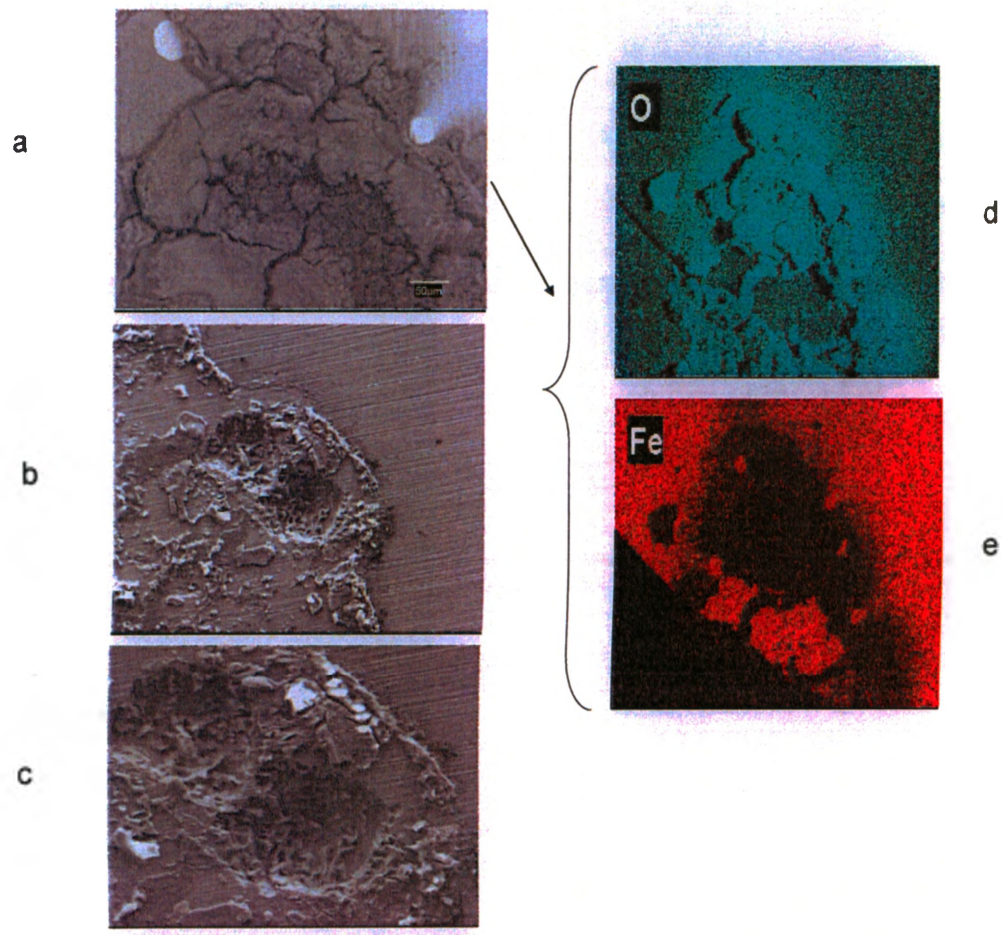

Figure 5-13 : SEM images (a, b,c), and EDX maps (d,e) of the pitted area. The electrode had undergone potentiostatic film growth in Br^- solution via the procedure illustrated in Figure 4-3 b,c) the pitted area after removing the corrosion products.

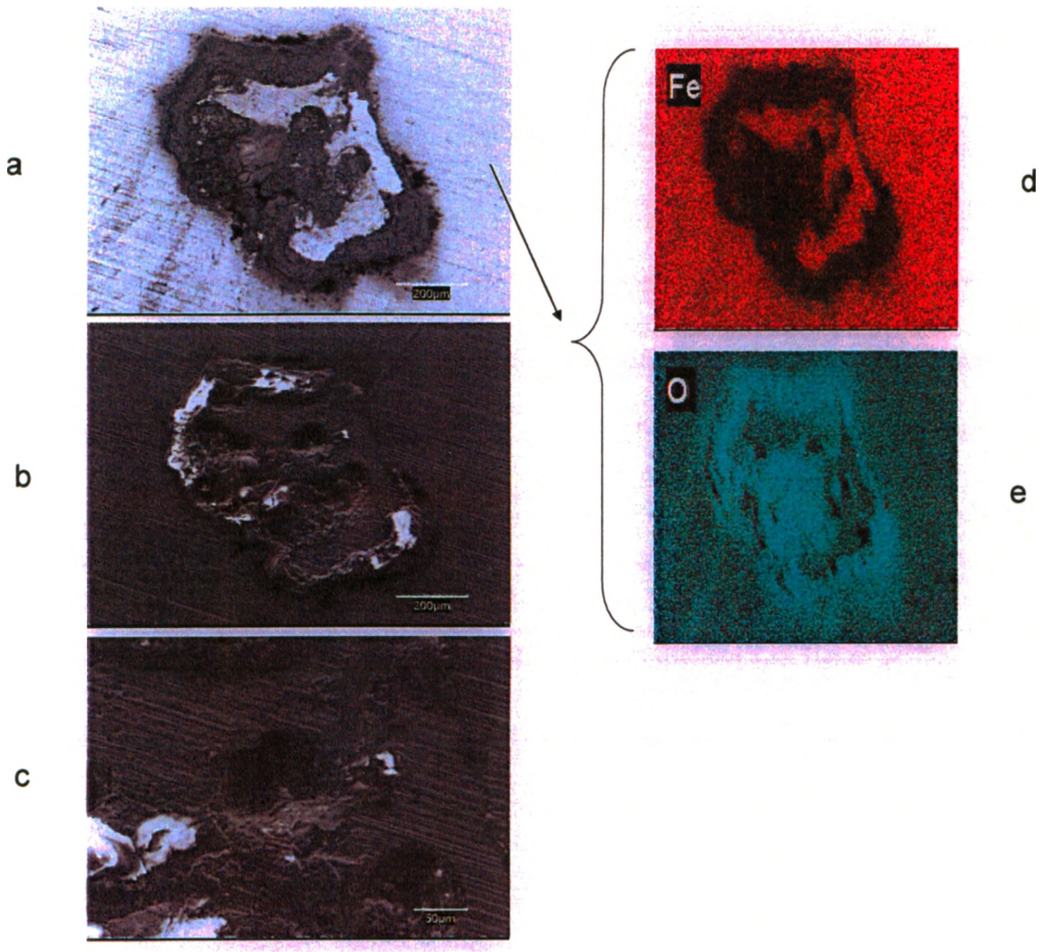

Figure 5-14 :SEM images (a, b,c), and EDX maps (d,e) of the pitted area. The electrode had undergone potentiostatic film growth in I^- solution via the procedure illustrated in Figure 4-3 b,c) the pitted area after removing the corrosion products.

5.4.2 Raman Spectroscopy

Following the potentiostatic step experiments at a series of potentials up to 0.4 V (Section 4.2.2), the electrode surfaces experiencing pitting were further examined by e*x-Situ* Raman Spectroscopy. The Raman spectra of standard iron oxides and oxyhydroxides are compared to those recorded on our electrodes after experiments in the presence of Cl^-, Br^- and I^-, respectively, Figure 5-15. To aid in the assignment of the observed Raman shifts to specific iron oxide or hydroxide phases, the Raman spectra of standard samples of γ-FeOOH, α-FeOOH, γ-Fe_2O_3, α- Fe_2O_3, and Fe_3O_4 were taken on the same instrument in our lab and the main shifts observed are listed in Table 2. The Raman shifts of these standard samples are consistent with those reported by Oblonsky and others [90-91]. Figure 5-16 shows spectra recorded on the pitted area (black) and the passive area (red) after pitting in the presence of Cl^- and I^-.

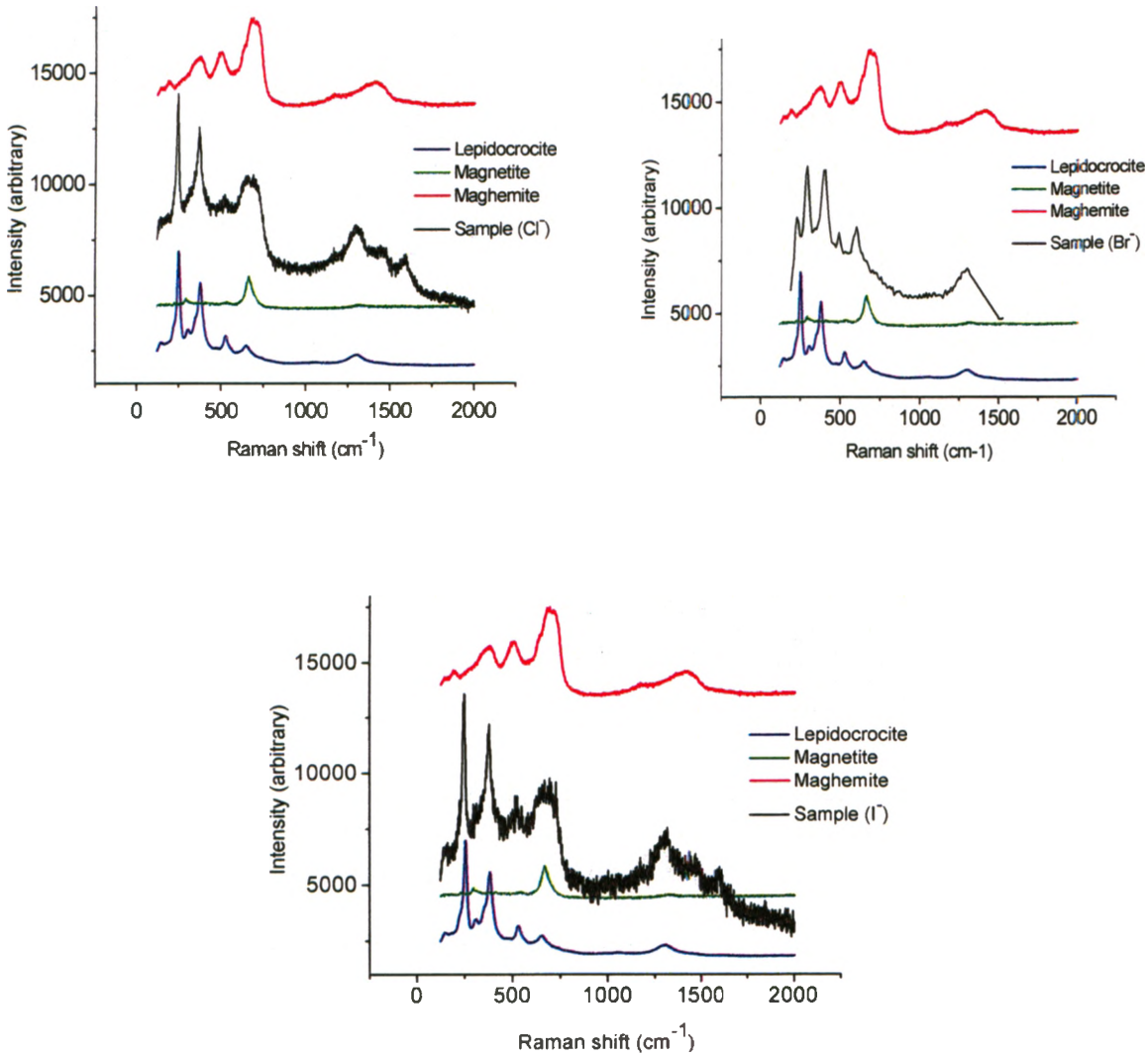

Figure 5-15 : Raman spectra of the corroded carbon steel electrode. The electrode had undergone potentiostatic film growth in Cl^- ,Br^- and I^- solutions via the film procedure illustrated in Figure 4-3.

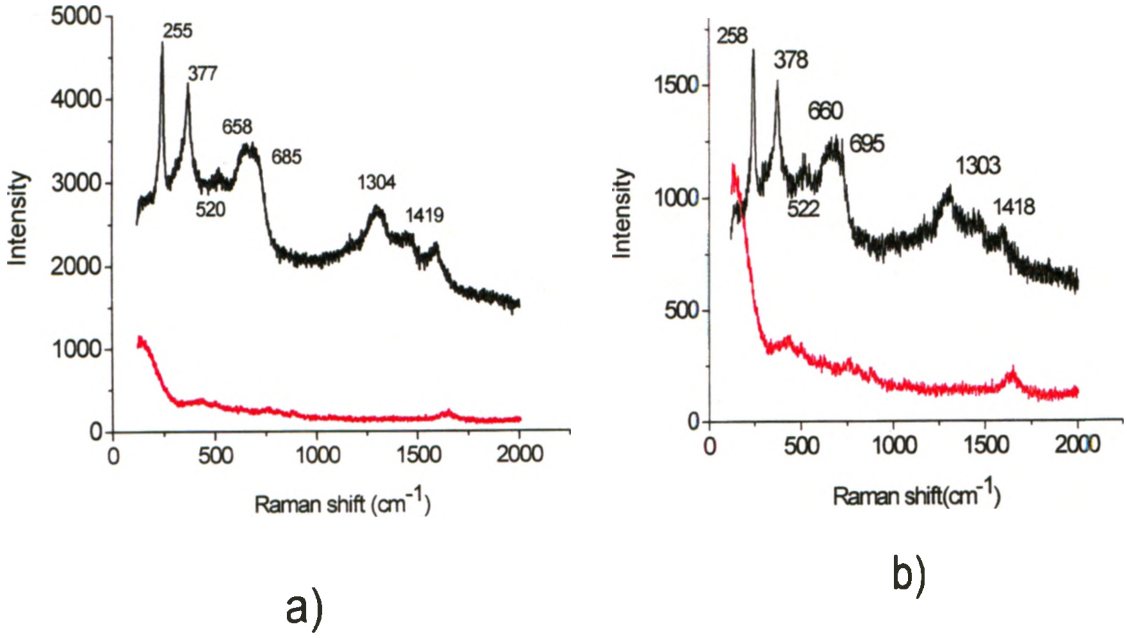

Figure 5-16 : Raman spectra of pitted carbon steel electrodes (substrate red and pitted area black). The electrode had undergone potentiostatic film growth in (a) Cl^- and (b) I^- solutions using the procedure illustrated in Figure 4-3.

Table 5-1 :Raman shifts observed for standard oxides and oxyhydroxides of iron. The strongest shifts are indicated in bold, and the second strongest in italics.

Oxide species	Raman shift (cm^{-1})
Fe_3O_4	*288* **665** (s)
γ- FeOOH	**252** (s) **383** (s) 529 656 1304 (b)
γ-Fe_2O_3	378 513 **690**(s) **715**(s) 1414 (b)
α-FeOOH	245 **355** (s) 479 550
α- Fe_2O_3	**224** (s) , **289** (s) *403* 600

The Raman spectra of surfaces pitted in the Cl^- and I^- solutions are essentially the same: the corroded areas exhibit Raman shifts characteristic of γ- FeOOH with sharp peaks around 252, 383 and a broad peak around 1304 cm^{-1}, and of γ-Fe_2O_3 with peaks around 378, 690 and 1414 cm^{-1}, and of Fe_3O_4 with a peak at 665 cm^{-1}. Unpitted areas show no significant peaks that can be attributed to any oxide phase, probably due to the thinness of the oxide film (expected to be < 10 nm).

The *ex-situ* Raman spectrum observed for the corroded surface in Br^- solution differs from those of the other halide cases, since it shows peaks that are characteristic of α-Fe_2O_3 at 224 and 403 cm^{-1}, in addition to those of γ- FeOOH around 252, 383 and 1304 cm^{-1}, and γ-Fe_2O_3 at 378 690, and 1414 cm^{-1}. The Raman shift around 675 cm^{-1} is attributed to Fe_3O_4, and γ-Fe_2O_3 which overlap. The formation of γ-Fe_2O_3 from Fe_3O_4 and $Fe(OH)_3$ is known to easily occur on air exposure [93]. Hence, it was suspected that this surface was exposed to air during drying and transferring for Raman analysis. This hypothesis was tested by performing *in-situ* Raman Spectroscopy of the carbon steel surface near the end of the potentiostatic experiment in Br- solution. Figure 5-17 shows the optical image and the Raman spectrum of the pitted area of the corroding surface in the Br^- solution.

The *in-situ* spectrum of the corroded area shows the same Raman shifts observed in the *ex-situ* spectra of the Cl^- and I^- cases, with shifts characteristic of γ-FeOOH, γ-Fe_2O_3 and Fe_3O_4. The *ex-situ* and *in-situ* Raman results show that the pitting corrosion products on carbon steel at the end of the potentiostatic step experiments in halide solutions consist of γ-FeOOH, γ-Fe_2O_3 and some Fe_3O_4, and the composition does not appear to depend on the type of halide.

a

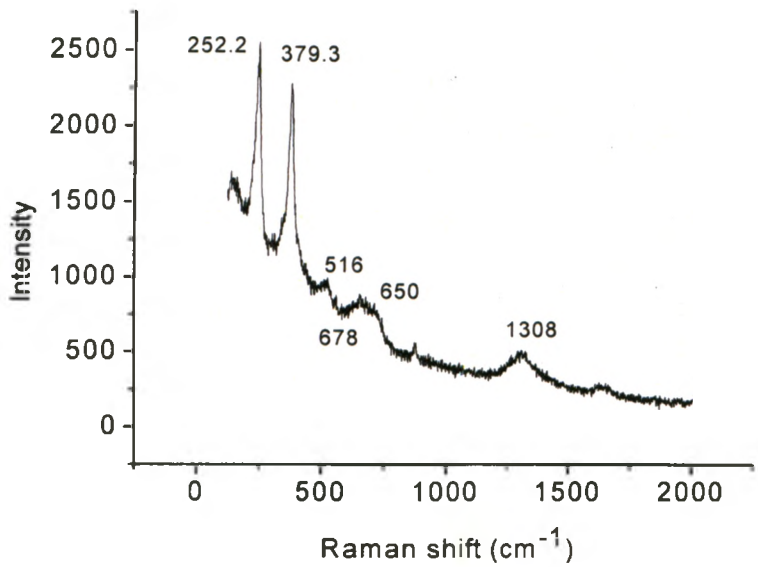

b

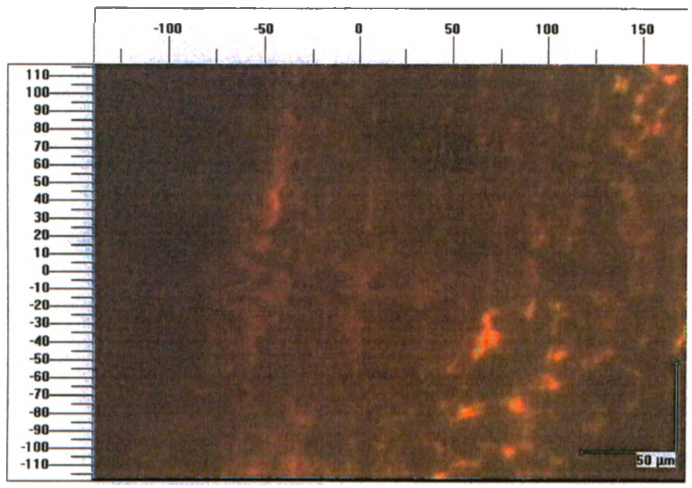

Figure 5-17 :a) In-situ Raman spectrum of a pitted carbon steel electrode. The electrode had undergone potentiostatic film growth in Br^- solution via the procedure illustrated in Figure 4-3. b) Optical image of the pitted area.

5.4.3 X- Ray photoelectron Spectroscopy (XPS)

X-ray photoelectron spectroscopy (XPS) was used to study the oxidation state of iron species and the chemical form of O in the films formed in potentiostatic step experiments. After 1 day of oxide growth at -0.6 V, the potential was increased stepwise in 20 mV increments every 40 min to a desired potential (E = 0.2 V). The electrodes were then removed from the cell, washed with deionized water, and dried with Ar gas. To minimize exposure to air, electrodes were transferred to a glass vial inside a glove box. The electrodes examined did not show pitting up to E = 0.2 V. (See section 5.2.3 for more details).

No evidence was found for Cl^- in the survey XPS spectra, which is consistent with the interpretation that Cl^- was not incorporated into the oxide film. A peak for Cl-2p would be observed around 199 eV, and for Cl-2s around 269 eV. As shown in Figure 5-18, no peaks for Cl^- are observed in these binding energy ranges. Similar investigations by Khalil et al [92] using XPS also did not reveal any Cl^- in passive films grown in Cl^- - containing solutions.

An example of a high resolution XPS spectrum for the Fe-2p and O 1s regions, recorded on an oxide film formed at 0.2 V in Cl^- solution is shown in Figure 5-19 (a,b). In addition to the Fe-2p oxide peaks at 709.5 eV for Fe^{II} and 710.5 eV for Fe^{III}, the peak at 707 eV for metal iron [93] is commonly observed in all XPS spectra, indicating that the thickness of the oxide film is less than the maximum escape depth of the photoelectrons from the material. This result suggests that the oxide thickness is < 10 nm. Biesinger et al [95] have calculated the thickness of the oxide film on iron using the

Strohmeier overlayer equation (Equation 5-3), and various data [94] for the mean free path lengths appropriate for the oxides of iron and iron metal,

$$d = \lambda_0 \cdot \mathbf{Sin}\ \theta \cdot \mathbf{ln}\left(\frac{N_m \lambda_m I_0}{N_0 \lambda_0 I_m} + 1\right) \qquad \textbf{5-3}$$

In this equation the subscripts *o* and *m* represent the oxide and metal, respectively, θ is the electron take-off angle used, *N* is the volume density of metal atoms in either the bulk metal or oxide phase, λ is the energy loss due to inelastic electron scattering in the respective phase, and *I* represents the intensity (peak area) of either the metal or the oxide Fe-2p signal. The maximum depth probed using this method is about 10 nm. Using values from Beisinger's calculations the thicknesses of iron oxides formed at different final potentials have been calculated, Figure 5-20 [95]. This figure shows that the oxide thickness does not show any increase at final potentials < 0.0 V, but does increase when the final potential is greater than 0.0 V, i.e., in potential Region 3 where the film is undergoing breakdown and repair.

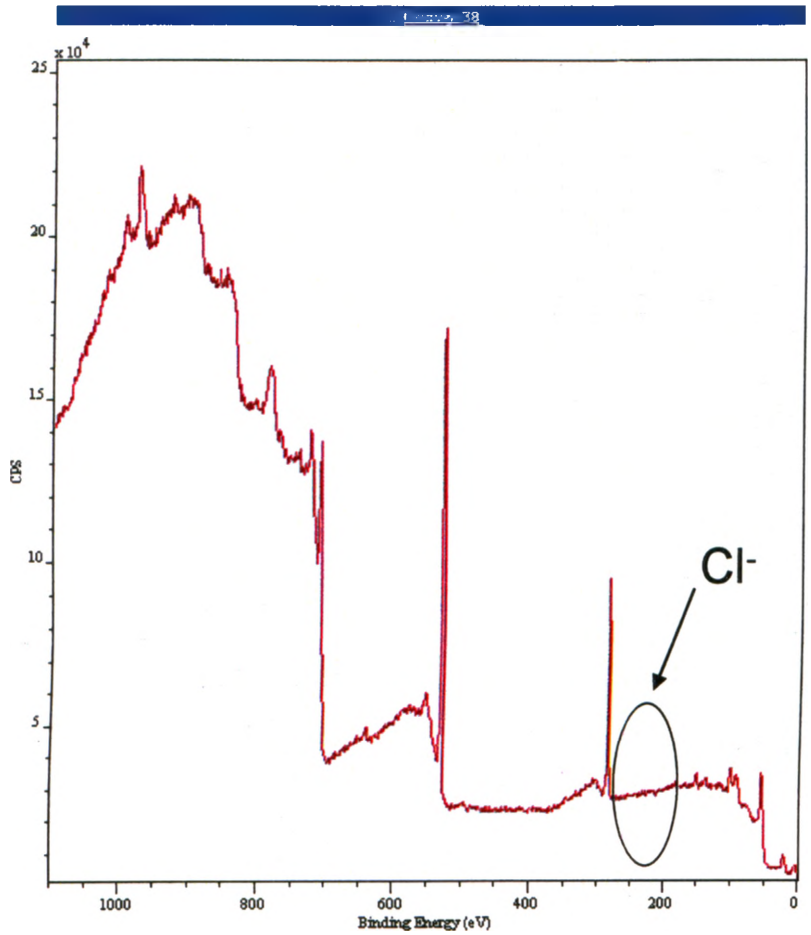

Figure 5-18 :XPS survey spectrum of a iron oxide film grown using the potential profile described in Figure 4-3 up to a final potential E = 0.2 V after pre-growth of a magnetite film at E = -0.6 V for one day in Cl^- solution.

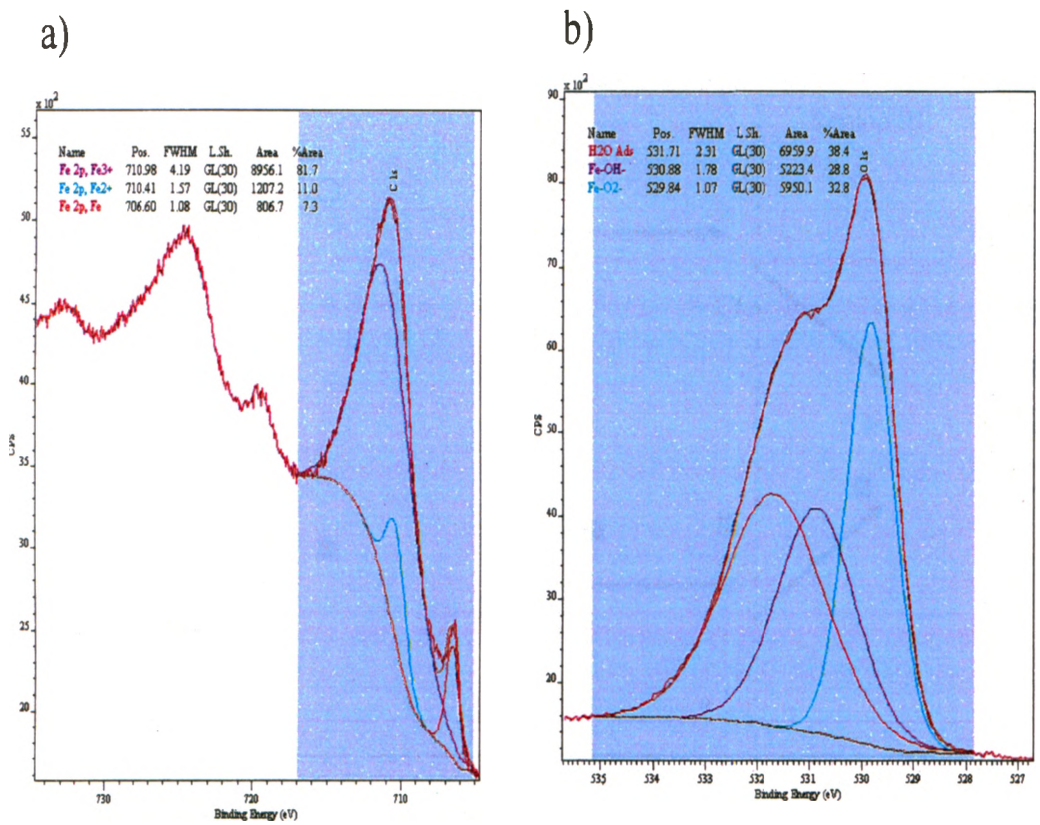

Figure 5-19 :High resolution XPS Spectra of the Fe-2p and O-1s peaks on an oxide film formed grown using the stepwise potential profile described in Figure 4-3 up to a final potential of E = 0.2 V after pre-growth of a magnetite film at E = -0.6 V for one day in Cl^- solution.

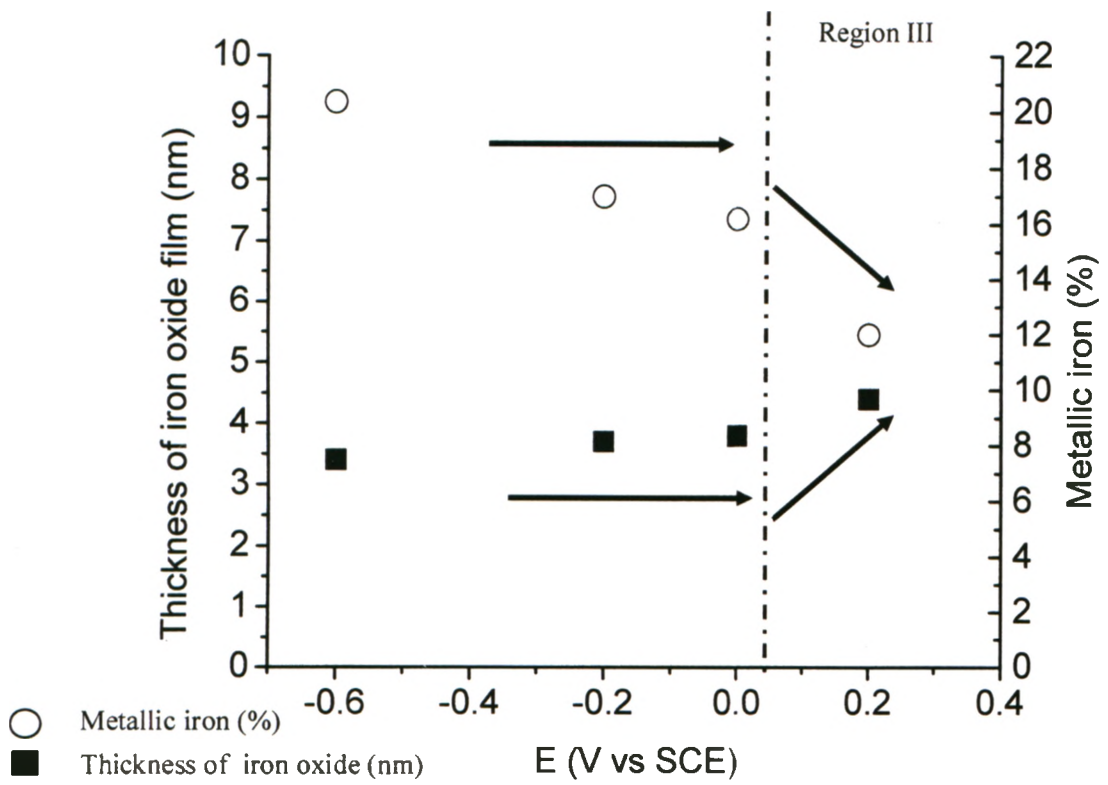

Figure 5-20 : Thickness of the iron oxide film as a function of potential (■) and the atom % of metallic iron as a function of potential (○).

Additional proof that the thickness of the film increases with potential can be obtained by observing the change in area of the metallic iron peak as the potential is increased in to region 3, Figure 5-20. This value roughly represents the depth to which X-rays can penetrate into the metallic iron under the oxide layer. The atom percentage of metallic iron shows a significant decrease when the potential is increased above 0.0 V.

The average oxidation state of the film can also be estimated. The position of the Fe-2p peak is plotted as a function of the applied potential in Figure 5.21. The binding energies for Fe-2p for wüstite (FeO) and (γ-FeOOH) are 710.4 eV and 711.5 eV, respectively. A gradual shift in the iron oxide peak position to higher binding energy with increasing potential indicates an increase in that ratio of Fe^{III} to Fe^{II}.

To determine the change in oxide content, the ratio of the area of O-1s peak in the oxide film as a function of potential is plotted in Figure 5-22. This figure shows a significant increase in the ratio of oxide content at the expense of the ratio of hydroxide content as the potential is increased through region 1 and 2. However, once the potential is increased in to region 3 and above a potential of 0.08 V, when corrosion of Fe_3O_4 to γ-FeOOH corrosion, the hydroxide content increases again.

These results are consistent with an increase in film thickness due to the growth of the Fe_3O_4 and γ- Fe_2O_3 phase at expense of $Fe(OH)_2$ or $Fe(OH)_3$ at low potentials. Once $E > 0.0$ V, the contribution of γ-FeOOH to the thickness of the film increases considerably, while that for Fe_3O_4 and γ- Fe_2O_3 decreases

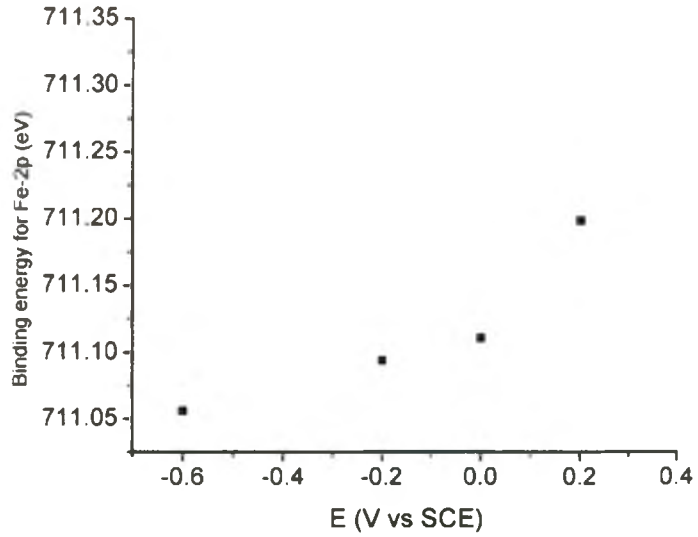

Figure 5-21 :Fe-2p binding energy of as a function of potential.

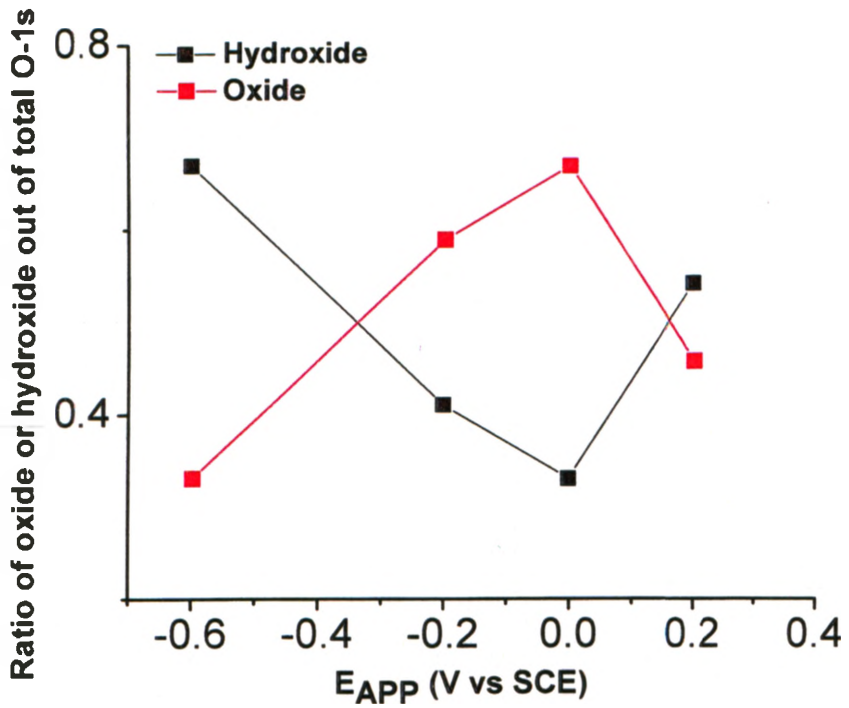

Figure 5-22 :Ratio of the area of oxide/hydroxide out of the total O-1s peak.

Chapter 6

6 PROPOSED FILM BREAKDOWN MECHANISM

Pitting is a localized process, which can be separated temporally into initiation and propagation steps. Initiation occurs when the protective (or passive) surface-oxide film is breached, opening up flaws and exposing the substrate metal to the solution. Generally, prior to initiation, the electrochemical potential of the corroding system is high because of the presence of the passive film, which acts as a resistive barrier to charge transfer processes prior to its breakdown. Consequently, on initial film failure, a high overpotential exists, which causes rapid oxidation of the underlying oxide or metal substrate. If this oxidation process favours the reformation of the passive oxide (i.e. the solubility of metal cations and their tendency to hydrolize are low), passivity can be restored. On the other hand, if metal dissolution leads to the formation of soluble cations, their hydrolysis could occur via reaction 6-1 leading to a decrease in the pH close to the substrate surface, especially within flaws which limit diffusion of protons away from the breakdown location,

$$M^{n+} + H_2O \rightarrow MOH^{(n-1)+} + H^+ \qquad 6\text{-}1$$

If the pH decreases in this manner, cation solubility is generally increased and repassivation strongly inhibited. As a result, once pitting is initiated, anodic dissolution inside the pit can proceed rapidly, leading to extensive pitting damage.

As the pit propagation rate is primarily controlled by the local environment inside the pit, and this environment is difficult to control or assess, it is important to determine the mechanisms and conditions leading to pit initiation.

Figure 6-1 shows that for Fe^{III} hydrolysis different Fe^{III} species such as $Fe(OH)^{2-}$, $Fe(OH)_2^{+}$, and $Fe_2(OH)_2^{4+}$ are rapidly formed,

$$\mathbf{Fe^{3+} + x\ H_2O \rightarrow Fe(OH)_x^{(3-x)+} + x\ H^+} \qquad \mathbf{6\text{-}2}$$

In the presence of halides, the formation of halides salts on the rapidly dissolving metal surface is thought to prevent repassivation but not hydrolysis as illustrated in Figure 6-1. Soluble Fe^{III} species which diffuse out of the pit will precipitate on encountering the much higher pH prevailing in the bulk of the solution.

Galvele et al [96] among others first proposed that metal ions hydrolyze inside pits, and that the corrosion products are transported out of the pit by diffusion. They also proposed a mechanism involving passivity breakdown at the initial stages of pit growth: due to localized acidification stemming from the hydrolysis of the few metal ions formed by the low (passive) anodic corrosion current. Following corrosion processes, Baylis et al. observed a bulk pH value of about 5 inside steel water pipes. They explained this slight acidification as being caused by the hydrolysis of anodically formed Fe^{II} and Fe^{III} ions resulting in the formation of Fe_3O_4 and various hydroxides or basic salt compounds along with the release of protons.

Since pitting, once initiated, can propagate rapidly, from the perspective of corrosion control, it is important to understand the mechanisms and conditions leading to

pit initiation and to develop a methodology to prevent it. As, mentioned above, for pitting to initiate, the passivity of the surface film must be compromised. As discussed in section 5.2, this can be achieved in halide-containing solutions. The results in this thesis can be discussed in terms of two possible initiation mechanisms.

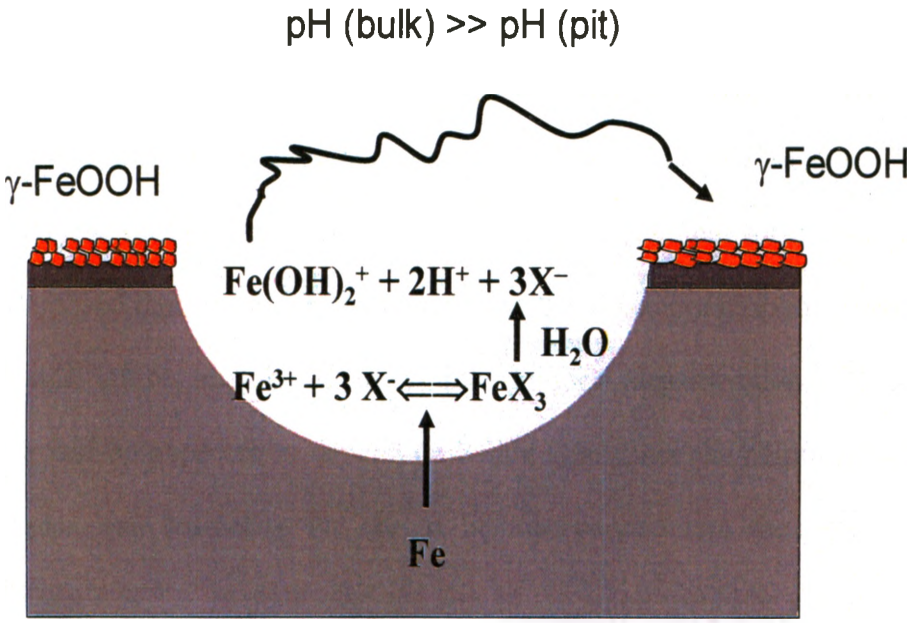

Figure 6-1 :Schematic of the pit propagation mechanism

6.1 Initiation Mechanism I: Influence of Halide on Passive Film Formation

In this mechanism, halides are either incorporated into the metal-oxide matrix during its growth, resulting in a progressively more defective film, or they prevent a

defect-free passive layer from forming. After prolonged exposure to halide solutions, such a film would become extensively defective, which would eventually lead to film fracture and/or the formation of micro pores. Through this initiation mechanism, E_B would be expected to depend on the type of halide, since their physical and chemical properties (e.g. size and electronegativity) that could influence oxide formation, vary significantly between halide species. Such mechanisms have been proposed by many researchers [46,48,49,54-56], who have suggested that the presence of Cl^- increases the solubility of iron species, resulting in an overall thinning of the passive layer. This would eventually lead to pitting if the potential is above a critical value. Other researchers [39-45] have proposed that oxide film breakdown involves incorporation of chloride directly into the oxide lattice, making it susceptible to local depassivation. Both of these processes would be expected to depend on halide type, since the ability of Br^- and I^- to either complex and solubilize Fe^{2+} or to be incorporated into the oxide, should be different to that of Cl^-. In particular, the size of the anion would be expected to have a very large effect on its ease of incorporation into defects in the oxide.

6.2 Initiation Mechanism II: Oxide Conversion and Opportunistic Halide Attack

In this mechanism, the halides are not involved in film formation, but take advantage of oxide hydroxide conversion processes in existing films. If these processes lead to development of interfacial stresses due to different lattice parameters and the ensuing volume changes, they could induce film fracture. Thermodynamic calculations

show that the conversion of Fe_3O_4 to γ-FeOOH on carbon steel occurs at high potentials (> 0.0 V at pH 10.6), and would be accompanied by a significant volume change at the steel/oxide interface, since their normalized volumes (volume per iron atom in a unit cell) are 0.1973 nm^3 and 0.1493 nm^3, respectively [99]. Also, the distance between to adjacent O^{2-} ions is about 0.298 nm [99] which is longer than the distance between cations. Therefore, metal ions can occupy the interstitial sites without affecting the O-O distance. In addition, this conversion involves the transformation of an inverse spinel (Fe_3O_4) to an orthorhombic structure (γ-FeOOH). The fractures induced by these changes could lead to exposure of the base metal to solution, and allow halide access to the metal surface. This would prevent repassivation by increasing cation solubility, promoting hydrolysis of dissolved Fe^{3+}, and allowing pit propagation (Figure 6-2). With this mechanism, E_B would be expected to be independent of the nature of the halide, but dependent on the properties of the film.

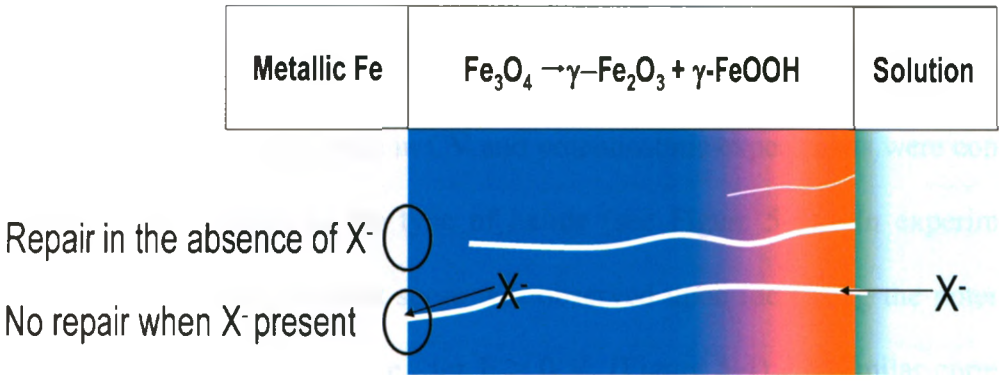

Figure 6-2 : Illustration of the proposed mechanism II for film breakdown in the absence of halide followed by film repair, and in presence of the halide followed by pit initiation.

6.3 Results Supporting Mechanism II

The hypothesis proposed in section 6.1 is the more popular one [96-103] although there is a lack of agreement in the literature on the influence of halide (e.g. Cl^-) on the passive film [96-103]. However, El-Nagger et al [100] suggested that penetration of aggressive anions (e.g. Cl^-) into the passive layer occurs without destroying its passivity prior to pit initiation, which is more consistent with mechanism II. In their scenario, the dissolution of the metal follows when Cl^- reaches the bare metal. Using Secondary Ionization Mass Spectroscopy (SIMS), Auger Electron Spectroscopy (AES), and XPS, Goetz et al [101] showed that oxide films formed on Fe in 0.5 M Cl^- solution are, in fact, Cl^- free; i.e., Cl^- does not incorporate into the passive oxide. By forming the oxide film in short time periods they also proved that the Cl^- is neither a precursor nor a cause of pit initiation. As well, in a recent study by Smialowska et al, [30] it was demonstrated that no Cl^- ions were found in the (inner) barrier or passive layer but only in

the outer layer of the film. This result suggests that a mechanism involving Cl^- penetration through the passive layer prior to pit initiation may be incorrect. In our results, the values of E_B observed in CV and potentiostatic experiments were consistently > 0.0 V and independent of the type of halide (see Figure 5-4). In experiments not leading to pitting, a brief current surge was observed upon increasing the potential into the breakdown potential range, i.e., for E > 0 V, (Figure 5-4). A similar current surge was observed for carbon steel immersed in halide-free solutions, suggesting that the film breakdown occurred irrespective of the presence of halide, which supports pit initiation via Mechanism II.

In general, there must be a relationship between pit initiation and the disordering of the passive layer. The mechanical stresses induced by the oxidative formation of the γ-FeOOH within the passive layer may be the actual reason for the increase of the nucleation rate which is demonstrated by the brief current spike throughout all the experiments at E = 0.08 V. For halide free solutions, the fracture is rapidly followed by repassivation and pit propagation is avoided, as shown in Figure 6-2. The particular causes for the conversion of Fe_3O_4 to γ-FeOOH will be discussed in the next section

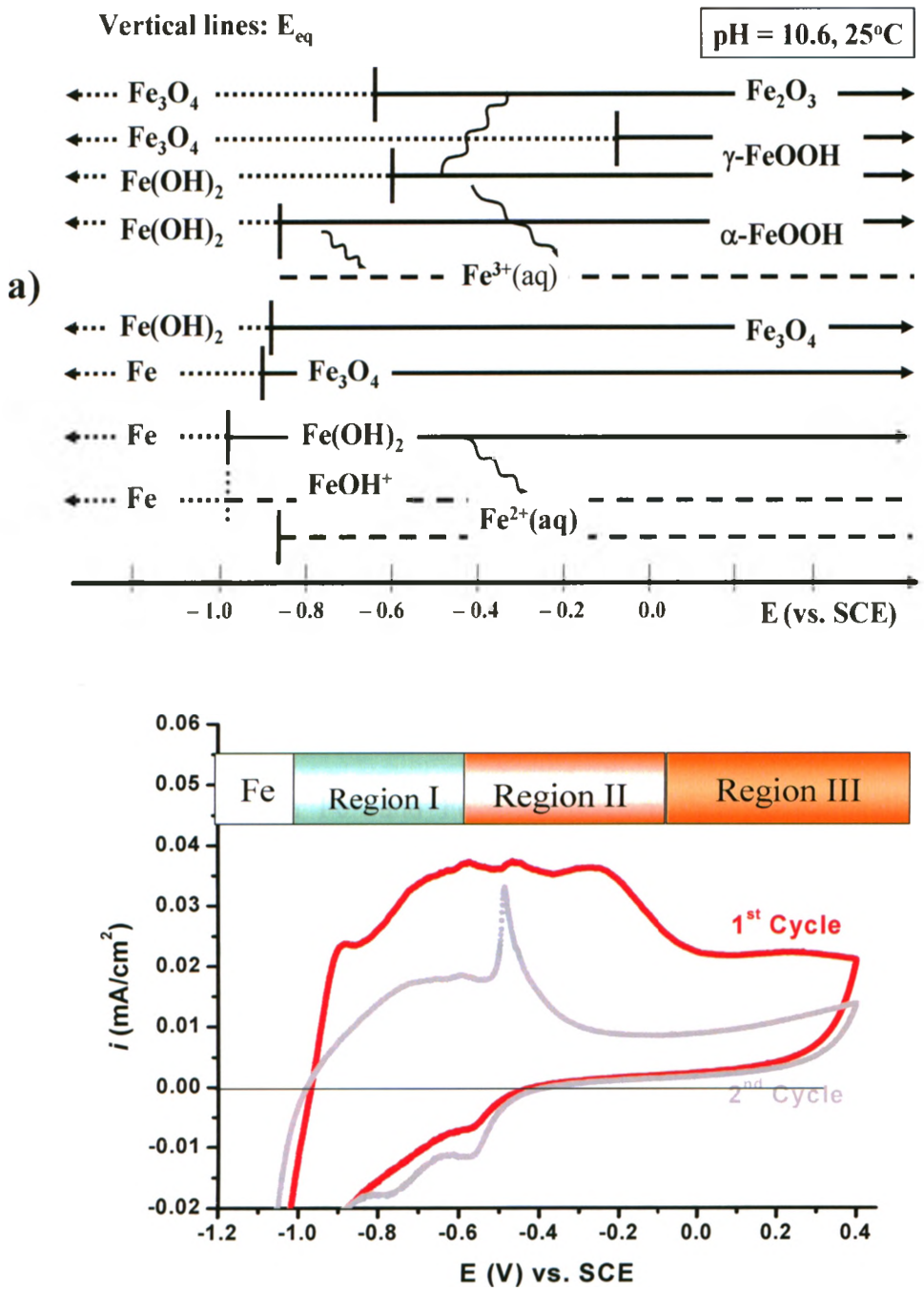

Figure 6-3 :a) Thermodynamic equilibrium potentials for a series of compounds at room temperature and pH 10.6. b) Cyclic voltammograms recorded on carbon steel in 0.01 M borate buffer solution at pH = 10.6 [102].

6.4 In Depth Analysis of Carbon Steel Films as a Function of Potential

Previous studies on the electrochemical properties of carbon steel in halide free borate solutions at pH = 10.6 [84,102] have suggested that the oxidation behaviour of carbon steel can be grouped into three potential regions as illustrated in Figure 6-3.

1- Region I (-0.8 V < E (V vs SCE) < -0.5 V)

2- Region II (-0.5 V < E (V vs SCE) < 0.0 V)

3- Region III (0.0 V < E (V vs SCE) < 0.4 V)

6.4.1 Region I (-0.8 V < E (V vs SCE) < -0.5 V)

In this region both Fe^{II} and $Fe^{II/III}$ oxides are thermodynamically feasible. Oxidation of Fe to Fe^{II} as well as either Fe or Fe^{II} to $Fe^{II/III}$ oxide phases will occur. Possible species include FeO, and $Fe(OH)_2$ for Fe^{II} and Fe_3O_4 for $Fe^{II/III}$

Figure 6-4)

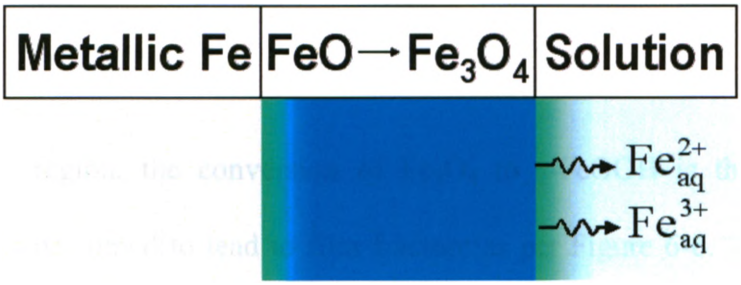

Figure 6-4 :Schematic of film formation processes possible in region 1

6.4.2 Region II (-0.5 V < E (V vs SCE) < 0.0 V)

In this potential region, oxidation of Fe to Fe^{II} and $Fe^{II/III}$ continues to occur. However, the conversion of FeO, $Fe(OH)_2$ and Fe_3O_4 to γ-Fe_2O_3 is also thermodynamically feasible. Kinetically, the conversion of Fe_3O_4 to γ-Fe_2O_3 should be facile because both have a similar cubic crystallographic structure. In general, the inner oxide layer is expected to be Fe_3O_4, while γ-Fe_2O_3 would be formed as an outer layer. The average valence of Fe would increase with an increasing in potential. Figure 6-5 illustrates the inner and outer phases formed in this region.

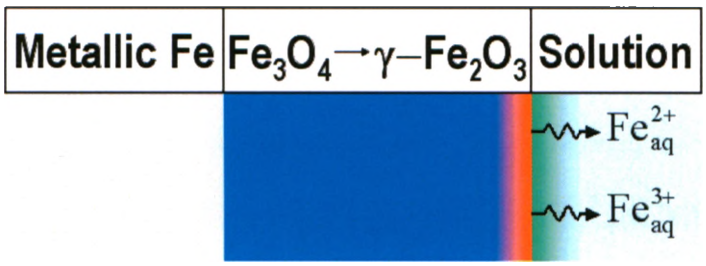

Figure 6-5 :Schematic of film formation processes possible in region 2

6.4.3 Region III (0.0 V < E (V vs SCE) < 0.4 V)

In this region, the conversion of Fe_3O_4 to γ-FeOOH is thermodynamically possible. This is presumed to lead to film fracture as per Figure 6-6. In the absence of aggressive anion (e.g. halides) the film quickly be repassivated or repaired whereas in the

presence of aggressive anion such as halides initiation of pit might be occurred. (Figure 6-6) [84]

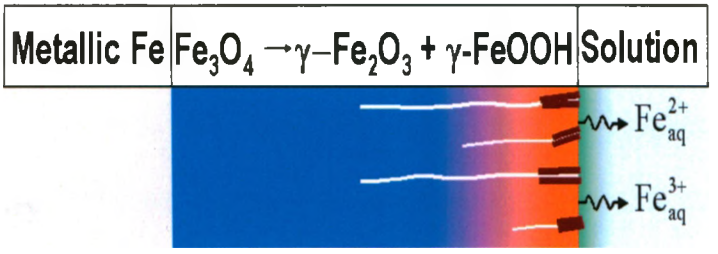

Figure 6-6 :Schematic of film formation process possible in region 3

Chapter 7

7 SUMMARY AND CONCLUSIONS

7.1 Summary

The primary goal of this research was to determine the processes which cause film breakdown leading to pitting of carbon steel in solutions containing halide anions. It is commonly accepted that the influence of Cl^- on passive film properties is the key feature in breakdown, and the possibility that transformations in the oxide are responsible has not been considered. Electrochemical techniques such as electrochemical impedance spectroscopy (EIS), cyclic voltammetry and amperometry, and surface analytical methods such as SEM, in-situ/ex-situ Raman spectroscopy and XPS have been used to investigate the changes in film properties leading to breakdown in borate-buffered solutions at pH = 10.6 containing either Cl^-, Br^- or I^-. The following results have been obtained in this research:

- The key observations from the voltammetric studies include:
    - The film breakdown, or pit initiation, potential is always more positive than 0.0 V (vs SCE), and has no systematic dependence on halide type.
    - On the reverse scan, the current decays immediately to near zero when pitting has not occurred. When pitting has occurred, the current remains

anodic until the potential reaches –0.4V ± 0.05 V. This potential at which the current becomes zero ($E_{i=0}$) is also independent of the type of halide.

- The key observations from the potentiostatic film growth experiments in which the potential is increased stepwise include:
  - Film breakdown indicated by a high steady-state current, never occurs at a potential less than 0.0 V, consistent with the minimum pit initiation potential observed in the voltammetric studies. Comparison to previous studies shows that potentials at, or above, this value are in the region where oxidation of magnetite (Fe_3O_4) to lepidocrocite (γ-FeOOH) could lead to a significant volume change in the thin oxide film leading to a susceptibility to pit initiation.
  - On the reverse voltammetric scans, ($E_{i=0}$) = –0.4V ± 0.05 V, independent of the type of halide, when pitting has occurred during the stepwise potential increase. This is the same zero-current potential value observed in the voltammetric studies. When pitting has not occurred, ($E_{i=0}$) is much higher at 0.2 ± 0.05 V, and identical for solutions containing one of the three halides, as well as for halide-free solution.
  - The thickness of the inner magnetite layer, controlled by changing the duration of the prefilm growth in this study, does not change the above general observations, although the thicker prefilm in general results in higher pit initiation potentials due to longer times required for the effect of halide to show for the thicker film. This confirms that the film properties, not the halide type, determine the breakdown potential.

- The time of halide addition does not change the general observations either; the halide addition when the potential is less than 0.0 V does not lead to pitting while it often leads to pitting when the potential is > 0.0 V whether halide is added before or after the potential is increased to these values.

- The EIS analysis of the film as a function of potential observed during the stepwise potential increase shows that;
  - The oxide film properties change considerably over the potential range – 0.42 V to 0.0 V (region II). Previous studies show that, in this potential range, the film is undergoing conversion from magnetite to maghemite (γ-Fe_2O_3), both of which share the same phase structure.
  - No further changes in the EIS spectra with potential are observed when E > 0.0 V for non-pitting cases.
  - The potential dependent behaviour of EIS is independent of the presence or the type of halide in the solution.

- The XPS analyses of the surface as a function of potential during the stepwise potential increase for non-pitted films in halide containing solutions show that,
  - No halide peaks are observed, indicating that halide ions are not incorporated into the oxide film.
  - The film thickness determined by the relative contributions of oxidized and metallic Fe to the Fe-2p band shows a distinct increase when the potential is increased above 0.0 V. This increase coincides with an increase of the OH contribution to the O-1s band. This is consistent with

acceleration of film thickening via a breakdown/repassivation process at E > 0.0 V.

- The key observations from the surface analyses of pitted films include
  - SEM/EDX analyses of pitted areas show a considerable deposition of iron oxides/hydroxides outside of the pit, and no trace of halide in the pit.
  - Raman spectroscopy of carbon steel electrodes pitted in halide-containing solutions indicate the presence of magnetite, lepidocrocite, maghemite, and hematite as corrosion products.

The above observations are consistent with the film formation/conversion mechanism on carbon steel in two potential regions (II and III) previously identified in halide-free solutions. In region II (below 0.0 V) the magnetite layer that has been formed at lower potentials can grow but also convert to maghemite (γ-Fe_2O_3). However, both share the same phase structure and hence the conversion is kinetically facile and leads to no stress in the film despite the film becoming more passive. In region III (above 0.0 V), the oxidation of magnetite (Fe_3O_4) to lepidocrocite (γ-FeOOH) could lead to a significant volume change and micro film fractures.

In the absence of halide, any release of Fe^{2+}/Fe^{3+} within these fractures would lead to a suppression of pH due to cation hydrolysis. However the solubility minimum for Fe^{3+} is at approximately pH 8, and the ensuing decrease in cation solubility would favour repassivation as always observed. However, in the presence of halides, the film fractures introduce facile pathways for the transport of halides to the metal surface at the

base of fractures. Since the dimensions of fractures will be considerably larger than the size of the halide ions, halide–type would be expected to be irrelevant. Once access to the metal surface is achieved, halides could then interfere with the repassivation process, thereby allowing the initiation of stable pits.

7.2 Conclusions

It is concluded that the halide ions do not degrade the properties of the oxide film leading to pit initiation, but take advantage of fractures induced by the conversion of magnetite to lepidocrocite at the steel/oxide interface. In the absence of halide, any release of Fe^{2+}/Fe^{3+} within these fractures would lead to a suppression of pH due to cation hydrolysis. However, the solubility minimum for Fe^{3+} is at ~ pH 8, ensuring a decrease in cation solubility, and thus, favouring repassivation. In the presence of halides, halides can be easily transported to the metal surface at the base of fractures. Once access to the metal surface is achieved, halides could then interfere with the repassivation process, thereby allowing the initiation of stable pits. For such a process, involving the transport of halides through fractures in the film, the significant differences in halide ion sizes would be unimportant.

7.3 Additional Required Research

- The dependence of pitting potential on pH should be measured. The conversion of magnetite to lepidocrocite would be expected to be pH-dependent, leading to a change in breakdown potential with pH.
- The thickness of the magnetite layer at the steel/film interface would be expected to increase with temperature, leading to an influence on the breakdown potential.
- A similar study on iron, as opposed to carbon steel, should be conducted. This could indicate whether the film breakdown events are influenced by the coexistence of ferrite and cementite grains in the steel.

REFERENCES

1. David G. Rethwisch, W.D. Callister, Fundamental of Materials; Science and Engineering, 3rd Edition, John Wiley and Sons, 2008
2. William D. Callister, Jr. Materials Science and Engineering and Introduction, 6th Edition, John Wiley and Sons, 2003
3. CANDU Reactor, 2007 Available from http://www.aecl.ca/reactor.htm
4. K. Ishigure, T. Nukii, and S. Ono, J. Nuclear Materials, 350 (1) 2006
5. B. Ben: Canada's Energy outlook: The Reference Case 2006-Electricity: Her Majesty the Queen in Right of Canada, 2006
6. P. Maak, Material Res. Society Symp. Proc., 663, 2003
7. S.B. Russel and G.R. Simmons, Proc. 11th International High-Level Radioactive Waste Management Conf. Las Vegas, 2003
8. G.Poon, M. Saiedfar, and P. Maak, Ontario Power Generation Report No.06819-REP-01200-10051-R00, 2001
9. P.Maak, Ontario Power Generation Report No.06819-REP-01200-10020-R00, 1999
10. M. Saiedfar, and P. Maak, Ontario Power Generation Report No.06819-REP-01300-10012-R00, 2000
11. P. Maak, and G.R. Simmons, Ontario Power Generation Report No.06819-REP-01200-10065-R00, 2001

12. F. Garisto, A.D'Andrea, P. Gierzewski, and T. Melnyk, Geologic Repository: Defective container scenario, Ontario Power Generation Report No: 06819-REP-01200-10127-ROO, Feb. 2004

13. D.W. Shoesmith, The Role of Dissolved Hydrogen on the Corrosion/Dissolution of Spent Nuclear Fuel, Nuclear Waste Management Organization, Report NWHD TR-2008-19 , Nov. 2008

14. D.W. Shoesmith, J. Nuclear Materials, 282, 1, 2000

15. J. McMurry, D.A. Dixon, J.D. Garroni, B.M. Ikeda, and T.W. Melnyk, Ontario Power Generation Report No.06819-REP-01200-10092-R00, 2003

16. I.V. Sieber, H. Hilderbrand, S. Virtanen, and p. Schmuki, Corrosion Science, 48, 3472-3488, 2006

17. Allison J. Davenport, Lucy J. Oblonsky, and Mary P. Ryan, J. Electrochemical Socienty, 147,(16) 2162-2173, 2000

18. Allison J. Davenport, and Jennifer A. Bardwell, J. Electrochemical Society ,142 (3) 721-724, 1995

19. R.P. Frankenthal, Electrochemical Acta, 16, 1845-1857, 1971

20. M. Buchler, P. Schmuki, and H. Bohni, J. Electrochemical Society, 145(2), 609-614, 1998

21. L.J. Oblonsky, A.J. Davenport, and M.P. Ryan, J. Electrochemical Society, 144 (7),2398-2404, 1997

22. T. Zakroczymski, Chwei-Jer Fan, Z. Szklrska-Smialowska, J. Electrochemical Society, 132 (12), 2868-2871, 1985

23. Emilse M.A. Martini, and I. L. Muller, Corrosion Science, 42, 443-454, 2000

24. Dong Fu, and J.C. Wren, J. Nuclear Materials, 374, 116-122, 2008

25. R.S. Schrebler Guzman, J.R. Vilche, and A.J. Arvia, J. Electrochemical Acta, 24, 395-403, 1978

26. S.M. Scharland, Cervice and Pitting Corrosion, Prentice Hall, 1996

27. S.M. Sharland, Corrosion Science, 27 (31), 289-323, 1987

28. R.C. Newman, M.H. Moayed, J. Electrochemical Society, 153 (8), B330-B335, 2006

29. Hans-Henning Strehblow, Mechanisms of Pitting Corrosion, Marcel Dekker, 1995

30. Z. Szklarska-Smialowska, Corrosion Science, 44, 1143-1149, 2002

31. P. Marcus, V.Maurice, and H.H. Strehblow, Corrosion Science, 50, 2698-2704, 2008

32. M.F. Toney, A.J. Davenport, and L.J. Oblonsky, Physical Review Letters, 79 (21),4281-4285, 1997

33. H.H. Uhlig, In passivity of Metals, Edited R.P. Frankenthal and J.Kruger, Princeton, 1978

34. M. Farady, Philosophical Magezine, 9, 57, (1836)

35. C.T. Schnben, Philosophical Magezine, 9, 53, (1836)

36. M. Nagayama, and M. Cohen, Electrochemical Socienty, 109, 781, 1962

37. C.L. Foley, J.Kruger, and C.J. Bechtoldt, J. Electrochemical Society, 114, 994, 1967

38. K. Kuroda, Electrochemical Society, 129, 2163-2172, 1982

39. Z. Scklarska-Smialowska, Pitting and Carvice Corrosion, NACE International, 2005

40. U.R. Evans, J. Electrochemical Society London, 1020-1028, 1927

41. L. Rozenfeld, and I.K. Marshakov, Corrosion Science, 20, 115-122, 1964

42. R. Nishimura, and K. Kudo, 8th International Congress Meeting , Germany, Vol.1, 6-16, 1981

43. A.F. Beck, M.A. Heine, and D.S. Keir, Corrosion Science, 2, 133-142, 1962

44. M.A. Heine, D.S. Keir, and M.J. Pryor, J. Electrochemical Society, 112, 24-35, 1965

45. M.A. Heine, and M.J. Pryor, J. Electrochemical Society, 114, 1001-1112, 1967

46. Hans-Henning Strehblow, In Corrosion Mechanism in Theory and Practice, Edited P. Marcus, Marcel Dekker, 1995

47. R. Gotez, B. MacDougall, and M.J. Graham, Electrochemical Acta, 31, 1299-1303, 1980

48. T.P. Hoar, and W.R. Jacob, Nature, 216, 1209-1220, 1967

49. K.H. Heusler, L. Fischer, J. Material and Corrosion, 27,551, 1976

50. W. Khalil, S. Haupt, and H.H. Strehblow, J. Materials and Corrosion, 36,(1), 15-21, 1985

51. M. Seo, Y. Matsumura, and N. Sato, 8th International Congress Meeting , Germany, Vol.1,108-118, 1981

52. J. A. Bardwell, and B. MacDougall, J. Electrochemical Society, 135, 2157-2169, 1988

53. S. Dallek, and R.T. Foley, J. Electrochemical Society, 123, 1775-1786, 1976

54. N. Sato, Electrochemical Acta, 16, 1683-1695, 1971

55. Y. XU. Wang, H.W. Pickering, J. Electrochemical Society, 140, 3448-3459, 1993

56. Z.A. Foroulis, and M.J. Thubrikav, J. Electrochemical Society, 122, 1296-1307, 1975

57. T.P. Hoar, Discuss Faraday Society, 42,299, 1947

58. T.P. Hoar, Trans Faraday Society, 45, 683, 1949

59. P. Zaya, International Congress on Metallic Corrosion, Toronto, 1984

60. M.P. Ryan, R.C. Newman, G.E. Thompson, J. Electrochemical Society, 142, L.177,1995

61. X. Zhang, W. Xu, D.W. Shoesmith and J.C. Wren, Corrosion Science, 49,4553, 2007

62. H. Oranowska, and Z. Szklaska-Smialowska, Corrosion Science, 21, 735, 1981

63. J. Tousek, Corrosion Science, 15, 147, 1975

64. C.L. McBee, and J.Kruger, Localized Corrosion, NACE , TX., 1970

65. M.A. DeCastro and B.E. Wilde, Corrosion Science, 19, 923-936, 1979

66. J.A. Bardwell, J.W. Fraser, B. MacDougall, and M.J. Graham, Electrochemical Society, 139(2), 366-370, 1992

67. Sejin Ahn, H. Kwon, and D.D. Macdonald, J. Electrochemical Society, 152, (11), 482-490, 2005

68. J.A. Bardwell, and B. MacDougall, J. Electrochemical Acta, Vol. 34, 229-232, 1989

69. R.W. Revie, J.O. Bockris, and B.G. Baker, Surface Science, 52, 644, 1975

70. B.P. Lochen, H.H. Strehblow, J. Electrochemical Society. 131,713.1984

71. H.H. Strehblow, Passivity of Metal, Editor D.M. Kolb, Advance in Electrochemical Science and Engineering, John Wiley and Sons, 2003

72. A. J. Bard, L.R. Faulkner: Electrochemical Methods: Fundamentals and Applications, 2nd Edition, John Wiley and Sons, 2001

73. V. Jovancicevic, and J.O. Bockris, Electrochemical Society, 133, 2219-2226,

74. D. Briggs and M.P. Seah, Practical Surface Analysis, John Wiley and Sons , 1983

75. W.M. Riggs and M.J. Parker, in : Methods of Surface Analysis, Elsevier, 1975

76. M.P. Seah and W.A. Dench, Surface and Interface Analysis, 1, 1979

77. C. R. Brundle, C.A. Evans, and S. Wilson, Encyclopedia of Materials Characterization, Butterworth-Heinemann, 1992

78. H.R. Verma, Atomic and Nuclear Analytical Methods, Springer, 2007

79. J.C. Riviere and S. Myhra, Handbook of Surface and Interface Analysis, Marcel-Dekker, 1998

80. P.E.J. Hewitt and R.K. Wild, Physical Methods for Materials Characterisation, IOP, 1994

81. B. Schroder, Infrared and Raman Spectroscopy: Methods and applications, VCH, 1995

82. D.R. Vij, Applied Solid State Spectroscopy, Spring, 2006

83. S.N. Begum, V.S. Muralidharan, and C.A. Basha, Applied Surface Science, 254, 2325-2330, 2008

84. W. Xu, K. Daub, X. Zhang, J.J. Noel, D.W. shoesmith, J.C. Wren, J. Electrochemical Acta, 54, 5727-5738, 2009

85. K.J. Vetter, and H.H. Strehblow, Localized Corrosion Congress, 240-251, 1971

86. M.B. Valcarce , and M. Vazquez, J. Electrochemical Acta, 53, 5007-5015, 2008

87. D.J.Blackwood, L.M.Peter and D.E.Williams; Electrochimica Acta, 33,1142, 1988

88. K. Jordan, A. Cazacu, G. Manai, S. Murphy and I.V. Shvets, Physical Review, B 74, 085416-1, 2006

89. T. Rayment, A.Davenport, A.J. Dent, J. Tinnes, R. Wiltshire, C. Martin, G.Clark, P.Quinn, J.F. Mosselmans, J. Electrochemistry Communications, 10, 855-858, 2008

90. L.J. Oblonsky, T.M. Devine, Corrosion Science, 37. 17-41, 1995

91. A. Hugot-LeGoff, J. Flis, N. Boucherri, S. Joriet, J. Electrochemical Society, 137, 2684-2689, 1990

92. W. Khalil, and S. Haupt, Corrosion Science, 36, 15-22, 1985

93. H.H. Strehblow, P. Marcus, X-ray photoelectron spectroscopy in corrosion research, Marcel Dekker, 2002

94. A.P. Grosvenor, B.A. Kobe, N.S. McIntyre, S.Tougaard, Surface and Interface Analysis, 36, 632-639, 2004

95. M.C. Biesinger, B.P. Payne, A.P. Grosvenor, L.M.W. Lau, A.R.Gerson and R.St.C. Smart, in preparation for Analytical Chemistry.

96. J.R. Galvele, J. Electrochemical Society, 123, 464-474, 1976

97. S. E. Traubenberg, and R.T. Foley, J. Electrochemical Society, 118, 1026-1038, 1971

98. Z.A. Foroulis, M.J. Thubricar, J. Electrochemical Society, 123, 1775-1786, 1976

99. R.M. Cornell, and U. Schwetmann, The Iron Oxides, John Wiley and Sons, 2000

100. M.M. El-Naggar, Applied Surface Science, 252, 6179-6194, 2006

101. R. Goetz, B. MacDougall, and M.J. Graham, J. Electrochemical Acta, 31, 1299-1303, 1986

102. X.Zhang, W.Xu, D.W. Shoesmith and J.C., Wren, Corrosion Science, 49, 4553, 2007

103. A.P. Grosvennor, B.A. Kobe, N.S.McIntyre, S.Tpugaard, and W.N. Lennard, Surface and Interface Analysis, 36, 632-639, 2004

104. J. Gio, T.M. Devine, Corrosion Science, 37-1177-1189, 1995

105. V. Schroeder, T.M. Devine, J. Electrochemical Society, 146, 4061-4070, 1991